ULTRAFAST ELECTRON DIFFRACTION: SOURCE DEVELOPMENT, DIFFRACTOMETER DESIGN AND PULSE CHARACTERISATION

Günther Horst Kassier

Dissertation presented for the degree of Doctor of Philosophy

at

Stellenbosch University

Promotor: Prof. Heinrich Schwoerer

Co- Promotor: Prof. Erich Rohwer

December 2010

DECLARATION

By submitting this dissertation electronically, I declare that the entirety of the work contained therein is my own, original work, that I am the owner of the copyright thereof and that I have not previously in its entirety or in part submitted it for obtaining any qualification.

Date : 10 March 2010

Copyright © 2010 Stellenbosch University

All rights reserved

ABSTRACT

Ultrafast Electron Diffraction (UED) is a rapidly maturing field which allows investigation of the evolution of atomic arrangement in solids on timescales comparable to the vibrational period of their constituent atoms (~10^{-13} s). The technique is an amalgamation of conventional high energy electron diffraction methods and pump-probe spectroscopy with femtosecond (1 fs = 10^{-15} s) laser pulses. Ultrafast pulsed electron sources generally suffer from limitations on the attainable electron number per pulse (brightness) due to Coulomb repulsion among the electrons. In this dissertation, the design and construction of a compact UED source capable of delivering sub-300 fs electron pulses suitable for diffraction experiments and containing about 5000 electrons per shot is described. The setup has been characterised by measurement of the transverse beam size and angular spread, and through recording and analyzing an electron diffraction pattern from a titanium foil. Measurement of the temporal duration of fs electron pulses is not trivial, and a specialised compact streak camera operating in accumulation mode has been developed as part of this study. A sub-200 fs temporal resolution has been achieved, and the dependence of temporal duration on electron number per pulse was investigated for the current UED source. The observed trends correlate well with detailed electron bunch simulations. In order to investigate ultrafast processes on samples that cannot be probed repeatedly, it becomes necessary to significantly increase the brightness of current state of the art compact sources such as the one constructed in the present study. UED sources employing electron pulse compression techniques offer this possibility. Traditional pulse compression schemes based on RF cavities, while simple in principle, pose significant technical challenges in their realisation. The current thesis describes two novel UED pulse compression methods developed by the author: achromatic reflectron compression and pulsed cavity compression. Both concepts are expected to be easier to realise than conventional RF compression. Detailed simulations predict that such sources can attain a brightness improvement of more than one order of magnitude over compact sources that do not employ compression techniques. In addition, such sources show much promise for the attainment of pulse durations in the sub-100 fs range.

OPSOMMING

Ultra vinnige elektron diffraksie is ‘n meettegniek wat tans in die proses is om vinnige ontwikkeling te ondergaan. Die tegniek het ten doel om strukturele omsettingsprosesse op ‘n lengteskaal van atoombindings en ‘n tydskaal van die vibrasie periode van atome in materie, ongeveer 10^{-13} s, te ondersoek. Dit word bewerkstellig deur die spasieresolusievermoë van gewone hoë energie elektron diffraksie met die tydresolusievermoë van femtosekonde (1 fs = 10^{-15} s) laserspektroskopie te kombineer. Die aantal elektrone per puls (intensiteit) van ultravinnige gepulsde elektronbronne word beperk deur die Coulomb afstootingskragte tussen die elektrone. Hierdie dissertasie beskryf die ontwerp en konstruksie van ‘n kompakte ultravinnige elektron bron. Die elektronpulse wat geproduseer word bevat tot 5000 elektrone per puls met ‘n tyd durasie van minder as 300 fs, en is geskik vir diffraksie eksperimente. Die aparaat is gekarakteriseer deur die volgende metings: elektronpulsdiameter, straaldivergensie, en ‘n titaan foelie se statiese diffraksie patroon. Dit is nie triviaal om die durasie van femtosekonde elektronpulse te meet nie, en n spesiale kompakte akkumulerende “streak camera” is vir die doeleindes van hierdie projek onwikkel. Die tydresolusie van hierdie “streak camera” is beter as 200 fs, en die afhanklikheid van die pulsdurasie wat deur die ultravinnige elektron bron geproduseer word as n funksie van die elektrongetal per puls is met behulp van hierdie toestel bepaal. Die resultate klop redelik goed met gedetaileerde simulasies van die elektron puls dinamika. Die karakterisasie van monsters wat nie herhaaldelik gemeet kan word nie vereis verkieslik ‘n nog hoër pulsintensiteit as wat met huidige bronne bereik kan word. ‘N verdere doelstelling is dus om ultravinnige elektron bronne te ontwikkel wat pulse met meer elektrone per puls kan genereer. Dit kan bewerkstellig word deur bronne wat van elektron puls kompressie tegnieke gebruik maak. Die tradisionele manier waarop dít gedoen word is deur middel van n kontinu gedrewe radio frekwensie holte. Hierdie metode gaan egter gepaard met aanmerklik hoë tegniese uitdagings. Om hierdie rede het die outeur twee alternatiewe puls kompressie konsepte ontwikkel: akromatiese reflektron kompressie and gepulsde holte kompressie. Albei konsepte sal waarskeinlik makliker wees om te realiseer as die tradisionele radio frekwensie kompressie, en is deur middel van gedetaileerde simulasies geverifiseer. Hierdie simulasies voorspel dat die intensiteit van genoemde bronne met ten minste n grooteorde meer kan wees as wat tans met kompakte ultravinnige elektron bronne moontlik is. Verder blyk dit dat sulke bronne n pulsdurasie van minder as 100 fs kan bereik.

ACKNOWLEDGEMENTS

I would like to thank the following people:

Prof. Heinrich Schwoerer for his exemplary supervision of this project. Heinrich has been actively involved with invaluable guidance and enthusiasm at every level of the present project, and was always willing to lend support in academic, administrative and financial matters alike. Despite his keen involvement, he encourages the free and independent development of ideas by his students, and has always supported me in whatever research path I chose to take. For this I am particularly grateful.

My co-supervisor Prof. Erich Rohwer for his guidance and support throughout the course of this study. The opportunity for me to do my PhD at the Laser Research Institute has to a large extent been created by Erich, and I shall always be grateful for that.

My fellow students Kerstin Haupt and Nicolas Erasmus who are also involved with the UED project. Perhaps for the first time I have experienced the power of true teamwork in my academic career. Kerstin was always more than willing to help me with various matters ranging from experiments to the creation of beautiful drawings. Nic and Kerstin, with their technical savvy, have been instrumental to the experimental success of the current project. I would also like to thank them, as well as the new member of our team Ilana Boshoff, for proofreading this dissertation.

The technical assistance of Eben Shields in all matters electronic is gratefully acknowledged. Ulli Deutschländer is perhaps the most generally useful person in the Stellenbosch University Physics Department as he not only seemingly knows everything, but also knows where everything is located.

The machinists Boel Botha and John Burnes must be thanked for the beautiful pieces they have created for the UED setup. In particular, the magnetic lens made by John as well as Perspex windows, a mount for the magnetic lens and various chamber improvements done by Boel Botha.

Sergio Coelho for all the help we have received from him during the course of this study. In particular, Sergio has fabricated the gold photocathode used in the current UED source as well as

the gallium arsenide photoswitch; both these components were indispensable for the success of this project. In addition, Sergio has with word and deed contributed much to the optimisation of our vacuum system. Prof. F. Danie Auret is also acknowledged for his willingness to collabotate with us and supplying the gallium arsenide material.

Ulrich Büttner at Electronic Engineering, University of Stellenbosch, for putting his time, expertise and equipment at our disposal. His metal evaporation and sputter systems have been particularly useful. Dirk Fourie at iThemba labs for supplying us with advice and equipment needed for the measurement of magnetic field profiles. Christoph Hebeisen at the University of Toronto for supplying us with helpful advice on electron gun design. Klaus Floettmann at DESY has provided me with valuable supplementary material for the ASTRA code, for which I am very grateful. Anton du Plessis at the CSIR in Pretoria for fruitful discussions on reflectrons.

My parents Horst and Marianne Kassier for their love and support.

TABLE OF CONTENTS

LIST OF TABLES

LIST OF FIGURES

1. INTRODUCTION TO ULTRAFAST ELECTRON DIFFRACTION (UED)

The atomic configuration of substances is a major determinant of their physical properties on a macroscopic scale and is also instrumental in determining their chemical properties or biological function. The essential role that knowledge of atomic structure plays in our understanding of biological function in particular has been epitomised by the spectacular progress made in fields such as genetics since the unravelling of the structure of DNA by Francis Crick and James D. Watson in 1953 from X-ray diffraction (XRD) images recorded by Rosalind Franklin [1,2,3]. With the plethora of opportunities afforded by XRD for studying and understanding the properties of matter, it seems fitting that the first Nobel Prize in physics was awarded to Konrad Wilhelm Röntgen in 1901 for his discovery of X-rays [4]. The most common method of generating X-rays for diffraction, which is based on inner shell line emission of metal targets excited by energetic electrons, remains essentially unaltered from the method used by Röntgen himself. Typical X- ray wavelengths emitted are about 1 Å, which is on the order of the d-spacing of crystal lattices and therefore ideally suited for high resolution molecular structure determinations.

Despite the marvellous contribution that diffraction techniques, most notably XRD but also electron diffraction, have made to our understanding of the structure of matter, these techniques lack the capability to study an equally important aspect that is needed for a complete understanding of matter at the atomic level: structural dynamics. Static diffraction techniques only give information about equilibrium structures; more precisely, the recorded diffraction pattern represents an average of a given structure with respect to vibrational and conformational changes induced thermally or otherwise over a timescale that is typically on the order of milliseconds or seconds. In order to more completely understand physical, chemical and biological reactions, it is necessary to study the molecular/ crystalline structure on the timescales at which these processes happen. This would allow an unprecedented view of the evolution of such reactions, with a particularly exciting possibility being the observation of short-lived reactionary intermediates which are not observed with static techniques at all. The timescales mentioned can be estimated as the time taken for a sound wave in condensed matter to propagate the inter-atomic distance or, equivalently, the vibrational period of atoms in molecules. This timescale is on the order of 10^{-13} s, or 100 femtoseconds (fs).

The process of capturing molecular dynamics on such short timescales is in many ways analogous to modern high speed photography. A famous example often alluded to in the ultrafast

spectroscopy community is a series of photographs depicting a racehorse in full gallop taken by Eadweard Muybridge in 1877. Using a series of 24 cameras with a particularly high shutter speed, Muybridge was able to record a high speed "movie" from which he could answer in the affirmative the long standing question of whether a galloping horse is ever fully airborne. As every photographer knows, there are two major technical problems associated with attempting to increase the temporal resolution of cameras as was done by Muybridge: 1) there are technical limits to achievable shutter speeds and, perhaps more importantly, 2) a higher shutter speed implies that less light reaches the detector (photographic film) due to the reduced exposure time, resulting in under-exposed images[1]. This highlights a critical issue common to all high speed single-shot imaging endeavours: the shorter the exposure time in recording an image, the larger will be the required illumination intensity or brightness. In moving from ms to μs exposure times, it has been necessary to introduce stroboscopic (flashlight) techniques, in part due to the fact that it becomes difficult for mechanical shutters to achieve sufficiently short exposure times. In flashlight photography, the exposure time is controlled by the duration of the flashlight pulse, which can easily reach sub-μs timescales. This technique was pioneered by Harold "Doc" Edgerton who produced his famous, crisp, full colour images of such elusive processes as a rifle bullet at the moment when it pierces an apple. Crucially, the flashlight not only provides the enhanced temporal resolution, but also delivers the required brightness which is much larger than what is achievable with continuous illumination sources such as sunlight. Another critical requirement in obtaining high time resolution images is of course the synchronisation of the observed process with the probing flashlight pulse; on μs timescales, this can still easily be done using an electronic trigger for the flashlight.

For observing molecular evolution on the timescale of 10^{-13} s, there exist suitable "flashlights": *femtosecond lasers*. These sources are off the shelf table top devices capable of producing optical pulses with durations well in the femtosecond range and with sufficient illumination brightness to allow the observation of fs molecular dynamics. The method employed to achieve this is called pump-probe spectroscopy, and it is similar to flashlight photography. A fs laser pulse is divided, using a beam splitter, into two pulses called a "pump" pulse and a "probe" pulse. The pump pulse is directed onto the specimen and starts the desired molecular process at a very precise time. The probe pulse, which is inherently synchronised with the pump pulse, is propagated through a variable time of flight delay line, and can thus be used to interrogate the desired observable at a nominal time subsequent to sample excitation. Probe

[1] Other than developing a sufficiently fast shutter, the major technical obstacle overcome by Muybridge was this issue of under- exposure of photographic film when a high shutter speed is used. He solved the problem by using special high sensitivity photographic film and increased the image contrast by placing a white background behind the galloping horse.

pulses with optical wavelengths in the few eV energy range are suitable for observing transitions of outer shell or valence band electronic states, and as such all-laser pump probe spectroscopy is a valuable tool for investigating the ultrafast evolution of the energy landscape of molecules or energy bands. No direct information on molecular structure is gleaned from this however, which brings us back to X-rays.

X-rays have been used as ultrafast probes with some success [5,6], but the achievement of true fs temporal resolution with X-ray pulses that are sufficiently bright to generate useful diffraction patterns has been rare. The best results have been achieved using large synchrotron sources with limited and expensive beam time. Even these sources suffer from relatively low brightness if one wishes to probe sub-picosecond dynamics. Free electron laser facilities are however in a rapid phase of development and will allow sub-100 fs high-brightness X-ray pulses with a tuneable narrow bandwidth. Table top ultrafast X-ray sources, while in existence, are currently not at a very mature state of development and suffer from poor brightness [7,8]. Another problem that should be mentioned is that due to the relatively low scattering cross section of X-rays in matter, a relatively large specimen thickness in the μm range is required, and this can lead to temporal mismatch of the X-ray pulse with the optical pump pulse in the 100 fs range due to differences in the propagation velocity of these wavelengths in matter. These difficulties have triggered the development of an alternative approach to the problem of probing the structure of matter on fs time scales: *Ultrafast Electron Diffraction (UED)*. For a review of progress in ultrafast X-ray and electron diffraction techniques, see Chergui and Zewail [9], Dwyer et al. [10] and Miller et al. [11].

High energy electron beams in the 10 – 100 keV range have a de Broglie wavelength in the few pm range. While this is not particularly well matched with typical inter-atomic spacings, electron diffraction is nonetheless well suited for determining inter-atomic structure, and has been extensively used for this purpose. In the context of ultrafast studies, electrons have a number of advantages over X-rays. Due to the fact that electrons are charged particles, they are scattered by the entire electrostatic potential of atoms, unlike X-rays which interact with the inner shell orbitals. As a result, the scattering cross section of electrons in matter is orders of magnitude larger than that of X-rays, and therefore much thinner samples in the nm range rather than the μm range are used. This generally implies a much better spatial and temporal overlap of the pump and probe pulses than what is achievable with X-rays, thus producing cleaner diffraction images with potentially better temporal resolution. In addition, ultrashort electron pulses are easily generated by fs laser excitation of metal photocathodes followed by acceleration in a suitable electric field. The resultant pulses can be easily controlled by readily available electron optics including deflectors and lenses, and therefore it is possible to create well-directed

high brightness electron pulses in a table top setup [12]. The creation and efficient control of X-ray pulses is much more problematic. There are also some challenges associated with fs electron pulses, however. The electric charge of electrons that is responsible for their excellent scattering cross section and easy controllability can also become a problem. Space charge forces in electron bunches in the 10 keV energy range lead to rapid temporal broadening, and electron bunches containing on the order of 10000 electrons starting out with a duration in the 100 fs range will rapidly broaden to ps pulse durations within only about 1 ns of propagation time. This places limits on the all-important brightness attainable for UED bunches, an issue discussed in detail in Chapter 3 of the present work. One way to avoid this problem is to keep the number of electrons per pulse small, down to only a single electron per pulse in extreme cases [13]. The diffraction image is then built up by accumulating a sufficiently large number of shots; the requirement of reasonable accumulation time requires a very large repetition rate, preferably in the MHz range. This however demands a sample that completely relaxes back to its original state subsequent to being excited, since it would be impossible to move "fresh" sample regions into the beam path at such a high repetition rate[2], even if enough sample material is available. In general, a sample is neither repeatedly excitable nor does one have an unlimited supply of it. For example, if one wishes to investigate the process of metal melting on short timescales, one is faced with the situation that, although melting itself is reversible in the sense that molten metal rapidly re-solidifies, the crystal structure of the metal is permanently altered [12]. This makes the achievement of high brightness UED pulses a very important quest [10].

Although femtosecond time resolved electron diffraction is a relatively new research field, many exciting results have already been obtained. The subject of UED has been reviewed by King et al. [13] (with special reference to ultrafast electron microscopy), Dwyer et al. [10] and Zewail [14]. Gas phase UED studies have revealed interesting dynamics of simple molecules on ps time scales [15,16]. Studies on condensed matter systems have been quite varied. Ultrafast melting of aluminium [17,12] and bismuth [18] as well as ultrafast phonon dynamics in gold [19] and silicon [20,21,18] have been studied with UED in transmission geometry. Reflection geometry UED, like its static counterpart Reflection High Energy Electron Diffraction (RHEED), is particularly well suited for studying surface and interface effects. Ultrafast dynamics studies of interfacial water on hydrophobic surfaces [22,23] and thin film bismuth layers on silicon [24,25] are noteworthy in this context. Other studies in reflection geometry are ultrafast phase transformations in vanadium dioxide [26], preablation and chemical bond dynamics in graphite [27,28] and phonon dynamics in cuprate superconductors [29].

[2] An exception to this is gas phase UED.

The present dissertation describes details of the design process and construction of a compact high brightness ultrafast electron diffractometer suitable for delivering sub-300 fs electron pulses containing up to 5000 electrons per pulse and having excellent spatial resolution capability. The setup is closely modelled on the pioneering design of Siwick et al. [12], and should enable the study of irreversible ultrafast processes in solid materials. The proper design of the UED setup requires detailed knowledge of the relevant properties of electron beams, particularly those parameters affecting the spatial resolution capability. Chapter 2 is therefore devoted to discussing electron beam properties such as emittance, brightness and coherence. The design aspects of the diffractometer that are particular to the very short pulse duration requirements are highlighted in Chapter 3. Pulse broadening due to initial photoelectron energy distributions and particularly space charge effects are discussed on a semi-quantitative basis, and the importance of electron bunch simulation codes as a design tool is emphasised. The diffractometer design is presented and its performance is verified through quantitative simulations using the ASTRA code. The diffractometer, which was constructed as part of the present study, is described in Chapter 4. Although no time resolved work has yet been done, a static diffraction image of a thin free standing titanium foil has been recorded and analysed. Some basic beam parameter measurements including beam radius at the sample and the energy spread at the photocathode conclude this chapter. Electron pulse duration measurements on sub-picosecond timescales are not trivial, and there is much room for improvement of existing measurement techniques. In Chapter 5, a novel compact streak camera design is introduced that was optimised for typical UED bunch parameters. The experimental results presented in this chapter demonstrate that it outperforms more conventional designs and that it is indeed suitable for UED pulse duration characterisation. Measurement of the pulses of the constructed electron gun using this streak camera shows that sub-300 fs electron pulses are readily achievable with the present setup. The present UED source may not have sufficient brightness for certain applications, and in Chapter 6 two novel pulse compression source concepts are described: an achromatic reflectron compressor and a pulsed cavity compressor that is similar in structure to the compact streak camera described in Chapter 5. These sources are potentially capable of boosting the brightness of compact UED sources by an order of magnitude or more. While another UED compression scheme based on a conventional continuous wave RF cavity exists, it has yet to be demonstrated, and the author contends that the pulse compression schemes presented in this dissertation would be easier to implement. Chapter 7 summarises the main aspects of the dissertation and points toward possible future research projects.

2. ELECTRON BEAM STATISTICS AND DIFFRACTION

In conventional (static) electron diffraction, the transverse beam size, angular spread, transverse emittance and longitudinal energy spread are of importance as they determine the spatial resolution capability of the beam. In ultrafast electron diffraction (UED), the parameters of temporal duration and longitudinal emittance are added to this list. This short chapter summarises the statistical definitions of these quantities and explains their relation to those beam parameters that, in addition to the above, represent the important figures of merit for UED beams: the transverse and longitudinal coherence lengths and beam brightness.

2.1 Statistical Bunch Parameters

Electron beams are conveniently described in terms of quantities that represent a statistical average of a certain observable pertaining to the constituent particles. The weighted statistical average $\langle q \rangle$ of a quantity q (e.g. position x) is given by

$$\langle q \rangle = \frac{\sum w_i q_i}{\sum w_i} \; ; \; \sum w_i = N \tag{2.1}$$

where the weight w_i accounts for the density distribution of N particles in the ensemble (e.g. a Gaussian distribution). An important statistical parameter is the root mean square (rms) deviation σ_q of q:

$$\sigma_q = \sqrt{\langle q^2 \rangle - \langle q \rangle^2} \tag{2.2}$$

Common parameters of bunched electron beams are the rms spatial extent in the x, y and z-direction: σ_x, σ_y and σ_z. For Gaussian distributions, these correspond to the standard deviation of the spatial distribution function. For the particle momenta p_x, p_y and p_z one has, analogously, the rms momentum spread $\sigma_{p,x}$, $\sigma_{p,y}$ and $\sigma_{p,z}$. Statistical quantities involving linear correlations between position and momentum are of particular importance in electron beam optics since phase space manipulations through beamline elements are usually linear by design. The rms normalised emittance in the x-direction $\varepsilon_{n,x}$ defined by

$$\varepsilon_{n,x} = \frac{1}{mc} \sqrt{\langle x^2 \rangle \langle p_x^2 \rangle - \langle x p_x \rangle^2} \tag{2.3}$$

is a measure of the product of the rms beam size and the linearly un-correlated part of the rms momentum spread. The $\langle x p_x \rangle^2$ term cancels the dependence of $\varepsilon_{n,x}$ on any momentum spread in the x-direction that is linearly correlated with x, and therefore the normalised emittance is invariant with respect to linear focussing. At a beam waist, such correlations vanish and Equation 2.3 reduces to $\varepsilon_{n,x} = \frac{1}{mc} \sigma_x \sigma_{p,x}$. For a distribution with a linear p_x- x relationship on

large length scales but with a local random Gaussian rms momentum spread $[\sigma_{p,x}]_l$, Michalik and Sipe have proved that [30]

$$\varepsilon_{n,x} = \frac{1}{mc}\sigma_x\left[\sigma_{p,x}\right]_l \tag{2.4}$$

The emittance in the *y* and *z*-directions is defined analogously, and both transverse normalised emittances $\varepsilon_{n,x}$ and $\varepsilon_{n,y}$ are independent of the bunch centre momentum p_z. The transverse normalised emittance as evaluated by Equations 2.3 and 2.4 has units of π rad m (rad = radian), but is usually specified in π mrad mm, π μm or π nm. The longitudinal normalised emittance $\varepsilon_{n,z}$ is often specified in units of energy × length. To convert $\varepsilon_{n,z}$ from units of π mm to π eV mm one has the following formula:

$$\varepsilon_{n,z}[\pi\ eV\ mm] = \frac{p_z c}{e}\varepsilon_{n,z}[\pi\ mm] \tag{2.5}$$

where *e* is the elementary charge. Physically, a longitudinal normalised emittance of 1 π eV mm means that an rms energy spread of 1 eV is required for the beam to be bunched to an rms length of 1 mm in the propagation direction. As already mentioned, $\varepsilon_{n,x}$, $\varepsilon_{n,y}$ and $\varepsilon_{n,z}$ are constants of motion when the beam is subject to perfectly linear electromagnetic forces, a fact that follows from Liouville's theorem. If nonlinearities exist, the normalised emittance invariably increases. The normalised emittances are a stringent measure for the quality of a beam, and the 6D peak brightness *B* for a Gaussian distribution is given in terms of the 6D phase space volume $\varepsilon_{n,x}\varepsilon_{n,y}\varepsilon_{n,z}$ as [31][3]

$$B = \frac{Nec}{(2\pi)^3\epsilon_{n,x}\epsilon_{n,y}\epsilon_{n,z}} \tag{2.6}$$

B is a measure of the peak electron current per unit cross sectional area per unit solid angle per unit energy spread that can be obtained from a beam. For many applications, the rms energy spread is of lesser importance, which leads to the definition of the transverse brightness B_t given by

$$B_t = \frac{I}{4\pi^2\epsilon_{n,x}\epsilon_{n,y}} \tag{2.7}$$

where *I* is the peak beam current. The question of which of these two definitions of brightness is more appropriate in UED is considered to be worthy of debate by the author, as further discussed in Section 2.2.2.

[3] *B* has a different normalisation constant than in reference [31] due to the definition of $\varepsilon_{n,z}$ given in the present work.

2.2 Coherence and Diffraction: Relation to Bunch Parameters

2.2.1 Electron Waves

The basis of electron diffraction is the wave nature of electrons. The de Broglie wavelength λ of matter waves associated with energetic electrons is related to electron momentum p and the reduced Planck's constant $\hbar$ by

$$\lambda = \frac{2\pi\hbar}{p} \tag{2.8}$$

By invoking Dirac's equation, this can be written in terms of the electron kinetic energy E_k as

$$\lambda = \frac{2\pi\hbar c}{\sqrt{E_k(E_k + 2E_0)}} \approx \frac{2\pi\hbar}{\sqrt{2mE_k}};\ E_k < 50\ keV \tag{2.9}$$

where c is the speed of light and E_0 the rest mass energy of an electron given in terms of the electron rest mass m by $E_0 = mc^2 = 511$ keV. Using the non relativistic approximation of equation 2.4 results in an error of less than 10% on λ if $E_k < 50$ keV. The wavelength of 30 keV electrons is 7.0 pm, much less than the typical inter-atomic distance of solids which is on the order of a few Å.

2.2.2 Longitudinal Coherence

Electron beams have a certain longitudinal energy spread $\Delta E_{k,z}$ that arises from the initial energy spread present at the source, the effect of beamline elements or space charge. As a consequence, the de Broglie wavelength λ of the constituent electrons is also subject to a certain wavelength spread $\Delta\lambda$, along with the associated wavenumber spread Δk. If one has a beam with average wave number k_0 and wavenumber spread Δk travelling in the z-direction with velocity v, its constituent electron plane waves adopt the form

$$\psi(z,t) = \exp[i(k_0 + \delta k)(z - vt)]\ ;\ -\Delta k/2 \le \delta k \le \Delta k/2 \tag{2.10}$$

It is assumed that the electron waves are in phase at $z = t = 0$. Consider now a wavepacket with a correlated wavenumber- z-displacement relation $k_c(z) = k_0 + g(z)$ where $g(z)$ is an arbitrary continuous function of z. Assume further that, for all z, the wavenumbers in the packet are normally distributed in k-space with mean value $k_c(z)$ and standard deviation σ_k. The superposition of this continuous wave spectrum at $t = 0$ is given by

$$\frac{1}{\sqrt{2\pi}\sigma_k}\int_{-\infty}^{\infty} \exp\left[\frac{(k - k_c(z))^2}{2\sigma_k^2}\right]\exp[ikz]\,dk \tag{2.11}$$

Recognising the above as an inverse Fourier transformation of a Gaussian in k-space, this is readily evaluated as

$$A \cdot \exp\left[\frac{-\mathrm{z}^2}{2(1/\sigma_\mathrm{k})^2}\right] \exp[ik_c(z)z] \tag{2.12}$$

where all multiplicative constants, which are inconsequential for the further analysis, are absorbed by the pre-factor A. The wavefunction is thus a chirped plane wave with wavenumber $k_c(z)$ that is enclosed by a Gaussian envelope with standard deviation $1/\sigma_k$. The longitudinal coherence length $L_{c,z}$ is then defined as the rms width of this envelope

$$L_{c,z} \equiv \frac{1}{\sigma_k} = \frac{\hbar}{[\sigma_{p,z}]_l} \tag{2.13}$$

where $[\sigma_{p,z}]_l$ is the local uncorrelated longitudinal rms momentum spread[4] corresponding to σ_k. $L_{c,z}$ is thus a measure of the length in the z-direction over which the waves can be considered to interfere constructively. Since $L_{c,z}$ depends only on the uncorrelated part of the momentum spread $[\sigma_{p,z}]_l$, it is chirp-independent. If one has a linearly chirped pulse, the longitudinal normalised emittance is given in terms of $[\sigma_{p,z}]_l$ by Equation 2.4. For this case, $L_{c,z}$ may be conveniently written as

$$L_{c,z} = \frac{\hbar\sigma_z}{mc\varepsilon_{n,z}[\pi\ m]} = \frac{\beta\gamma\hbar c\sigma_z}{e\varepsilon_{n,z}[\pi\ eV\ m]} \tag{2.14}$$

where $\beta = v_z/c$, γ is the Lorentz factor and the units of $\varepsilon_{n,z}$ are indicated in square brackets with the second equality following from Equation 2.5. If the chirp deviates from linearity, Equation 2.14 underestimates $L_{c,z}$. Thus $\varepsilon_{n,z}$ is a stringent determinant of $L_{c,z}$[5]. In the case of continuous beams, the concept of longitudinal emittance is not meaningful, and the longitudinal coherence length is given in terms of the beam energy E_k and rms energy spread ΔE_k (neglecting relativistic effects) by [32]

$$L_{c,z} = \frac{\lambda E_k}{\pi\Delta E_k} \tag{2.15}$$

The following example is instructive: static electron beams emitted from a tungsten filament typically have an rms energy spread of about 0.1 eV. Assuming 30 keV beam energy, Equation 2.15 predicts a longitudinal coherence length of 700 nm, which is typical of static diffraction sources [33]. For the UED bunch parameters as simulated in Section 3.3, $\varepsilon_{n,z}$ and σ_z at the sample position typically assume values of 0.01 – 0.1 π eV mm and 6 μm – 20 μm respectively. Compact UED sources thus have typical $L_{c,z}$ values in the 10 - 40 nm range as evaluated by Equation 2.14. While this is considerably smaller than what is obtained with

[4] $[\sigma_{p,z}]_l$ should not be confused with the *total* rms momentum spread $\sigma_{p,z}$ which is averaged over the entire pulse. $[\sigma_{p,z}]_l$ is equal to the momentum spread measured at a single point in z- space, and is therefore independent of any correlated momentum spread.

[5] For a rigorous treatment of the relationship between the local momentum spread, coherence length and emittance, see Michalik et al. [34] and Michalik and Sipe [30].

static sources, it is nonetheless comparable to or larger than the thickness of typical samples probed in transmission geometry, and therefore one would not expect significant deterioration of the diffraction image quality due to the reduced coherence (see also the discussion of this issue by Michalik et al. [34]). Unfortunately, this is in general no longer true for compressing UED sources. In case of the pulsed cavity compressor described in Section 6.3, $L_{c,z}$ of the pulses containing 10^5 electrons is only about 0.4 nm. This is even smaller than the transverse coherence length, raising concerns that the effective brightness of such sources may not be as high as one might expect from the enhanced number of electrons per pulse due to the strongly reduced longitudinal beam coherence. Essentially, the debate is whether Equation 2.6 or Equation 2.7 is the appropriate figure of merit for the effective beam brightness, and the author contends that this issue has not yet been satisfactorily addressed by the UED community. A more detailed analysis by Michalik et al. [34] reveals, however, that Equation 2.14 severely underestimates the longitudinal coherence length. In fact, these authors find that $L_{c,z}$ is quite insensitive to the longitudinal energy spread, and depends mainly on the transverse beam parameters. For typical UED bunch parameters, Michalik et al predict a longitudinal coherence length that exceeds typical transmission geometry sample thicknesses.

2.2.3 Transverse Coherence

The finite electron source size gives rise to a finite transverse emittance and its associated uncorrelated rms angular spread $\sigma_{\theta,s}$ at the sample which persists even for perfectly collimated beams. As seen in Figure 2.1, two electron waves that have the same wavelength λ and are initially in phase will run out of phase at the sample plane due to the difference in propagation angle $\sigma_{\theta,s}$ between them. The length on the sample plane for which this happens is known as the transverse coherence length $L_{c,x}$. To derive an expression for $L_{c,x}$, consider Figure 2.1: assuming small angles $\sigma_{\theta,s}$, the phase shift $\Delta\lambda$ is given in terms of the transverse displacement x by

$$\frac{\Delta\lambda}{x} = \sigma_{\theta,s} = \frac{p_x}{p} \tag{2.16}$$

with p_x the transverse momentum and p the bunch centre momentum. The waves that are originally in phase are then subject to a variable phase shift $\Delta\lambda$ as they arrive at the sample plane, and can be written as

$$\exp[ik(z + \Delta\lambda)] = \exp[ikz] \exp[ik\Delta\lambda] \tag{2.17}$$

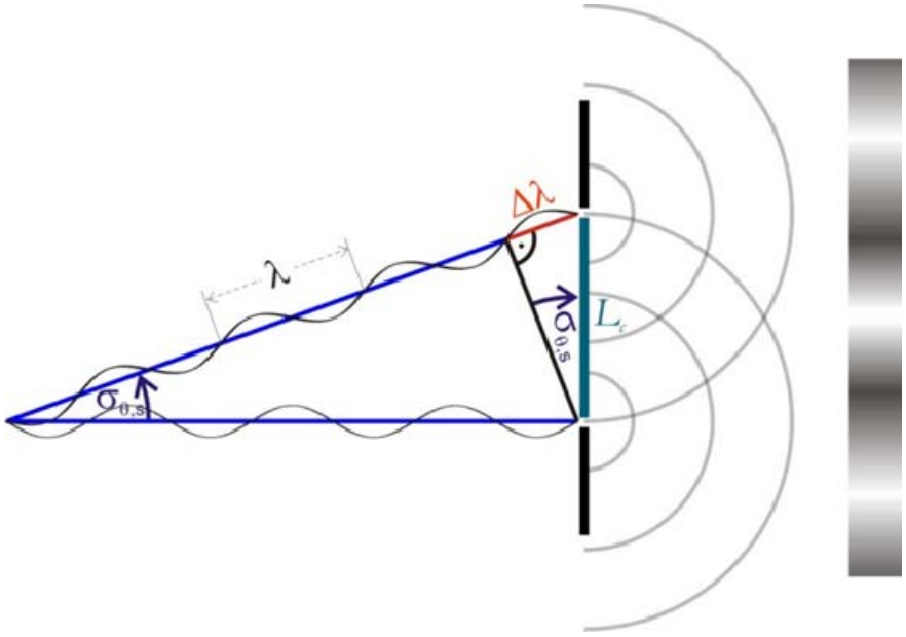

Figure 2.1. Illustration of the concept of transverse coherence. Due to the finite transverse emittance, there exists an angular spread $\sigma_{\theta,s}$ of the electron beam at each point on the sample plane. The diffraction image therefore consists of an interference pattern due to waves arriving with a range of angles. As illustrated in the figure, the finite $\sigma_{\theta,s}$ implies that electron waves with wavelength λ which are originally in phase will run out of phase by an amount $\Delta\lambda$ after a certain length called the transverse coherence length L_c.

The first factor on the right hand side is simply a constant phase independent of x, and can be ignored in the further analysis. The second factor can be written as

$$\exp\left[i\frac{p}{\hbar}x\frac{p_x}{p}\right] = \exp\left[\frac{ip_x x}{\hbar}\right] = \exp\left[ik_x x\right] \tag{2.18}$$

via Equation 2.8, and the transverse wavenumber $k_x = p_x/\hbar$ is introduced in the last equality. Now, suppose that the transverse momentum chirp function is $p_c(x)$. Assuming once again a Gaussian local transverse momentum spread with standard deviation $[\sigma_{p,x}]_l$, one has the momentum distribution function

$$\frac{1}{\sqrt{2\pi}\sigma_{p,x}}\exp\left(\frac{(p-p_c(x))^2}{2[\sigma_{p,x}^2]_l}\right) = \frac{\hbar}{\sqrt{2\pi}\sigma_{k,x}}\exp\left(\frac{(k_x-k_c(x))^2}{2\sigma_{k,x}^2}\right) \tag{2.19}$$

which can be written in terms of k_x as demonstrated by the second equality. The wave function is then given by

$$\frac{\hbar}{\sqrt{2\pi}\sigma_{k,x}}\int_{-\infty}^{\infty}\exp\left[\frac{(k_x-k_c(x))^2}{2\sigma_{k,x}^2}\right]\exp[ik_x x]\,dk_x \tag{2.20}$$

which in analogy to the longitudinal case leads to a Gaussian envelope with standard deviation of $1/\sigma_{k,x} = \hbar/[\sigma_{p,x}]_l$. With the transverse emittance given by Equation 2.4 and assuming a linear transverse chirp, one obtains for the transverse coherence length

$$L_{c,x} = \frac{\hbar \sigma_x}{mc\varepsilon_{n,x}} \tag{2.21}$$

From Equation 2.4 it is clear that the transverse normalised emittance present at the electron source decreases with the source size. Assuming conservation of $\varepsilon_{n,x}$ in the beamline, Equation 2.21 predicts that the transverse coherence length increases with beam size at the sample. Given a typical photoemission source emittance of $600\times\sigma_{x,ph}$ π nm where $\sigma_{x,ph}$ is the rms radius of the photoemission source in mm (see Section 3.1.2), Equation 2.21 implies that $\sigma_x \geq 3\times\sigma_{x,ph}$ if a transverse coherence length of greater than 2 nm is desired. The electron gun design presented in Section 3.3 conforms to this requirement. As will be seen in Sections 3.1.33.3, generation of electron bunches on a small initial spot size implies increased temporal spreading due to space charge forces, which can be detrimental to UED temporal resolution. The concern of space charge induced emittance growth leading to a reduction in the longitudinal coherence length as discussed in Section 2.2.2 is much less severe in the transverse case, as confirmed in Section 3.3 and Chapter 6. The reason for this asymmetry is the fact that UED bunches start out in the pancake regime, implying that the initial longitudinal bunch dimension, and therefore its emittance, is much smaller than its transverse counterpart[6]. Any emittance growth is therefore more noticeable in the longitudinal direction. Transverse emittance growth does however become apparent at very large pulse charges and small initial radii.

[6] As an example, consider a 30 keV electron bunch with an initial duration of 150 fs and rms radius of 25 μm. The longitudinal rms width is about 6 μm, a factor of 4 smaller than the rms radius.

3. THE BEHAVIOUR OF ULTRASHORT ELECTRON PULSES AND UED GUN DESIGN

Ultrafast electron guns, although similar in structure to conventional (static) designs as implemented in electron crystallography, do have some unique features that are necessitated by the requirement of extremely short pulse durations in the 100 fs regime. To attain such short pulse durations in the first place, the electrons are photo-generated from metal cathodes using readily available femtosecond laser sources. Keeping the thus produced electron pulses short in the presence of the inevitable energy spread inherent in photoelectron bunches as well as space charge forces between the electrons is not trivial, and herein lies the special challenge of ultrafast electron gun design. Due to the many body nature of electron-electron interaction, there are no simple formulas that can be used to predict the behaviour of highly charged electron bunches, and particle simulation codes are thus a very useful tool in the design of ultrafast electron sources. Section 3.1 describes the basic design of compact high brightness UED sources and affords the reader a qualitative picture of ultrashort electron bunch dynamics. Electron bunch simulation codes, with special reference to the ASTRA code, are described in Section 3.2 while details of the present UED source design (the implementation of which is described in Chapter 4) along with simulation results are presented in Section 3.3.

3.1 Semi-Quantitative Description of UED Beam Dynamics

3.1.1 UED Gun Setup

Electron guns suitable for ultrafast electron diffraction must satisfy similar requirements demanded of those used in static high energy electron diffraction. The transverse beam emittance, beam size and longitudinal rms energy spread at the sample should be conducive toward a sufficiently large coherence length, as discussed in Section 2.2. In addition, the beam energy should be suitable for the particular diffraction geometry: transmission electron diffraction is typically carried out with energies in the 100 keV range while reflection geometries (RHEED) require energies in the 10 keV range. It is therefore not surprising that UED guns are closely modelled on their static counterparts. The requirement of the very short pulse length to be produced by UED guns does, however, lead to some design modifications.

In static high energy electron diffraction guns, the electron source is typically a heated filament or a field emission tip that is held at the required negative electrostatic potential. A special electrode called a Wehnelt cylinder, which is held at a slightly higher negative potential than the emission source, is placed in the beam path between the cathode and

grounded anode. The Wehnelt cylinder focuses the electron beam onto an extraction aperture on the anode from which a well collimated beam emerges, which is then passed through deflection and focussing optics. The UED gun to be discussed here has a somewhat different structure, as can be seen in Figure 3.1.

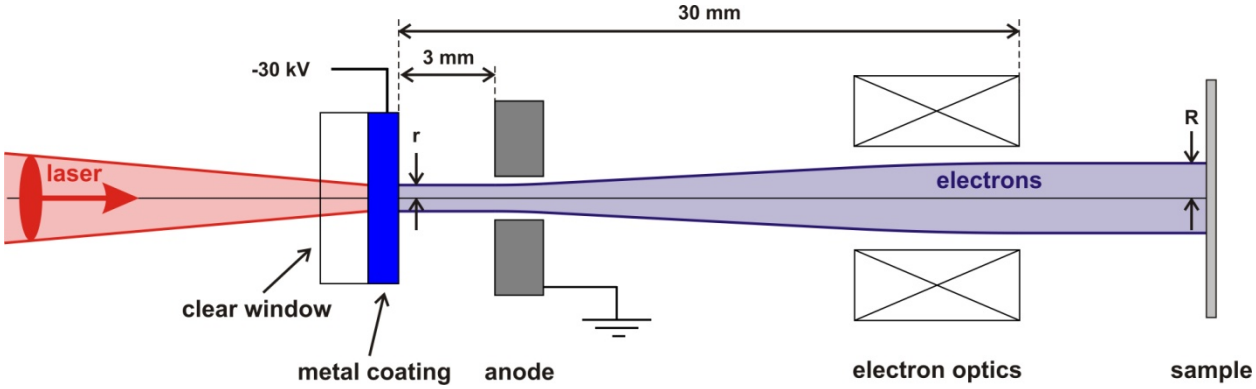

Figure 3.1. Basic structure of an UED gun. The drawing is not to scale and the indicated dimensions are approximate. The beam radius at the source and sample are denoted by r and R respectively. Practical UED sources usually have $r < R$ for improved transverse coherence.

Instead of a filament or tip, a metal photocathode is used to generate an ultrashort electron pulse from the femtosecond laser pulse[7]. The electron pulse is accelerated toward the anode aperture without passing through a focusing Wehnelt cylinder. The acceleration gap between cathode and anode is very short with very high electric field strength. Thereafter, the electron pulse passes through focusing optics via the sample to the detector in the same way as in static electron diffraction. The discussions on UED beam dynamics that follow in this section will elucidate these gun design choices.

3.1.2 Photoemission Energy Spread and its Effect on Bunch Parameters

Although the photoelectric effect is quantum mechanical in nature, the emission of photo-excited electrons from metal targets is a classical process: electrons acquire sufficient kinetic energy to overcome the effective work function of the metal Φ_{eff}, resulting in ballistic electron ejection. The photoemission of electrons can be regarded as a three step process [35,36,37]: 1) absorption of photon energy $\hbar\omega$ by the electron, 2) migration of the electron to the cathode surface including e^--e^- scattering, and 3) ballistic emission subject to electron kinematics at the boundary. The kinetic energy of emitted electrons is $\hbar\omega$ - Φ_{eff} , but the direction of the photoelectron momentum is uniformly distributed in half space, and only those photoelectrons

[7] In ultrafast electron microscopy, one does make use of field emission tips which are photo excited by a femtosecond laser. See Reed[], for example.

with a sufficiently large momentum component normal to the metal surface will be emitted. There thus exists a "cut-off" angle φ_{max} relative to the surface normal beyond which no electrons are emitted. From kinematical considerations at the photocathode boundary that result in an equation similar to Snell's law in optics, it can be shown that φ_{max} is given by [35,36,37]

$$\cos\varphi_{max} = \sqrt{\frac{E_F + \phi_{eff}}{E_F + \hbar\omega}} \tag{3.1}$$

where E_F is the Fermi energy of the photocathode material. The transverse normalised emittance $\varepsilon_{n,x}$ of the photoelectron beam can be calculated using the three step model and assuming a Fermi-Dirac electron distribution for the cathode material. Based on this, Dowell and Schmerge have derived the following formula that is valid for metal photocathodes [37]:

$$\varepsilon_{n,x} = \sigma_{x,pc}\sqrt{\frac{\hbar\omega - \phi_{eff}}{3mc^2}} \tag{3.2}$$

Here, the rms radius of the photocathode emission region is denoted by $\sigma_{x,pc}$. From this, it is clear that $\varepsilon_{n,x}$ decreases as the photon energy approaches the work function, and doing so is highly desirable since this increases the transverse coherence length in diffraction experiments (see section 2.2.3). In practise, there must be a small excess photon energy above the cathode work function in order to get sufficient quantum efficiency, and there is in fact an inevitable trade-off between emittance and quantum efficiency requirements [37]. Typical values for the excess photon energy above the work function are around 0.5 eV. The emittance due to this excess energy spread is also known as the "thermal emittance" of the photocathode. It is the dominant factor in determining the transverse coherence length of the beam (see Section 2.2.3).

While the transverse component of the initial momentum spread at the photocathode determines the transverse coherence of the beam, the longitudinal momentum spread, which is on the same order of magnitude as its transverse counterpart, can contribute to temporal expansion of femtosecond electron pulses. This is a well known phenomenon in streak camera technology, and the rms temporal spread $\sigma_{t,acc}$ arising from the longitudinal rms energy spread at the photocathode $\Delta E_{k,ph}$ in the acceleration region can be estimated from elementary equations of motion (disregarding relativistic effects) as

$$\sigma_{t,acc} = \frac{\sqrt{2m\Delta E_{k,ph}}}{eE} \tag{3.3}$$

where E is the extraction field strength. The temporal broadening due to the initial photoelectron energy spread is thus inversely proportional to E. For a typical value of $\Delta E_{k,ph}$ =

40 meV corresponding to a FWHM energy spread of 95 meV as obtained by Janzen et al. [38], the FWHM temporal broadening assuming an extraction field of 10 MV/m is about 100 fs. With a desired pulse length on the order of 100 fs, it is clear that UED photoguns cannot employ an extraction field significantly less than 10 MV/m. Therefore one typically does away with electron gun features such as a Wehnelt cylinder which would lengthen the acceleration distance, leading to a smaller extraction field strength.

After emerging from the photogun, the electron pulse broadens further due to its energy spread. This time taking into account relativity, one differentiates the electron kinetic energy $E_k = (\gamma - 1)mc^2$ with respect to the velocity v_z, thereby obtaining the following relationship between the bunch energy spread ΔE_k in terms of the bunch velocity spread Δv_z in the laboratory frame:

$$\Delta E_k = \gamma^3 m v_z \Delta v_z \tag{3.4}$$

The temporal spreading of the electron pulse in the drift region $\sigma_{t,d}$ due to its energy spread ΔE_k is thus

$$\sigma_{t,d} = \frac{\tau_d \Delta v_z}{v_z} = \frac{\tau_d \Delta E_k}{\gamma^3 m v_z^2} \tag{3.5}$$

where τ_d is the drift time. As an example, consider a 30 keV electron pulse with a photo-induced energy spread of 95 meV. Even after a relatively long propagation time of 1 ns (corresponding to a 10 cm propagation distance) $\sigma_{t,d}$ is only 1.4 fs, which is negligible compared to the pulse broadening in the acceleration region. UED guns operating in the low charge per pulse regime (e.g. single electron pulses) therefore only need a compact acceleration region and do not require to have a short drift region. Unfortunately, ΔE_k in the drift region is dominated by space charge effects even for small electron numbers per pulse, and the resultant broadening increases rapidly with electron number, as discussed in the next section.

3.1.3 The Effect of Space Charge

Multi-electron bunches suffer from broadening in the longitudinal (temporal) and radial direction due to e^--e^- forces. Computation of the temporal evolution of such pulses is a many body problem that in general must be solved by particle tracking algorithms, as will be described in Section 3.2. Here, the aim is to convey a predominantly qualitative picture of the nature and evolution of space charge dominated electron bunches in UED. The behaviour of bunches with small electron numbers is largely determined by the spatial and momentum distribution at the region of photoemission. Since these distributions are typically Gaussian, and will remain so in the absence of space charge effects, a detailed model of UED bunch

propagation based on Gaussian functions has been developed [39]. With the pulse charge increasing into the 10^4 electrons range, however, particle simulations predicted a spatial particle distribution that became increasingly flat top while the momentum distribution developed a markedly linear correlation with position [40]. These observations, which could no longer be attributed to initial photoelectron distributions, received a solid theoretical basis when Luiten et al. [41] showed that highly charged electron bunches that start out in the pancake regime, ideally with a "half circle" radial profile[8], will under favourable conditions evolve into a hard edged uniformly filled ellipsoidal shape. Ellipsoidal bunches are well known in particle beam physics for their desirable properties [42,43,31]: the space charge forces in these bunches are linear in all directions, implying linear space charge induced momentum-position correlations and thus a large degree of normalised emittance conservation. On the one hand, this means that the transverse emittance and hence the transverse coherence length should be insensitive to high bunch charges. On the other hand, the linear nature of the longitudinal phase space holds the promise of excellent compressibility of these bunches. This is the basis for single shot UED sources that employ compressed electron bunches, as discussed in Chapter 6.

In the context of compact UED sources without compression, the aforementioned quasi-ellipsoidal nature of UED pulses suggests that these pulses can be conveniently described as ellipsoidal bunches for a qualitative analysis. In particular, one is interested in estimating the rate of temporal broadening that can be expected in UED pulses with a certain initial pulse radius and charge. Equation 3.5 gives the temporal broadening in terms of the energy spread of the bunch, and therefore it remains to estimate ΔE_k from the electrostatic potential energy of the bunch. For a spheroidal pancake charge distribution (half circle radial symmetric pancake distribution) the total potential energy is given by [44]

$$U_{p,disc} = \frac{3Q^2}{40\varepsilon_0 r} \tag{3.6}$$

where Q is the charge, ε_0 the free space permittivity and r the radius of the distribution. The maximum possible rms energy spread in the bunch rest frame that can arise as a result of this potential energy is equal to the average potential energy per electron given by

$$\Delta E_{k,max} = \frac{3e^2 N}{40\varepsilon_0 r} \tag{3.7}$$

[8] In practise it turns out that the requirement of a "half circle" profile is not critical for typical UED bunch parameters, and good results can be obtained with radial uniform or truncated Gaussian profiles [44,94]

where N is the electron number. With the velocity spread in the laboratory frame given in terms of the bunch frame velocity spread by $\Delta v_z = \gamma^{-2}\Delta v_b$ for $v_b << v_z$ and $\Delta v_b = (2\Delta E_{k,max}/m)^{1/2}$, Equation 3.5 yields the maximum possible space charge induced de-bunching as:

$$\sigma_{t,sc} \leq \frac{\tau_d}{\gamma^2 v_z}\sqrt{\frac{2\Delta E_{k,max}}{m}} = \frac{e\tau_d}{\gamma^2 v_z}\sqrt{\frac{3N}{20\varepsilon_0 mr}} \tag{3.8}$$

For example, consider a 30 keV electron pulse generated with an initial pulse radius of 50 μm containing 10^4 electrons. After a 3 cm propagation distance (300 ps flight time) Equation 3.8 predicts the FWHM temporal spread to be about 2 ps. Fortunately, Equation 3.8 represents an over-estimation of the actual temporal duration for two reasons: 1) the energy spread only reaches the value assumed by Equation 3.8 after the pulse is fully expanded and 2) bunch expansion inside the acceleration region results in electrons at the front of the bunch spending less time in the acceleration field than those at the back, and thus the energy spread of the bunch is significantly reduced upon emerging from the gun aperture (see section 3.3 and reference [44]). Nonetheless, for highly charged electron pulses ($N \sim 10^4$) $\sigma_{t,sc}$ dominates the temporal duration and Equation 3.8 in addition to Equation 3.3 determines the gun design parameters. Although Equation 3.8 is in quantitative disagreement with actual pulse durations expected from simulations (see Section 3.3), it is useful in estimating how the temporal duration of space charge dominated pulses scales with electron number, initial pulse radius, time of flight and electron energy. Since the transverse normalised emittance of the pulse is proportional to r, the initial spot size should be as small as possible. This is however in conflict with pulse duration considerations as $\sigma_{t,sc}$ scales with $r^{-1/2}$. Therefore, UED gun design involves a trade-off between spatial resolution of the diffractometer as determined by the transverse normalised emittance and the temporal resolution as determined by the pulse duration. Clearly, much can be gained in terms of temporal resolution by minimising the drift time τ_d. An obvious way of doing this is to keep the drift length as short as possible, which is the reason for the compact design shown in Figure 3.1. In the sub-relativistic regime, higher bunch energy implies a larger velocity v_z, which reduces the temporal spreading through the inverse dependence of $\sigma_{t,sc}$ and τ_d on v_z. There has consequently been a trend toward higher acceleration energies in UED source design [10,45]. At relativistic energies the γ^{-2} dependence leads to strong suppression of space charge induced broadening, which is the basis for relativistic UED schemes [46,47].

While Equation 3.8 gives a good overview of design considerations for UED guns, the actual design of such a gun requires much more detailed calculations. The method of choice

in the current study is use of a particle simulation code as described in Section 3.2. The detailed gun design is given in Section 3.3.

3.2 Electron Beam Simulations

3.2.1 Particle Tracking Codes

In the early 2000's when ultrafast electron diffraction, particularly femtosecond electron diffraction, saw a phase of rapid development, researchers recognised the need for predicting the behaviour of ultrashort electron pulses with greater precision than had been necessary in the 1980's and 1990's when picosecond electron diffraction was the state of the art [48,49]. Calculation of the behaviour of an electron bunch subject to particle-particle interactions due to space charge is generally a rather complex and computationally expensive procedure. While analytical approximations for the behaviour of UED electron pulses exist [40,50,39,30], the formulas derived so far do not allow calculation of bunch evolution in arbitrary external electric and magnetic fields, and are thus of limited use as a design tool. For more practical and accurate predictions of UED bunch properties, particle tracking codes have been developed by prominent researchers in the field. A code employing the Barnes- Hut leapfrog algorithm was used by the group which was led by R.J.D. Miller at the University of Toronto [40]. The code was never generalised to cater for relativistic electron bunches, and with the trend towards higher electron energy in UED it is of limited use [51]. The group of A.H. Zewail at Caltech have also developed an electron tracking code based on Monte Carlo techniques [52]. Many large electron accelerator facilities have developed their own electron bunch tracking codes, some of which are made available free of charge. Although such facilities operate in a very different electron energy regime than typical of UED, the particle tracking codes developed there are well suited as a design tool for current and proposed UED systems. In particular, the mentioned facilities frequently make use of bunched low emittance electron beams (e.g. those required for free electron lasers), a situation not dissimilar to that encountered in UED. Codes such as ASTRA, PARMELA and GPT (see table 4.1) have been used to predict electron pulse durations that can be compared with measurements [47,32,53,54,55]. Table 4.1 gives an overview of some of the important electron bunch simulation codes that are available.

An exact simulation of an electron beam would be to numerically calculate the trajectories of each electron subject to the electromagnetic fields of both the beamline elements as well as the sum of all the electromagnetic fields (including radiative effects) due to the other electrons. For electron bunches typical of synchrotron facilities (up to nC bunch

charges) the exact simulation mentioned above would be a completely intractable problem. Even for the much smaller electron numbers typical of UED such a simulation would take an inconveniently long time using a regular computer, although it is certainly possible and on occasion desirable to do so [52,56].

Table 4.1. Overview of important particle tracking codes that take space charge effects into account.

Code	Space charge calculation	Owner	Website	Commercial?
ASTRA (**A** **S**pace Charge **Tr**acking **A**lgorithm)	Point to cylindrical or 3D mesh	DESY (Deutsches Elektronen Synchrotron)	www.desy.de/~mpyflo/	no
CSRTrack (**C**oherent **S**ynchrotron **R**adiation **Track**)	Point to mesh consisting of Gaussian sub-bunches, 1D or 3D	DESY	www.desy.de/xfel-beam/csrtrack/	no
CPO (**C**harged **P**atricle **O**ptics)	Point to mesh or point to point	CPO Ltd	www.electronoptics.com	yes
GPT (**G**eneral **P**article **T**racer)	Point to cylindrical or 3D mesh and point to point	Pulsar Physics	www.pulsar.nl/gpt	yes
PARMELA (Phase **a**nd **R**adial **M**otion in **E**lectron **L**in**a**cs)	Point to cylindrical or 3D mesh and point to point	LANL (Los Alamos National Laboratory)	http://laacg1.lanl.gov/laacg/services/serv_access.phtml#parmela	yes
TRACK	Point to mesh	ANL (Argonne National Laboratory)	www.phy.anl.gov/atlas/TRACK/Trackv37/	no
TREDI	Monte Carlo macroparticle point to point or point to mesh	ENEA	www.tredi.enea.it/	no

Electron tracking codes capable of taking into account particle-particle interactions therefore make approximations to significantly ease the computational load. For large bunch charges (nC or pC) the individual electrons are replaced by so-called macroparticles which represent a large number of electrons and carry a corresponding charge[9]. In addition, the macroparticles are grouped into cells. The forces on each individual macroparticle are then approximated as arising from a dynamic grid of cells representing the ensemble. The details of how the macroparticles are grouped, how the electromagnetic field is calculated from the grid and how the resulting particle dynamics is determined vary from code to code, and usually the codes have many user defined parameters and methods. The particle trajectories are computed by numerically integrating the motion of all particles in a cell over discrete time steps subject to all particles in the cell experiencing the same force due to the effect of all other cells in the grid. Space charge tracking algorithms typically compute the forces due to cells by computing the potential using a Green's function method. The 3D space charge tracking routines of

[9] In UED where the electron number per pulse is typically on the order of 10^4, it is feasible to set the number of macroparticles equal to the number of electrons.

ASTRA, PARMELA, and GPT, for instance, work in this way. Simplifications of the computations in bunch tracking codes are also effected by specialising certain routines to cater only for the dominant physical phenomenon present; for instance, some routines may be specialised to deal accurately with space charge forces (ASTRA, CPO), while codes such as CSRTrack and certain sub-routines in GPT are better suited for calculating coherent synchrotron radiation effects that occur in bending magnet sections of a beamline [57,58].

3.2.2 Description of the ASTRA code

The simulation program of choice in the present study is the ASTRA code originally developed by Klaus Floettmann at DESY. ASTRA is freely available [59], user friendly and ideally suited for simulating the propagation of bunched electron beams emanating from photoguns and propagating through radial symmetric beamline elements. To perform a simulation, an initial bunch distribution must be specified; this can be done either as a 3D spatial distribution or as a transverse spatial and longitudinal temporal distribution so that the photoemission process from a cathode can be simulated. Details of the photoemission process including the Fermi-Dirac nature of the initial energy distribution, Schottky barrier lowering of the cathode material work function as well as image charge effects during the emission process of highly charged bunches are handled by ASTRA. The current version of ASTRA can only simulate cathode image charge effects for circular beams [60].

External radial symmetric fields due to cylindrical standing wave cavities and solenoid lenses are easily fed into the code through on-axis field profiles that can be measured or generated using for example the Poisson/Superfish set of codes [61]. For standing wave cavities, the static on-axis field profile must be provided, and by specifying a phase and frequency ASTRA computes the resultant electromagnetic field. More complicated electromagnetic fields such as travelling waves and non-sinusoidal waves can be implemented by overlapping a suitable number of sinusoidal standing wave cavities. It is also possible to feed arbitrary 3D fields into ASTRA so that beamline elements lacking radial symmetry such as deflecting mode cavities can be included. Future versions of ASTRA are supposed to also implement bending magnets.

For the space charge calculation there are two algorithms to choose from: cylindrical symmetric and full three dimensional (“3D FFT” [60]). In the cylindrical symmetric algorithm, the system is Lorentz transformed into the bunch rest frame and the electron bunch is divided into a nominal number of rings in the radial direction and slices in the longitudinal direction. Each ring shaped cell is then treated as having a uniform volume charge, and the electric field at the centre points of each cell due to all other rings is computed. The resultant

lookup table is then interpolated to calculate the electric field at each point, which is Lorentz transformed back into the laboratory frame so that the space charge field is treated on equal footing with the external electric and magnetic fields. The full 3D space charge calculation is done in a similar way, except that the bunch is divided into Cartesian cells with a nominal number of divisions in the x, y and z directions [60]. The space charge forces are calculated by approximating the charge contained in each cell by a set of three line charges along the fundamental axes of the cell. The tracking of macroparticles is done via a 4^{th} order Runge-Kutta integration which is performed by taking into account the external fields and the space charge field which is updated regularly as the bunch shape evolves.

3.3 Design of an Electron Gun for UED Experiments

The discussions of Sections 2.2, 3.1.2, 3.1.3 and 3.2 are now applied to the design of a compact UED source suitable for generating highly charged 30 keV electron bunches (10^3 – 10^4 e^-/shot) with a transverse coherence length of about 2 nm, rms radius of less than 100 μm and FWHM temporal duration of less than 300 fs. It should be emphasised here that specifying temporal duration and electron number per pulse alone is not sufficient for judging the relative merit of the pulse performance in a UED experiment. When it comes to samples that cannot be repeatedly excited and probed the important beam parameter in UED experiments is the transverse brightness of the beam (apart from temporal duration). Transverse Brightness is defined as the number of electrons per unit cross sectional area per unit of transverse coherence length (which is crucial for spatial resolution) that can be delivered (see Section 2.1).

The basic gun design is given in Figure 3.1 and it remains to choose reasonable gun and magnetic lens dimensions that can be simulated using the ASTRA code. The following design choices were made: for 30 keV electrons an acceleration distance of 4 mm is used with an extraction opening of radius 1 mm. The magnetic lens geometry was designed such that the magnetic gap and bore diameter are 5 mm and 7 mm respectively, with the length of the entire lens equal to 18 mm (see Section 4.3.2 and Figure 4.8 for details of the lens geometry). The gun-facing side of the lens is positioned 11 mm from the cathode, and thus the minimal cathode-sample distance is about 30 mm.

The simulation parameters are now discussed. In order to meet the pulse radius specification of 100 μm at the sample, a suitable photoemission spot size needs to be chosen. Using a Gaussian transverse profile, it was found via simulations that an rms emission spot radius of 25 μm is suitable. The energy spread of photo emitted electrons was modelled in

accordance with the discussion in Section 3.1.2, assuming an excess photon energy above the work function of $\hbar\omega$ - Φ_{eff} = 0.55 eV, as obtained for the present setup in Section 4.5.3. Equation 3.2 then predicts a thermal emittance of 15 π nm, and assuming conservation of thermal emittance Equation 2.13 yields a transverse coherence length in excess of 2 nm, which meets the specifications. The temporal emission profile of electrons was assumed to be Gaussian with a FWHM duration of 120 fs.

The results are shown in the figures below. In the initial stages, the temporal duration of the pulses increases with a parabola-like shape, but at larger propagation times becomes asymptotic to a straight line, the latter being particularly evident for the pulse containing 10000 electrons (Figure 3.2). This is in good agreement with what has been observed from simulations previously and predicted by analytical models [40,50,39]. It is also evident that the space charge induced broadening increases appreciably with pulse charge; if a FWHM duration of less than 300 fs is desired, the pulse should not contain much more than 5000 electrons if the sample is placed at the minimal distance of 30 mm from the cathode.

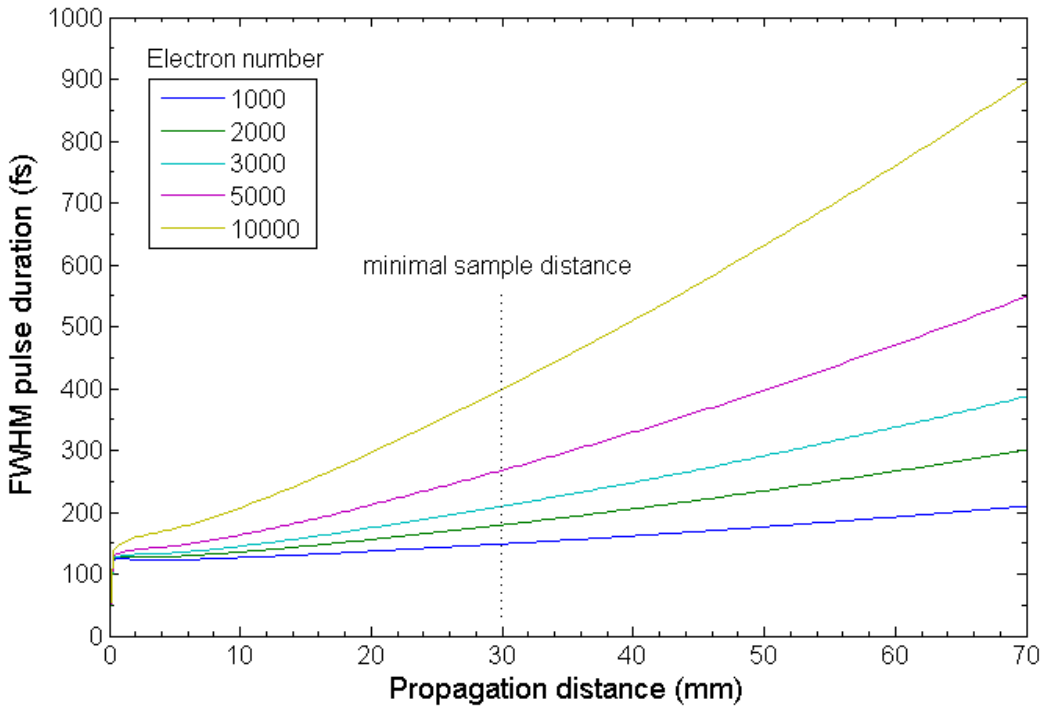

Figure 3.2. Simulated FWHM temporal duration versus propagation distance for various bunch charges. The initial rms bunch radius at the photocathode is 25 μm, the initial excess photon energy above the work function is 0.55 eV, and the bunch is accelerated to 30 keV over a distance of 4 mm. The initial temporal profile is Gaussian with a FWHM duration of 120 fs. The closest possible sample distance, determined by the setup geometry, is indicated at a distance of 30 mm. Rapid temporal spreading of the pulses is evident as the electron number per pulse is increased from 10^3 to 10^4.

The reduction of the rms energy spread at the electron gun exit that was briefly mentioned in Section 3.1.3 is clearly visible in Figure 3.3. Subsequent to this "cooling", the rms energy spread increases again due to the remaining potential energy in the pulses, eventually flattening out to an asymptotic value. Clearly, highly charged UED pulses have a much larger energy spread than static electron beams which have only the initial "thermal" energy spread present at the cathode.

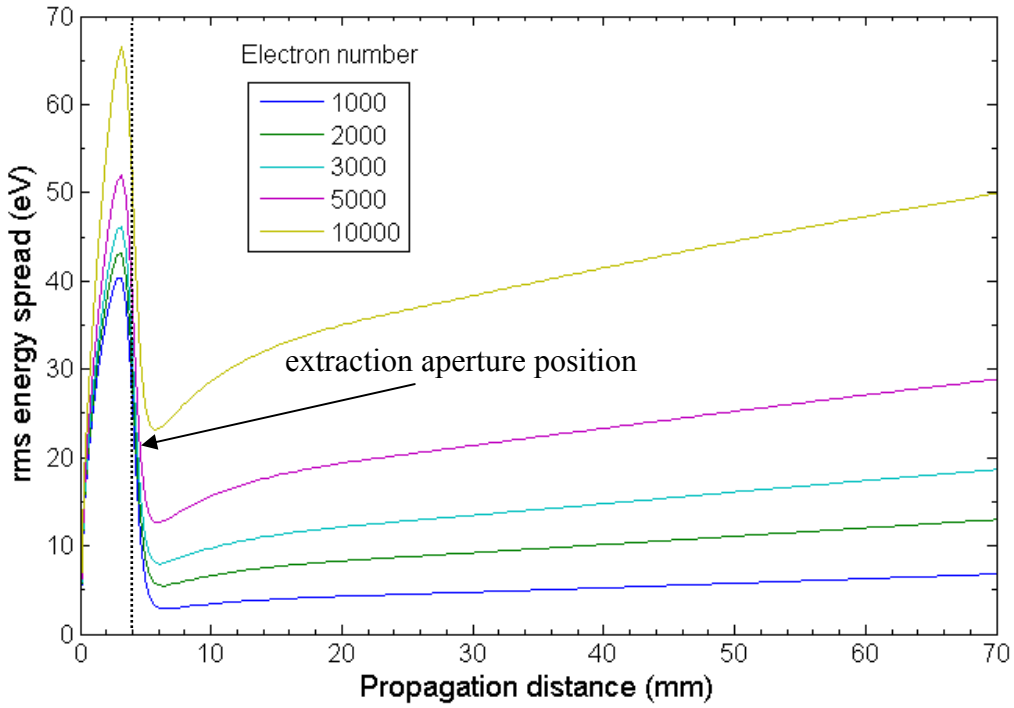

Figure 3.3. Rms energy spread versus propagation distance for the electron pulses. After photoemission, space charge expansion combined with rapid bunch centre acceleration causes a rapid increase in the rms energy spread. This energy spread is chirped to a large degree, with slower electrons trailing the faster ones. At the extraction aperture (indicated by a dotted line in the figure) the trailing electrons receive an extra momentum "kick" relative to the ones at the front due to bunch expansion inside the acceleration region, which leads to a significant reduction in the rms energy spread after emergence. This reduction in ΔE_k is highly beneficial for UED since it leads to significantly reduced de-bunching of the pulses. The remaining potential energy of the pulses is converted into energy spread in the post gun drift region. The increase of rms energy spread with electron number is apparent in this figure.

The longitudinal coherence length is determined from the longitudinal emittance and pulse duration by Equation 2.7. For 1000 e- /pulse, one obtains $L_{c,z}$ = 120 nm at the sample position (30 mm from the cathode) while for the 10000 e- /pulse one obtains $L_{c,z}$ = 34 nm. These values are considerably less than the case of static electron diffraction, where $L_{c,z} \sim 1$ μm. The

ability to observe microstructure as is possible with static RHEED is thus sacrificed in UED, but for transmission electron diffraction the sample thickness is in any case on the order of 30 nm for 30 keV beams; there should thus be no noticeable degradation of the diffraction image quality due to the lowered longitudinal coherence of UED beams (see also Michalik et al. for a detailed discussion of this issue [34]). The longitudinal emittance is also a measure of the compressibility of a bunch. The approximately linear scaling of $\varepsilon_{n,z}$ with electron number seen in Figure 3.4 implies that re- compressed highly charged electron pulses necessarily have a large energy bandwidth. The longitudinal coherence of such sources is rather small, on the order of 1 nm. Thus there are definite limits on the electron number per pulse even for compressing UED sources such as those discussed in Chapter 6. The electron gun and magnetic lens implementation that forms part of the ultrafast electron diffractometer to be described in Chapter 4 was constructed according to this design.

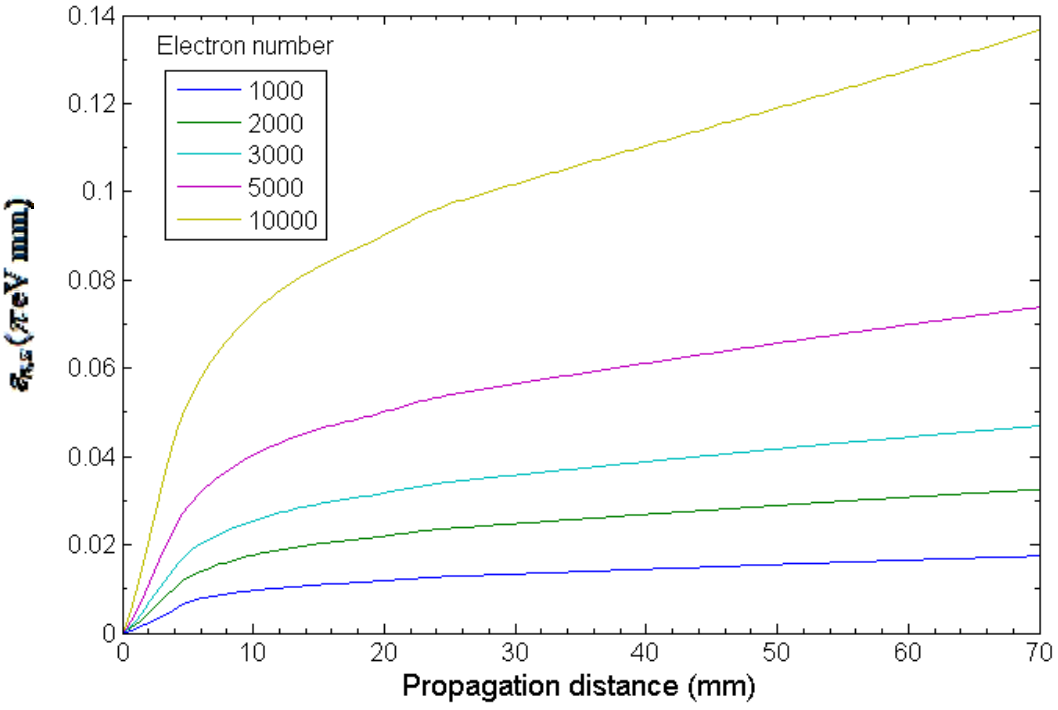

Figure 3.4. Longitudinal normalised emittance versus propagation distance. Nonlinearities in the space charge expansion result in longitudinal emittance growth that is roughly proportional to the number of electrons. This implies that the longitudinal coherence length $L_{c,z}$ decreases as the number of electrons increases, assuming the same pulse duration. It also means that the compressibility of pulses decreases with electron number, i.e. more rms energy spread is required to attain a desired pulse duration. This places brightness limits on compressing UED sources as discussed in Chapter 6.

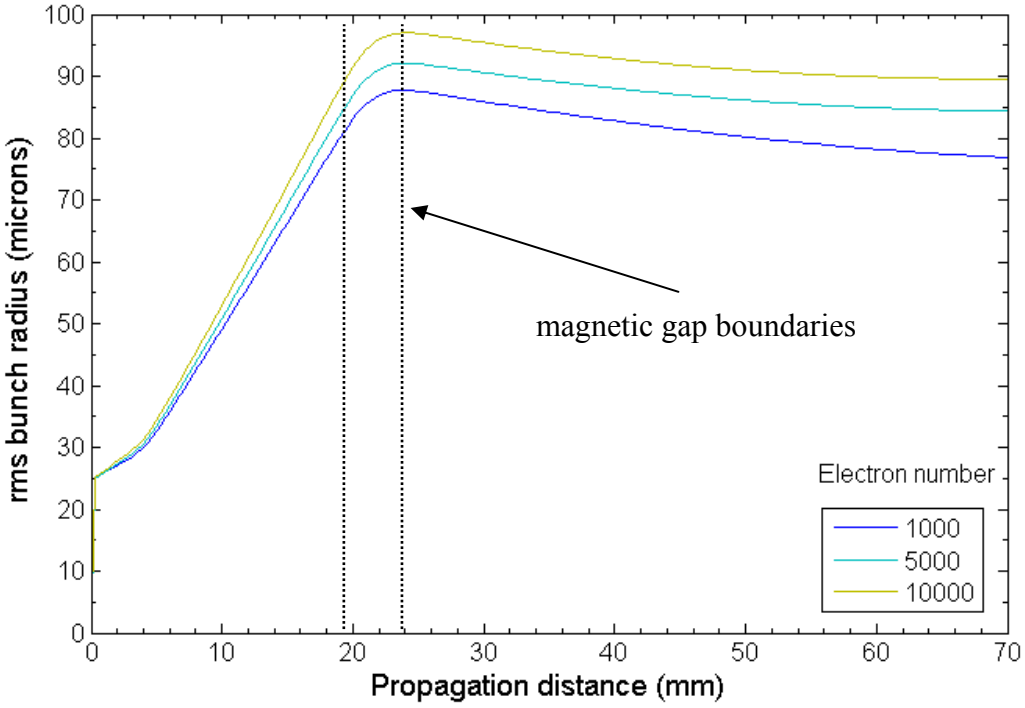

Figure 3.5. Rms bunch radius versus propagation distance. To obtain the same focussing at the sample position, the solenoid field strength was varied slightly (less than 5%). Once again, the magnetic gap boundaries are indicated by dotted lines. Evidently, a larger number of electrons leads to more pronounced radial broadening. This effect is however much less noticeable than in the longitudinal case (see Figure 3.2): increasing the number of electrons by an order of magnitude from 10^3 to 10^4 results in an increase in the rms radius of only about 10 %.

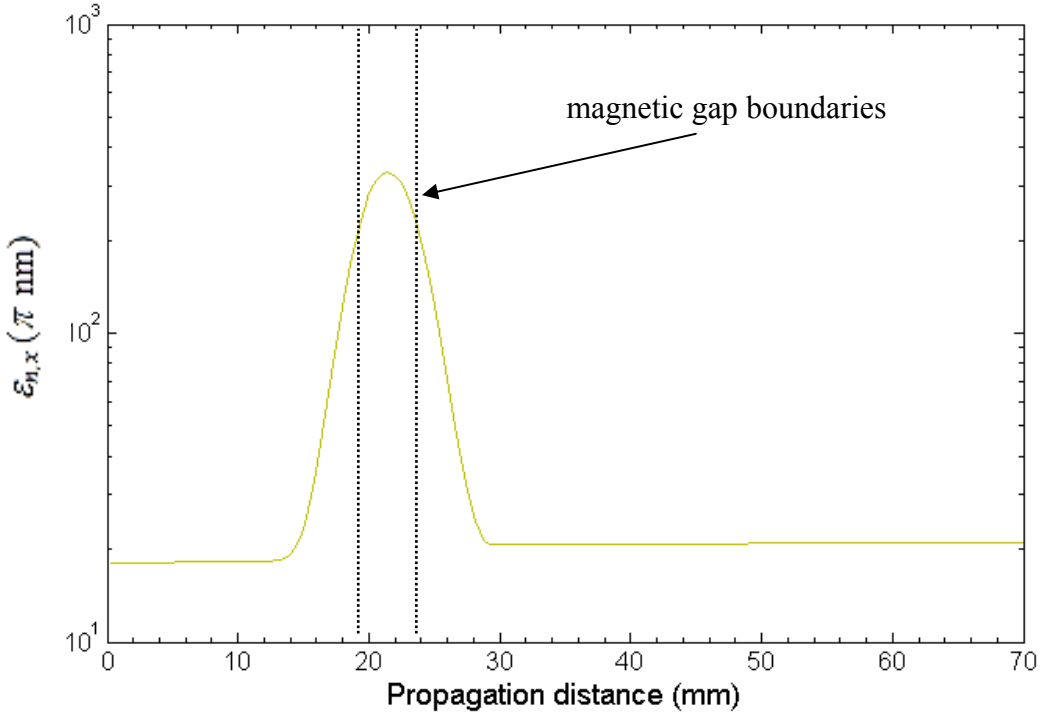

Figure 3.6. Transverse normalised emittance versus propagation distance for the bunch containing 10^4 electrons. The net increase in $\varepsilon_{n,x}$ is relatively small, and is mainly due to magnetic lens aberrations. The boundaries of the solenoid magnetic gap are indicated on the graph (see Figure 4.8 a) and b) for details of the magnetic lens geometry and field). $\varepsilon_{n,x}$ increases substantially but reversibly while inside the solenoid field. The reason for the emittance increase is the azimuthal velocity temporarily acquired by the electrons which enables the focussing action.

4. THE ULTRAFAST ELECTRON DIFFRACTOMETER

A major aspect of the current study was the research into bunched electron beam dynamics as described in Chapters 2 and 3. With the help of simulations, performed here using the ASTRA code, it has been possible to make reasonable predictions of the behaviour of ultrashort electron pulses (section 3.3). The electron gun design outlined in the previous chapter is thus predicted to deliver sub-300 fs electron pulse durations with pulse electron numbers up to 10^4. This chapter describes the details of the electron diffractometer which was constructed as part of the present study. The realisations of the electron gun and solenoid lens are of course based on the simulations described in the previous chapter. The setup as constructed and to be described in this chapter is suitable for fs time resolved electron diffraction experiments, but no pump-probe diffraction experiment has yet been performed. Static diffraction images of thin Ti foils have however been recorded and analysed as described in Section 4.4. Characterisation of the setup regarding easily measured beam parameters such as transverse beam size, angular spread and normalised emittance at the photocathode is given in Section 4.5. Temporal characterisation is considerably more challenging, and Chapter 5 is devoted to this subject.

4.1 Setup Overview and Vacuum Chamber

An overview of the UED setup as currently implemented is given in Figure 4.1. The femtosecond laser is a commercial chirped pulse amplification (CPA) system (Clark-MXR CPA 2101) with a central wavelength of 775 nm, rated pulse duration of 150 fs and 800 μJ pulse energy at a repetition rate of 1 kHz. The setup is designed to function as a pump-probe system employing a laser excitation ("pump") pulse and a high energy (30 – 50 keV) electron pulse as a "probe" to take a "snapshot" of the atomic configuration at a specific time by generating an electron diffraction pattern.

In order to get good synchronisation of pump and probe pulses, both are derived from the same pulse using a beam splitter. The probe arm beam first passes through a set of interchangeable neutral density filters (labelled "attenuator" in Figure 4.1) for intensity adjustment, where after it is sent through a pair of mirrors mounted on a translation stage which function as an optical delay line to control the relative timing of pump and probe pulses. The pulse is bound for the specially designed high energy photoelectron gun (see detailed discussion of the electron gun design in Section 4.3.1) but first the 775 nm laser pulse must be frequency tripled in a special optical arrangement (Section 4.2) so that the photon energy is sufficient to overcome the work function of the noble metal photocathode. Once

generated and accelerated, the electron pulse is collimated by a magnetic lens (Section 4.3.2) and passes through the sample where it is diffracted, producing a diffraction image on the detector. The pump pulse enters the vacuum chamber through a special broad band window (UV – NIR) and is directed toward the sample in an almost anti-parallel direction relative to the electron pulse. Since the sample for transmission geometry is typically less than 100 nm thick it is feasible to pump and probe from opposite sides of the sample. In the current setup, the pump beam is the 775 nm fundamental. Some experiments may require different excitation wavelengths, and it is possible to use for example a noncollinear optical parametric amplifier (NOPA) to generate fs laser pulses that are tuneable in the visible and near UV/ IR.

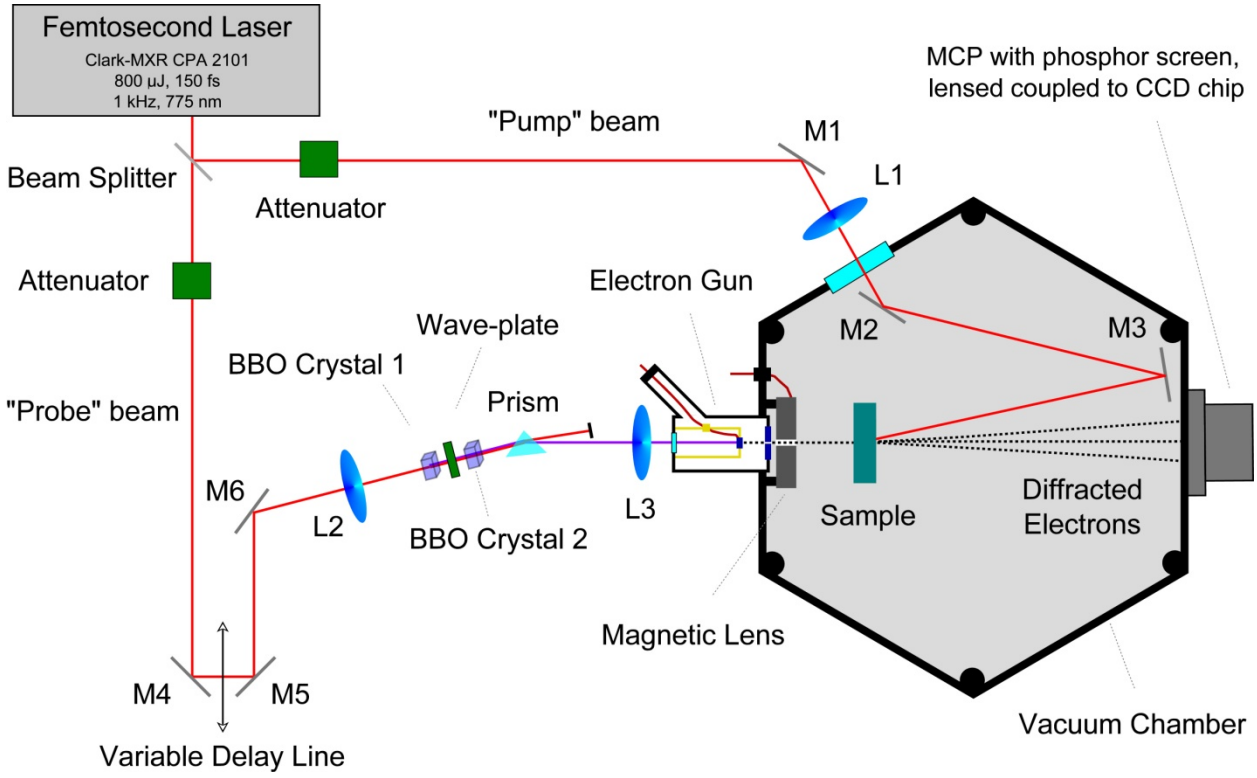

Figure 4.1. Overview of the setup capable of performing pump-probe electron diffraction experiments with fs temporal resolution. Optical lenses are labelled L and mirrors are labelled M.

The vacuum chamber itself was designed to be as flexible as possible; it consists of a hexagonal stainless steel frame with a diameter of about 50 cm. The six side walls are made from identical aluminium plates that are fitted with O-rings around the periphery, and as such are easily interchangeable (see Figure 4.2 a)). The price to pay for this flexibility is the fact that it is difficult to get a really good vacuum. Thus far the lowest pressure achieved was about 10^{-5} mbar. Currently a very small turbomolecular pump (Leybold TW70H) with a pumping capacity of only 60 l/s is employed, but recently this was replaced with a larger

turbomolecular pump that has a capacity of 700 l/s (Oerlikon Turbovac SL 700). The vacuum reaches the 10^{-6} mbar range with this improvement, and is expected to attain the 10^{-7} mbar range after some leak management efforts.

No pump probe diffraction experiment has so far been performed during this study. Experience with the relative timing of laser pulses and electron pulses on a 100 fs timescale was however gained from the streak camera experiment described in Chapter 5. Static diffraction patterns from a titanium foil were also recorded and analysed, see Section 4.4.

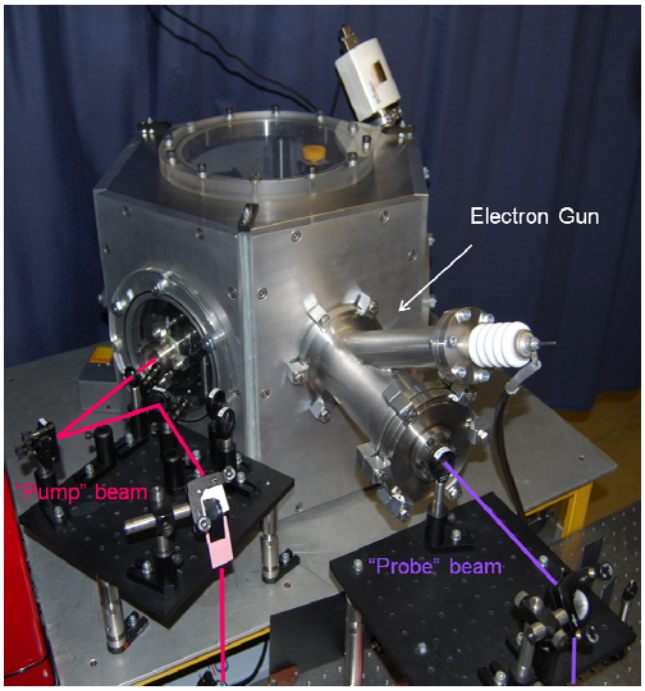

Figure 4.2. Vacuum chamber with electron gun and pump beam entrance window visible in front. Both the pump beam and UV gun trigger beam paths are visualised.

4.2 UV pulse Generation and Characterisation

In order to be able to generate photoelectrons from noble metal photocathodes (silver or gold) it is necessary to have a light beam with photon energy in the 4-5 eV range in order to exceed the workfunction of these metals. The Clark CPA delivers pulses with a wavelength of 775 nm (1.61 eV); frequency tripling of the pulses would therefore deliver a photon energy of 4.83 eV which is sufficient. An efficient way to achieve the tripling is by the two-step process of first doubling the fundamental in a nonlinear crystal and then overlapping the remainder of the fundamental with the frequency doubled light in a second nonlinear crystal to obtain the third harmonic via sum frequency generation. The details are as follows (see Figure 4.3): A

lens with f = 500 mm focuses the 775 nm fundamental roughly onto the assembly consisting of two beta barium borate (BBO) crystals and a wave plate. The focussing is required in order to get sufficient intensity for the nonlinear processes to take place. Type I phase matching is used in both crystals, and therefore the incoming rays to be frequency mixed must both have ordinary (o) polarisation, while the outgoing sum frequency ray will have extraordinary (e) polarisation. Both BBO crystals, labelled crystal 1 and crystal 2 in Figure 4.3, are cut at an angle of 30°. This angle is optimal for the phase matching of the frequency doubling process of the 775 nm wavelength, and after passing through crystal 1, both the fundamental with o-polarisation and the second harmonic (388 nm) with e-polarisation emerge (in Figure 4.3 the polarisation direction is indicated by the arrows and dots). In order to meet the phase matching conditions in crystal 2 (both incoming rays must be o-polarised), the waveplate is needed. A $\lambda/2$ plate for the 775 nm wavelength was chosen so that the fundamental is rotated by 90° but the second harmonic by 180° which means that both wavelengths have the same polarisation as they enter crystal 2, which is rotated by 28° such that the optic axis lies at an angle of 28° + 30° = 58° to the incoming polarisation direction. This angle is required for the phase matching of the sum frequency generation. The third harmonic at 258 nm emerges along with the remainder of the fundamental and second harmonic. Since the beam was focussed by a 500 mm lens, it needs to be collimated and this is done by the focussing mirror (labelled simply as “mirror” in Figure 4.3). What remains is to filter out the second and third harmonic wavelengths, and this is done by dispersing the beam with a MgF prism. With the current setup, the attainable average UV power is in the 1 μW to 80 μW range for an input fundamental power ranging from 1 mW to 30 mW. The intensity of the fundamental can currently only be varied in discrete steps using a set of neutral density filters. Continuous adjustment of the UV power is however possible by rotating the waveplate, thereby varying the efficiency of the third harmonic generation. The electron number per pulse that can be attained with the given maximum UV power was found to be highly variable, but electron numbers as high as 70 000 per pulse have been achieved, which is more than sufficient for present purposes.

In order to generate high quality electron pulses with a small transverse emittance, the UV beam must be focussed to a small spot onto the photocathode. In the present setup this is done using a lens with focal length 300 mm. In order to accurately simulate the electron beam parameters, the focal spot size and profile of the UV beam must be known. The test setup to measure the UV beam size and profile as a function of distance is shown in Figure 4.4. A phosphor screen is used to make the UV spot visible, which is then imaged via a single lens (objective lens indicated in Figure 4.4) onto a CCD detector. The entire assembly is mounted

on the same steel rod an can be moved in unison using the translation stage. The transverse beam profile was found to be Gaussian, and the FWHM width is plotted versus longitudinal position in Figure 4.5. The $z = 0$ position corresponds to a distance of 330 mm from the lens; the focal distance is not equal to 300 mm due to imperfect collimation of the incident UV beam. In the UED setup the distance from lens to cathode is 300 mm, and from the graph it follows that the FWHM UV spot size on the photocathode must be about 190 μm. This is not particularly small, and leads to an excessively large beam size at the sample; a smaller spot size will be used in future. This can be achieved by expanding the UV beam to a larger diameter before it enters the 300 mm focussing lens.

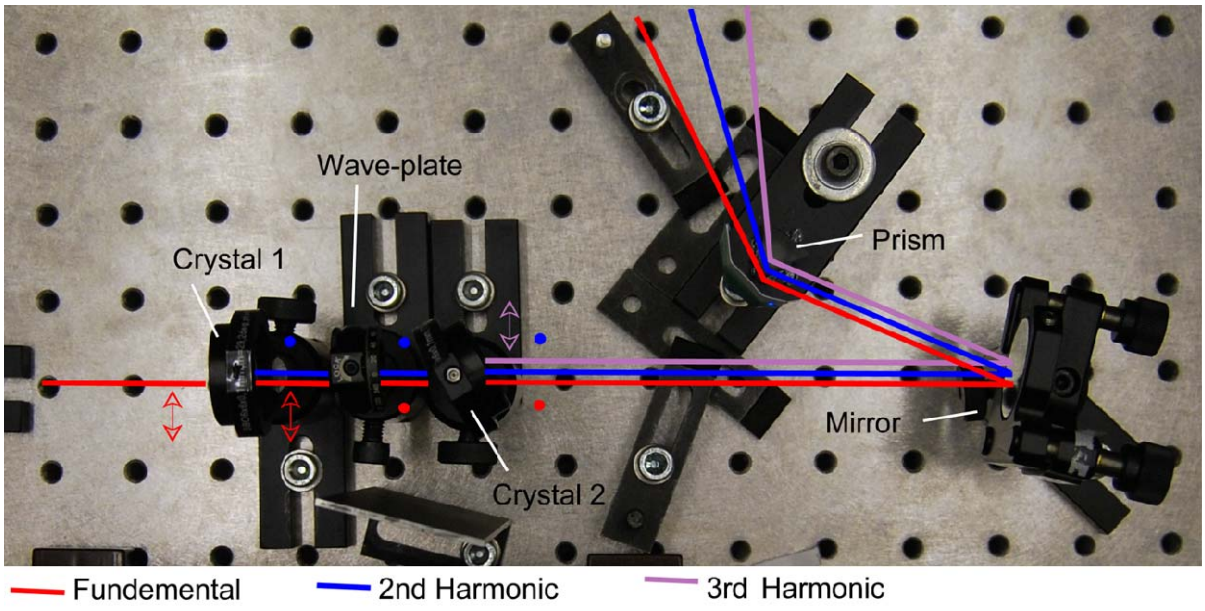

Figure 4.3. Experimental setup for frequency tripling of the 775 nm fundamental. The polarisation direction is horizontal in case of arrows and vertical (out of the page) in case of dots.

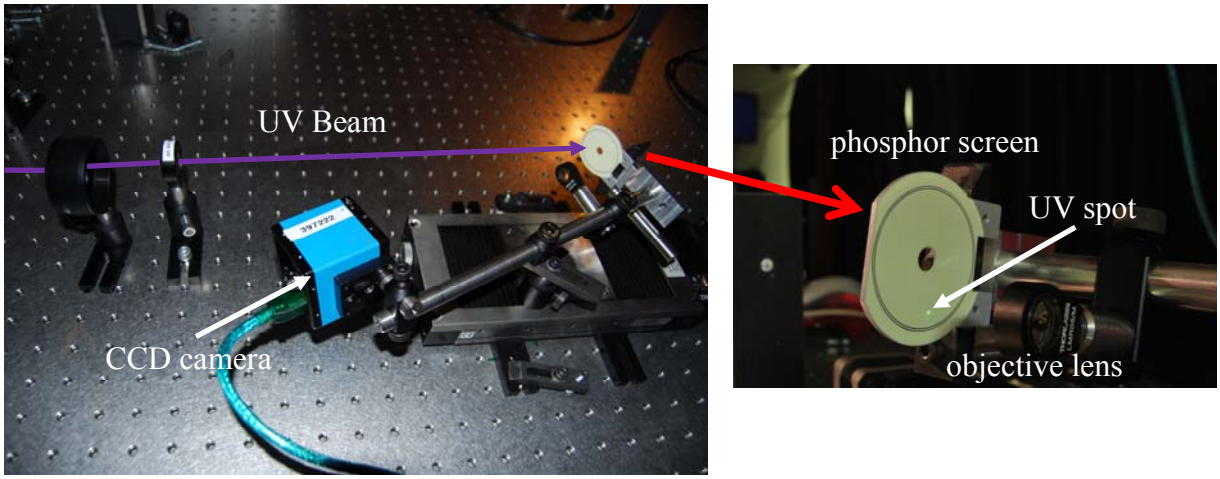

Figure 4.4. Test setup to characterise the transverse profile of the UV beam. An assembly consisting of a phosphor screen, imaging lens and CCD camera is mounted on a translation stage in order to visualise the transverse UV beam profile as a function of displacement from the 300 mm focussing lens.

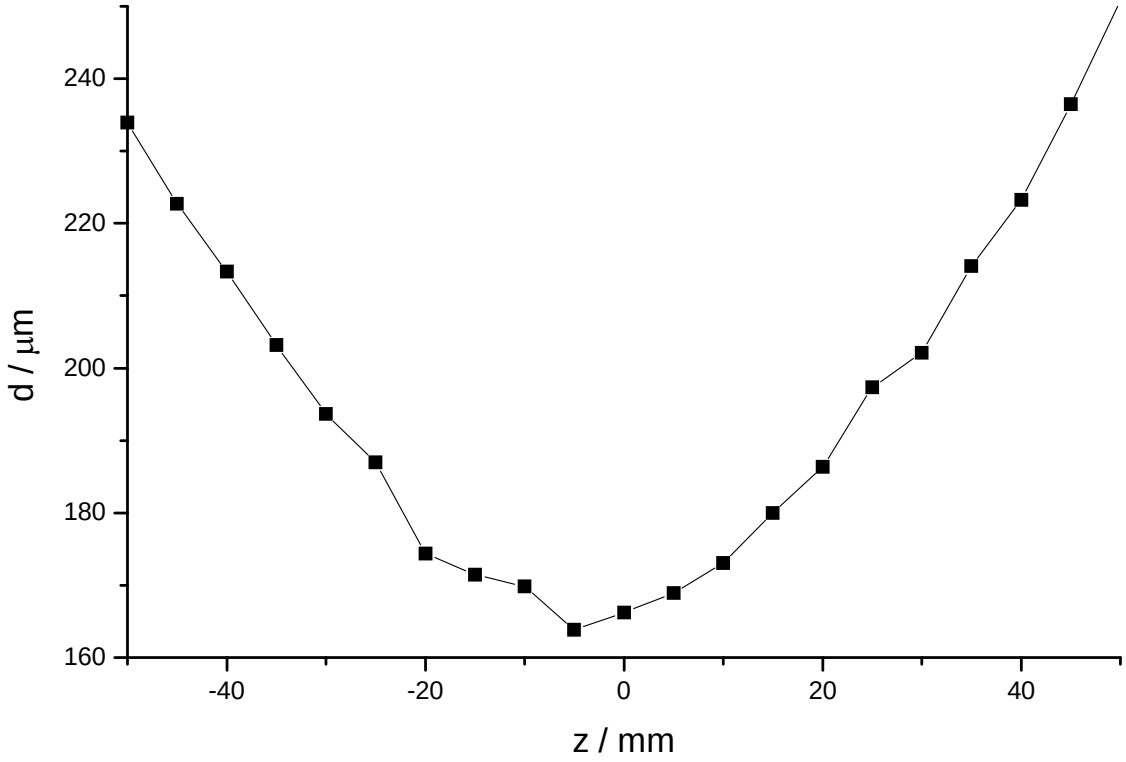

Figure 4.5. FWHM diameter of the UV beam as a function of longitudinal distance z. The $z = 0$ position corresponds to a distance of 330 mm from the lens.

4.3 The Electron Beamline

4.3.1 Electron Gun

The electron gun is the single most specialized component of an UED setup, and much care was taken in its design. As discussed in Section 3.1.1, a short acceleration and propagation distance is necessary. In addition, instead of using a heated filament, the gun is to be photo triggered by the optical setup described in Section3.1.1. The electron gun design which was developed in this study is based on the pioneering work of B.J. Siwick [12], and is shown in Figure 4.6. The schematic cross section is depicted in Figure 4.6 a) while Figure 4.6 b) is a 3D rendition of the design. The gun features a Rogowski shaped cathode [62] which ensures that the electric field strength in the electron acceleration region (up to 10 kV/mm) is not exceeded anywhere else on the cathode head for a cathode potential up to 60 kV. In addition, this critical field is not exceeded anywhere else in the geometry if a cathode voltage less than 60 kV is used (see Figure 4.7). This is important to prevent arcing caused by breakdown of metal surfaces in a vacuum [63]. The Rogowski electrode is mechanically supported and electrically isolated from ground by a Macor tube through which the UV laser pulse that enters the vacuum chamber through a quartz window can reach the back-illuminated photocathode (pc). The pc is placed inside the Rogowski electrode and secured with silver paint. It consists of a highly polished quartz disc onto which a 25 nm gold layer was deposited on top of a 5 nm titanium adhesion layer using electron beam evaporation[10] (see Figure 4.6 d)). A thicker gold layer of about 1000 nm was deposited on the outside of the glass disc and around the edges to ensure good electrical contact with the Rogowski electrode. The most common choice for the photocathode material in UED is silver or gold [38,64,45]. The effective work function of thin films of these metals on quartz or sapphire is typically in the 4-5 eV range [65] and therefore well matched with the photon energy delivered by frequency tripled Ti:Sapphire lasers which can range in wavelength from about 760 nm to 820 nm (corresponding to frequency tripled photon energies of 4.92 eV and 4.55 eV respectively). An adhesion layer between the silver/ gold and the transparent substrate is not essential but can improve the durability of the pc, as reported by Janzen et al. [38].

The electrons are accelerated from the cathode to the anode through a distance of about 3 mm. The anode is a loose-fitting lid and is secured to the electron gun via four screws. The position of the anode is variable in all directions to a certain extent. A central hole of 2 mm diameter serves to extract the electrons. The finished electron gun is shown in Figure 4.6 c) and the Rogowski shaped cathode in Figure 4.6 d). The entire gun was machined from non

[10] The E- beam deposition was done courtesy of Sergio Coelho and F. Danie Auret at the University of Pretoria.

magnetic stainless steel, and the interior surfaces were carefully polished to prevent vacuum breakdown. The “punch through” of potential lines at the extraction opening causes de-focussing of the electron beam similar to an electrostatic aperture lens (briefly discussed in Section 4.3.2) and can be mitigated through use of an extraction mesh [12,38]. However, such a mesh randomises the electron trajectories, leading to unacceptably large transverse emittance growth [66]. It is therefore preferable to use a gridless anode extraction aperture and re-focus the beam with a stronger collimating lens. More complicated (gridless) electron gun geometries can be designed that do not cause de-focussing of the electron beam [44].

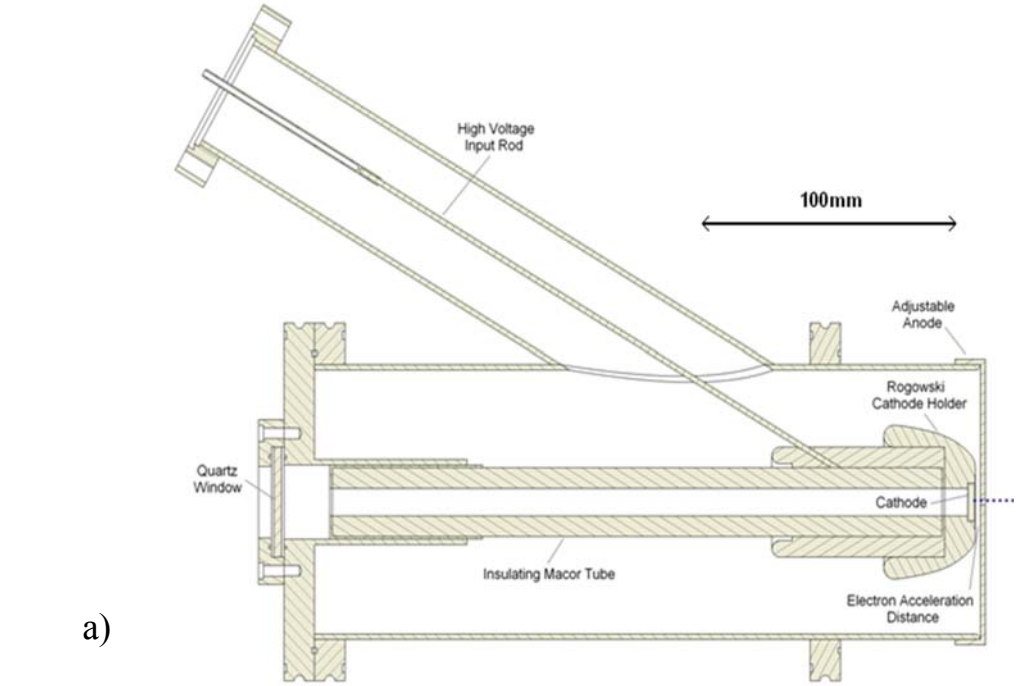

a)

b)

c)

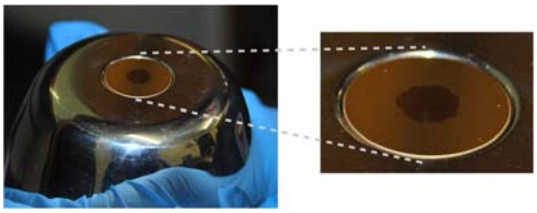

d)

Figure 4.6. UED gun design. a) schematic cross section, b) exploded 3 dimensional rendition of the gun design, c) finished electron gun and d) close-up of the Rogowski electrode with fitted photocathode.

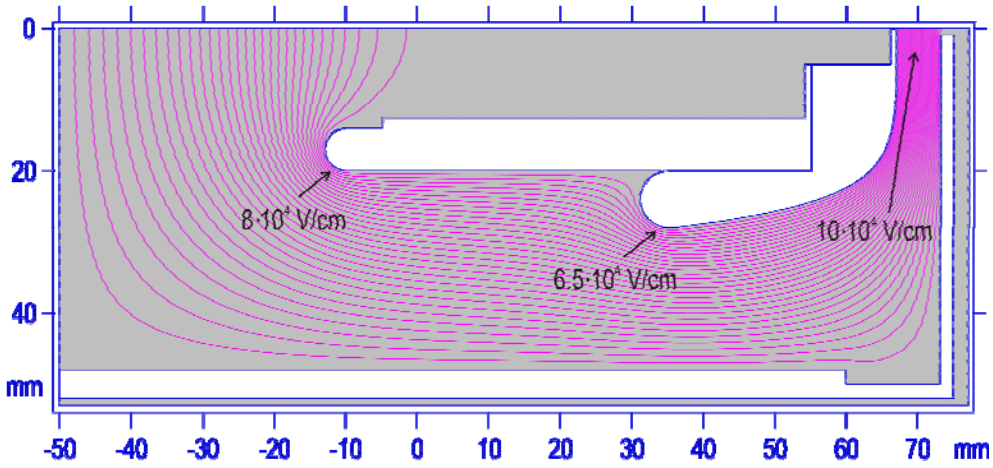

Figure 4.7. Electric potential simulation of the gun geometry

4.3.2 Magnetic Lens

The collimating lens of the electron diffractometer, like the electron gun, also requires a specialised design to help minimise the propagation time of the electron pulses. This implies designing a lens that is as short as possible in the propagation direction of the electron beam. In the electron energy regime considered for this study (30- 50 keV) there are two lens types that can be considered: electrostatic and magnetic [67]. An electrostatic aperture lens, also called an Einzel lens, consists of a charged electrode sandwiched between two grounded plates, complete with apertures for the electron beam to pass through. The polarity of the charge on the centre electrode determines whether the lens is a converging or diverging lens. In the present case a converging lens is required, and thus a negative electrode potential. As was discussed in Section 4.3.1, the beam divergence of the electron gun is relatively large due to space charge forces and the high electric field strength required for speedy electron pulse acceleration, which causes a strong de-focussing effect at the extraction aperture. For an Einzel lens to be effective, it turns out that a very large electrode potential in excess of 5 kV is required. Since this potential would in addition to the focussing effect also reduce the average velocity of the pulses, it is clear that an Einzel lens is not the optimal choice for the present UED gun.

It was therefore decided to make use of a magnetic solenoid lens. Solenoid lenses consist of a circular coil wound inside a casing of material with a high magnetic permeability (see Figure 4.8 a)). A gap in the magnetic casing surrounding a central circular opening produces a

cylindrical symmetric magnetic field with radial and axial (*z*-direction) components. The focussing action is second order: incident off-axis electrons acquire an azimuthal velocity through interaction with the radial magnetic field component. Interaction of this azimuthal velocity component with the axial magnetic field component results in a Lorentz force directed toward the *z*-axis, regardless of the magnetic field polarity or electric charge of the beam particles. It can be shown that the azimuthal velocity vanishes upon the beam exiting the solenoid field [68] so that the net effect is a purely focussing one. Implementation of a solenoid lens in a compact UED electron diffractometer poses some special challenges. To keep the propagation distance as short as possible, it is advantageous to place the lens inside the vacuum chamber [12]. This is avoided in conventional electron optics systems due to the fact that regular magnet wire is not high vacuum compatible and placing magnet wire in a vacuum leads to cooling problems. The special design shown in Figure 4.8 a) circumvents these difficulties by placing the magnet wire inside a casing that is hermetically sealed with low outgassing epoxy (scotchweld #2216). The thermal power dissipated by the lens at the design current of 1.25 A is only about 8 W at a lens temperature of 50 °C[11], and therefore passive cooling via an aluminium bracket which doubles up as a lens mount and is thermally coupled to the base plate of the vacuum chamber is sufficient (see Figure 4.8 d)). The temperature of the magnet coil can be monitored in situ by measuring the winding resistance, and during normal operation in a vacuum the temperature stabilises at about 50 °C, well below the maximum temperature rating of the epoxy (80 °C). The lens is shown in Figure 4.8 c). The magnetic casing was machined from mild steel, and the coil consists of 586 turns wound from 0.56 mm diameter enamelled copper wire. The maximum magnetic field observed in the simulation (Figure 4.8 b)) is about 400 mT with an assumed wire current of 2 A, well below the saturation field of mild steel which is about 1.6 T.

The solenoid lens is only 1.8 cm long and in order to get a sufficiently large focussing power a relatively small inner bore diameter of 7 mm was chosen. The disadvantage of this is that focussing aberrations with the concomitant increase in the transverse normalised emittance start to become noticeable if the rms pulse radius at the lens position exceeds about 200 μm. Since the rms pulse radius would ideally be less than 100 μm in a diffraction experiment, the current lens is expected to work well, and this is confirmed by detailed simulations.

[11] The relationship between the winding temperature T (°C) and winding resistance R (Ω) was found to obey the relation $R = 0.017 \times T + 4.1$ in the temperature range 27 °C ≤ T ≤ 90 °C.

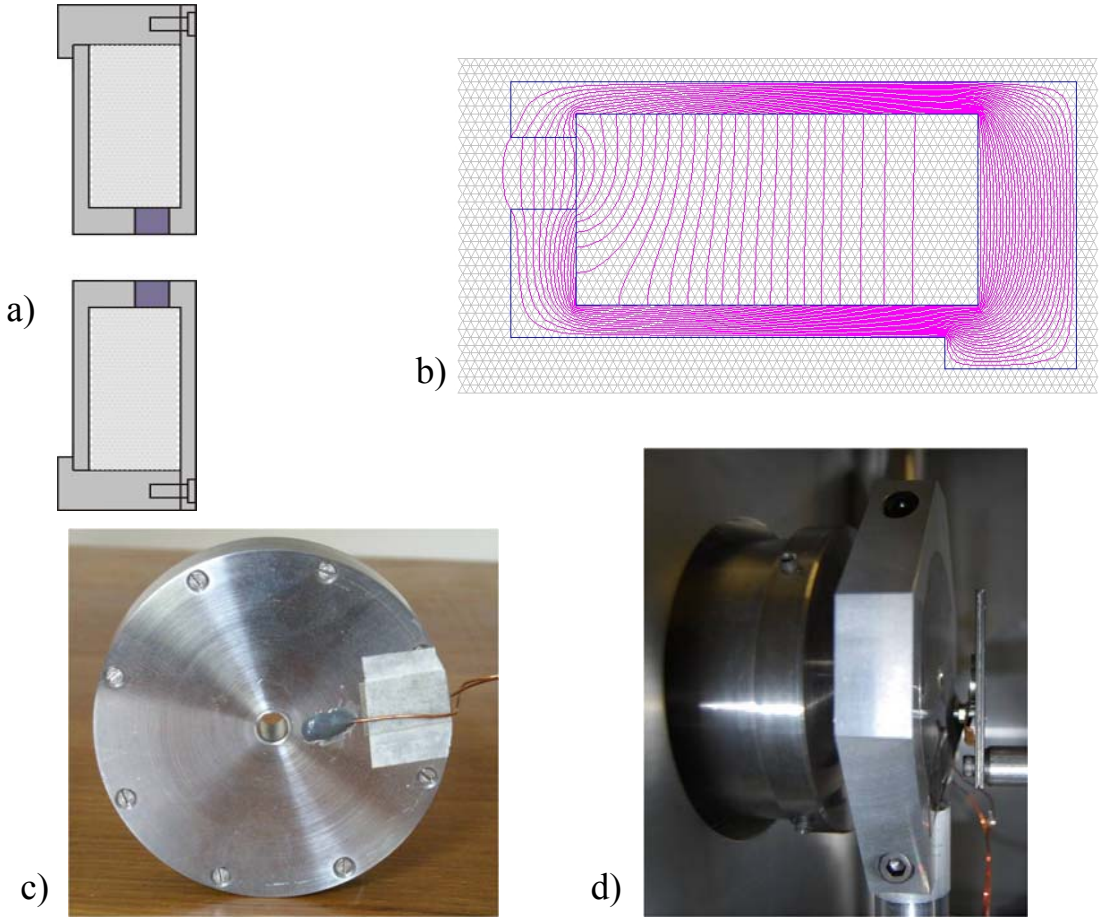

Figure 4.8. Magnetic solenoid lens design and realisation. a) schematic cross section, b) cross section of the geometry with Poisson simulation of the magnetic field lines, c) constructed solenoid lens and d) solenoid lens fitted inside the vacuum chamber with passive cooling bracket.

The on-axis magnetic field profile of the magnetic lens subject to an excitation current of 1.25 A was measured using a small Hall probe, and the result is shown in Figure 4.9[12]. Since the Hall probe was not calibrated, the measured absolute magnetic field values are only known within an error margin of ±10%. The measured peak magnetic field was 125 mT, which is in good agreement with the simulated value of 133 mT. To facilitate easy comparison of the measured and simulated field profiles, the measured magnetic field values were normalised so that the peak measured field coincides with the peak value of the simulated field in Figure 4.9. Clearly the agreement is very good, and therefore one can use the simulated field profile with some confidence in particle simulations of the setup. The absolute magnetic field value can of course currently only be known to within ±10% from knowledge of the excitation current. A

[12] The Hall probe and supplementary instrumentation for this measurement was kindly made available to us by Dirk Fourie at iThemba Labs in Cape Town, South Africa.

more accurate way of estimating the absolute magnetic field of the lens is currently by measurement of the beam divergence as is done in section 4.5.3.

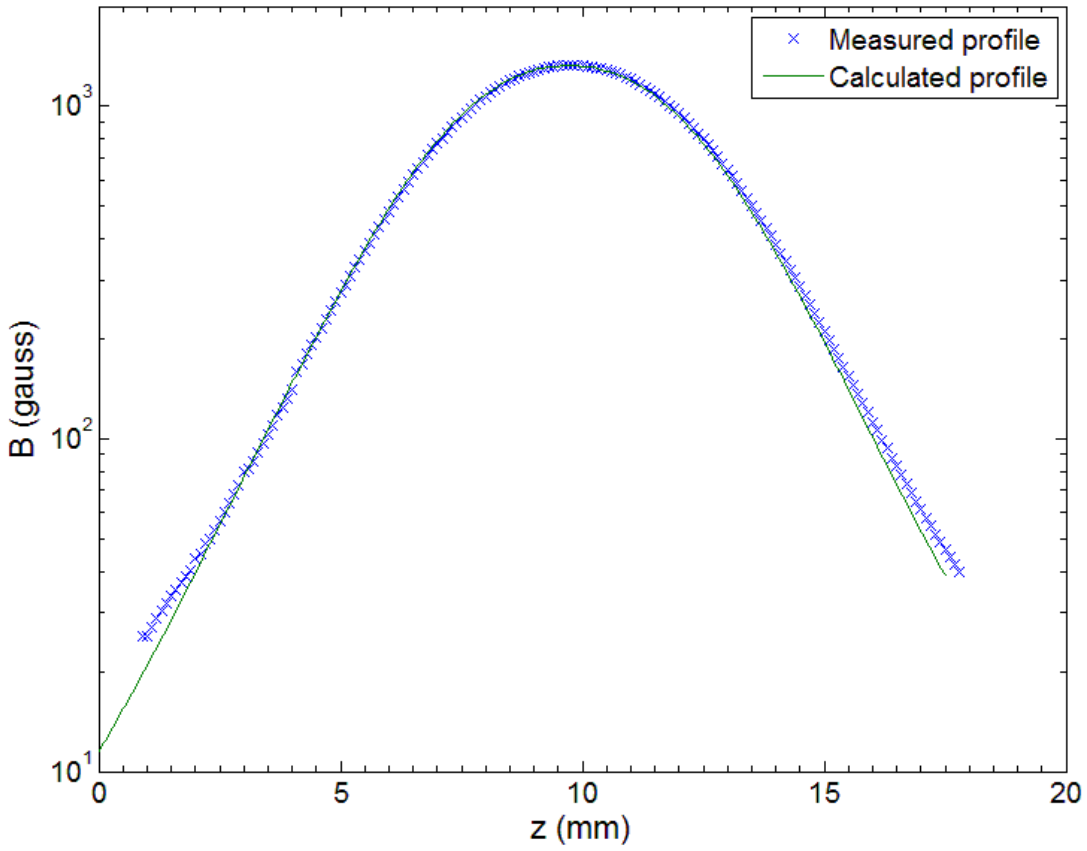

Figure 4.9. Measured and calculated on-axis magnetic field profiles of the solenoid lens using an excitation current of 1.25 A. The Hall sensor was only calibrated to ±10% accuracy. The measured profile was normalised so that its peak magnetic field corresponds to that of the simulated profile; without the normalisation the agreement between the absolute values of measurement and simulation was better than 7%. This plot reveals very good agreement of the measured and calculated profile shapes.

4.4 Electron Detection and Diffraction Images

Due to the problem of space charge induced de-bunching that already becomes significant for electron pulses containing ~10 000 even for short electron guns such as the one implemented in this study, the average beam current is orders of magnitude smaller than in conventional electron diffraction guns. It is therefore imperative to have an electron detection method that approaches the ideal case of single electron sensitivity as closely as possible. Special back-thinned CCD detectors that can be directly illuminated with energetic electrons have come very close to this ideal scenario. The high cost of such detectors and the fact that they may suffer from degradation due to insufficient radiation hardness has thus far rendered their implementation prohibitive for

most groups. At high electron energies exceeding 100 keV, direct illumination of a phosphor screen that is fibre coupled to a cooled high sensitivity CCD is currently an attractive option that also approaches every electron detection capability. At relatively small electron energies of about 30 keV, a multichannel plate (MCP) array is an affordable high sensitivity electron detector, and this is the option chosen for the current project. A 2D MCP is essentially a secondary electron multiplier array that is coupled to a translucent phosphor screen, as illustrated inFigure 4.10 a). To get higher sensitivity, it is common to couple two MCP arrays in tandem in what is known as a Chevron pair, and an electron multiplication factor as high as 10^8 can be achieved. The MCP detector employed in the present setup is of this type, and the detection surface is shown in Figure 4.10 b). The detection area is circular with a diameter of 40 mm, the centre to centre distance of the channels is 15 μm and the channel diameter is 12 μm, yielding a fill factor of 60%. Due to the large electron multiplication factor, it is not necessary to have a particularly efficient optical detection, and a lens coupled system such as the one employed in the present setup (Figure 4.10 c)) is commonly used both in conventional electron diffraction (e.g. RHEED and EBSD) and UED. While MCP detector systems do not achieve every electron sensitivity (typically about 20% of electrons are detected at 30 keV [69]) they are certainly the most affordable option and are viable up to energies of about 60 keV. At larger electron energies, MCP efficiency drops significantly.

The capabilities of the setup were tested by recording a diffraction pattern in transmission from a 50 nm thick free standing titanium foil. The electron energy was set to 37.2 keV corresponding to a de Broglie wavelength of 6.2 pm, and the camera length was 350 mm. After suitable beam focussing, a sharp diffraction pattern was observed, which is shown in Figure 4.11 a). The diffraction pattern consists of concentric rings, which reflects the polycrystalline nature of the specimen. Titanium has a hexagonal crystal system with lattice spacing a = 2.995 Å and c = 4.729 Å [70]. The annular diffraction maxima must satisfy Bragg's law ($2d\sin\theta = \lambda$) where the d-spacing for a hexagonal crystal system is given by [71]

$$\frac{1}{d_{hkl}^2} = \frac{4}{3}\left(\frac{h^2 + hk + k^2}{a^2}\right) + \frac{l^2}{c^2} \tag{4.1}$$

The θ values for the seven most prominent diffraction rings in Figure 4.11 a) were calculated, and compared with peaks predicted by Equation 4.1 substituted into Bragg's law, as shown in Figure 4.11 b). Most of the peaks in the measured radial distribution function match well with low-order values computed from Equation 4.1.

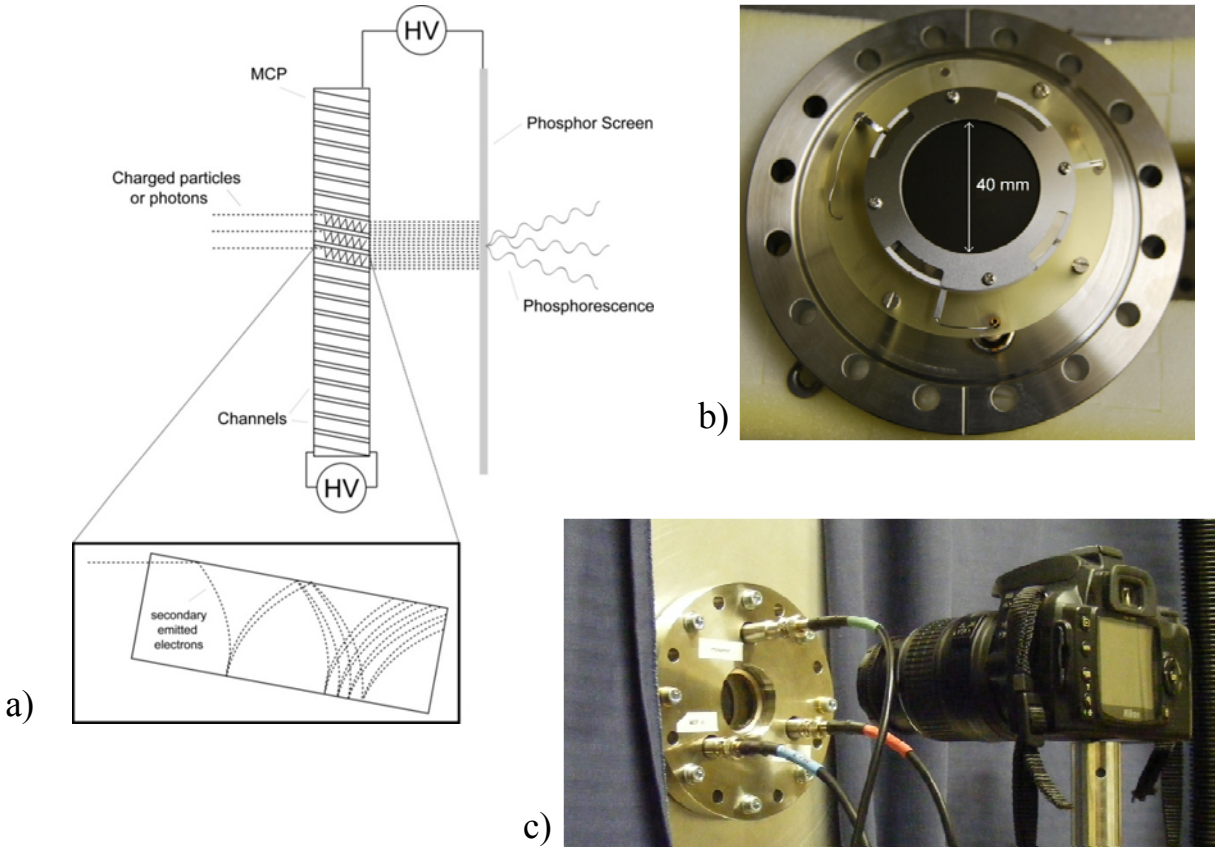

Figure 4.10. The electron detection setup: a) schematic of how a multichannel plate (MCP) array works, b) detection surface of the MCP array fitted in the present setup and c) acquisition of the MCP image with a Nikon camera.

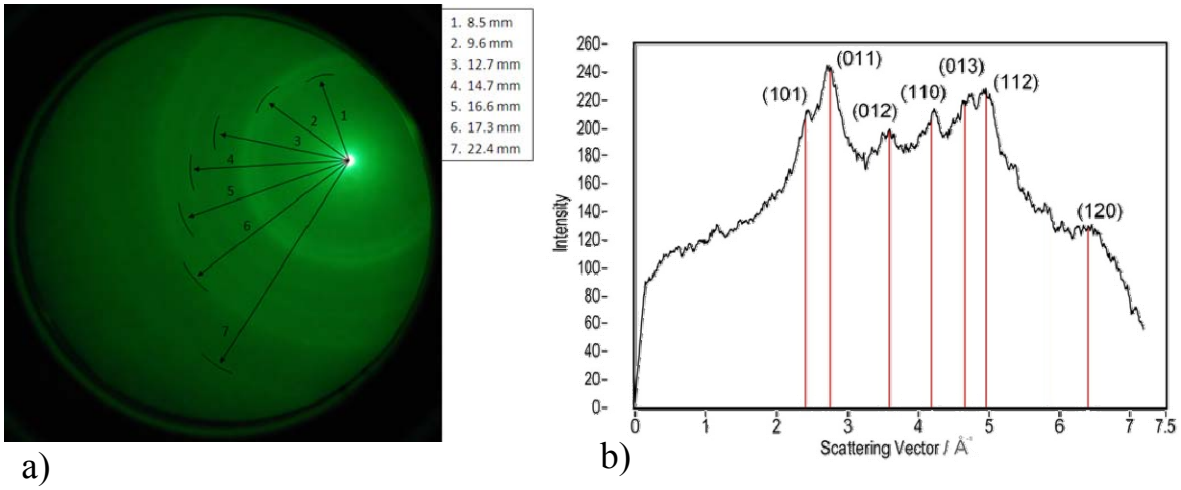

Figure 4.11. Electron diffraction imaging. a) Recorded image of 30 keV electron diffraction rings from a 50 nm free standing titanium foil. b) radial distribution function showing characteristic peaks of titanium calculated from Equation 4.1.

4.5 Measurement of Beam Parameters

4.5.1 Average Beam Current

The electron number per pulse is an important parameter since it is usually the dominant cause of de-bunching in well designed UED guns (see Chapter 3 and Section 5.4). The average bunch charge is most easily measured via the average electron current collected by a Faraday cup (see Figure 4.12 b)) at a known pulse repetition rate (1 kHz in the current setup). For a typical value of 6000 electrons per pulse, the average beam current at 1 kHz is about 1 pA, and measurement with an error of better than 10% therefore demands a current measurement resolution of better than 0.1 pA. While commercial pico-ammeters can easily attain this resolution, such a device was not available for this study. It was therefore decided to use a regular voltmeter (Agilent 34401 A) to measure the potential difference due to the electron current over a large 528 MΩ resistor so that 0.1 pA corresponds to a measurable voltage of about 50 μV(see Figure 4.12 a)). The specified input impedance of the voltmeter is > 10 GΩ, which is much larger than the nominal probe resistance. A smoothing capacitor and good metal shielding of the circuit and connection wires is used to dampen pickup noise. The error of this "electron counting" device is estimated at about ±250 electrons per pulse for a 1 kHz pulse train. The electron number values as a function of incident UV pulse power given in section 4.2 were determined with this setup.

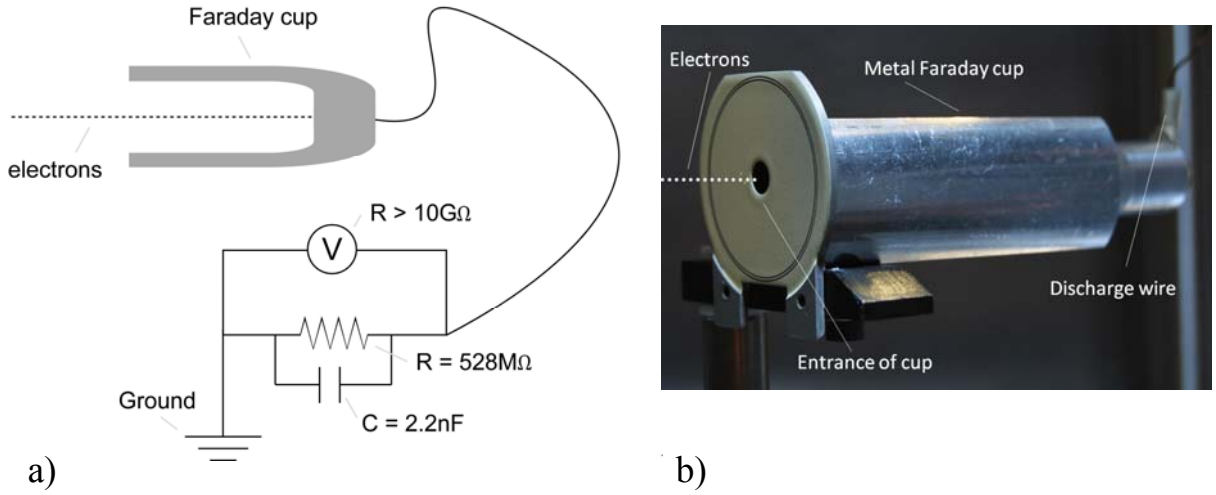

Figure 4.12. Beam current measurement setup. a) The circuit diagram of the beam current measurement device. b) Photograph of the faraday cup used to collect the measured beam. The phosphor screen mounted on the front is used for easy beam location.

4.5.2 Rms Beam Radius

One way of measuring the transverse beam profile is by scanning a suitably sized aperture (50 μm in the present case) along the cross section of the beam and recording the relative intensity of the spot produced on the detector at each position, thus determining the beam profile. While this technique could in principle be used to scan across the beam in two dimensions, thus eliminating the need to assume radial symmetry (the beam may not have complete radial symmetry), this was not done in the present study, and the aperture was scanned over the horizontal beam cross section only. The resulting beam profile at a distance of 5.5 cm from the photocathode is shown in Figure 4.13.

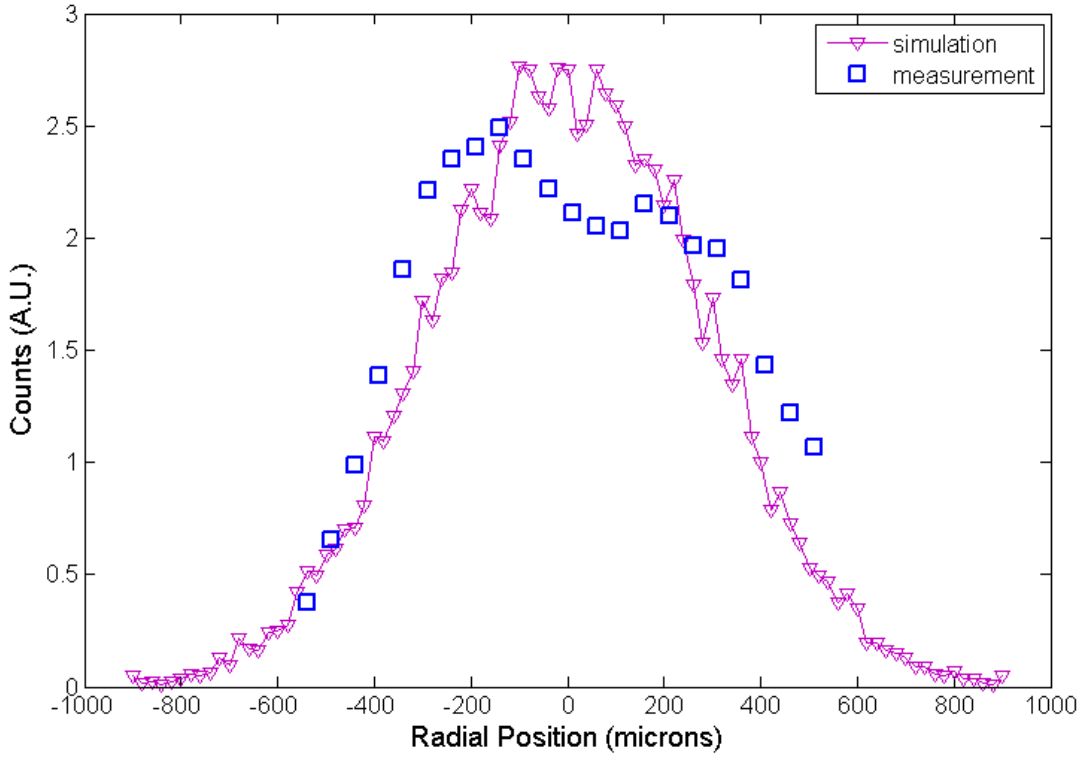

Figure 4.13. Measured and simulated radial beam profile of the electron gun at a distance of 5.5 cm from the photocathode.

The setup was identical to that described in section 3.3. The lens current was set to 0.89 A and the bunch electron number was measured to be 8000 e-/pulse. The simulation parameters (ASTRA simulation) of the calculated radial profile (Figure 4.13) were the same as for the measurement, except that the solenoid field strength in the simulation was varied so as to match the measured rms beam size *and* beam divergence (see Section 4.5.3) as closely as possible. This was done due to the uncertainty in the solenoid magnetic field (see Section 4.3.2) and the fact that the beam divergence is very sensitive to the solenoid field strength. The simulated solenoid current was 0.84 A, deviating from the experimental value by about

6%. As can be seen in Figure 4.13, the simulated profile resembles a Gaussian shape while the measured profile is more irregular, which could have been caused by variations of the electron beam current during the measurement. The rms radii of the measured and simulated beam are 270 μm and 265 μm respectively. This method also yields additional information about the beam, namely the divergence, angular spread and transverse normalised emittance. The latter can be used to compute the energy spread at the photocathode, as demonstrated in the next section.

4.5.3 Divergence , Angular Spread and Emittance

The rms beam divergence $\sigma_{\theta,div}$ is a measure of the collimation state of a beam and is given by

$$\sigma_{\theta,div} = \frac{\langle xx' \rangle}{\sqrt{\langle x^2 \rangle}} = \frac{1}{\sigma_x p_z} \sum_{i=0}^{N} I_i x_i (p_x)_i \; ; \; \sum_{i=0}^{N} I_i = 1 \tag{4.2}$$

where $x' = p_x/p_z$ and I is the normalised intensity corresponding to a given x value.

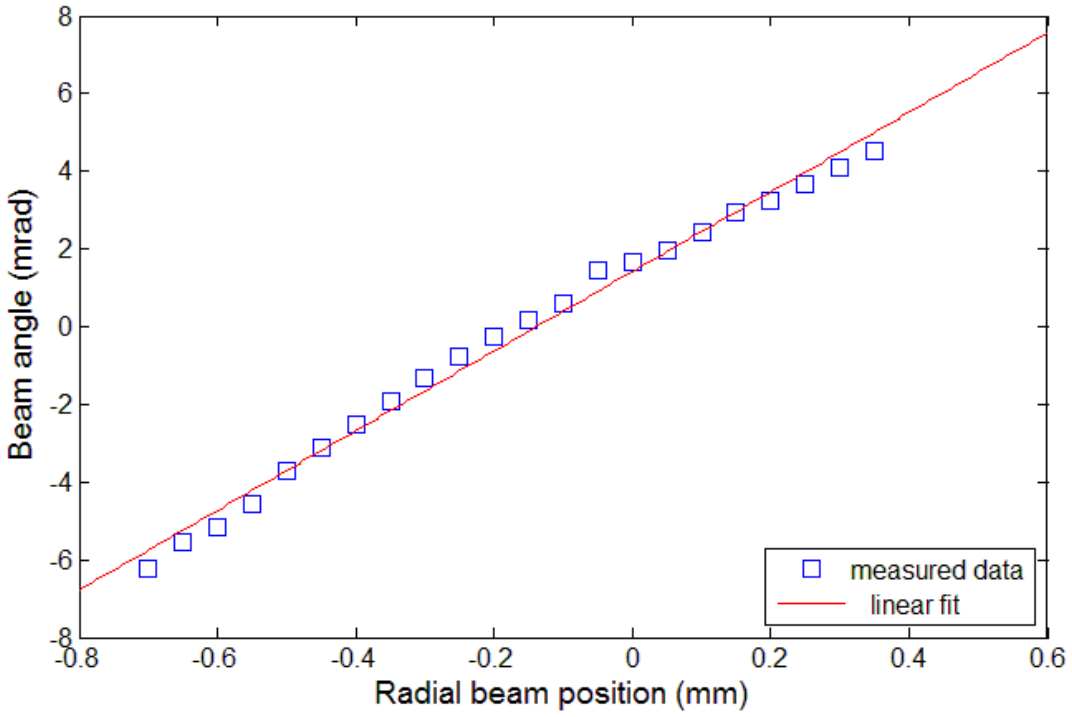

Figure 4.14. Plot of beam angle versus radial position of the electron beam at a distance of 5.5 cm from the photocathode.

The x values are directly known from the radial density measurement in the previous section while the p_x values are deduced from the horizontal position of the observed spot. The resultant angle versus transverse position plot is shown in Figure 4.14. Ideally the plot would

be a straight line, but there is some deviation from linearity here due to lens aberrations of the beam at large radii. For the rms angular divergence the value $\sigma_{\theta,div}$ = 2.7 mrad is found, while the simulated value is 2.4 mrad. The angular divergence is positive, which means that the beam is expanding.

In a diffraction experiment the beam would have a different angular divergence, but this is not important here as the purpose in this section is to estimate the magnetic lens quality and to calculate the energy spread at the photocathode. The initial energy spread of electrons $\Delta E_{ph} = \hbar\omega - \phi_{eff}$ as they are emitted at the photocathode is a useful parameter for estimating the electron gun performance in terms of transverse beam quality. It has not been customary in UED to measure ΔE_{ph}, and researchers usually resort to making a reasonable guess for its value based on literature values such as those of Rangarajan and Bhide [65]. Janzen et al. have however measured the FWHM energy spread at the photocathode using a time of flight technique [38]. Here, the average local (uncorrelated) angular spread $[\sigma_\theta]_l$ of the beam, which is a good measure of its transverse coherence length (see section 2.2.3), is used to calculate ΔE_{ph}. From Equation 2.4 that is valid in the absence of transverse position-momentum correlations, Equation 3.2 can be written in terms of the transverse rms momentum spread:

$$[\sigma_{p,x}]_l = \sqrt{\frac{m(\hbar\omega - \phi_{eff})}{3}} \tag{4.3}$$

$[\sigma_{p,x}]_l$ is computed from an intensity-weighted average of the rms spot sizes r_l obtained from the radial profile measurement described in Section 4.5.2, the latter is given by

$$\langle r_l \rangle = \sqrt{\sum_{i=0}^{N} I_i \, (r_l^2)_i} \; ; \; \sum_{i=0}^{N} I_i = 1 \tag{4.4}$$

with I the normalised intensity of the spots. $[\sigma_{p,x}]_l$ is then related to $\langle r_l \rangle$ by

$$[\sigma_{p,x}]_l = \frac{\gamma m v_z \langle r_l \rangle}{l_c} \tag{4.5}$$

with v_z the electron beam velocity and l_c the camera length (distance from aperture to detector). The r_l values obtained in the measurement are not free of correlated angular spread due to the presence of a rather large rms angular divergence of 2.7 mrad. For the aperture size of 50 μm used in the present experiment, the correlated rms angular spread over the aperture with rms radius 12.5 μm is 0.125 mrad, resulting in an enlargement of the rms spot size of about 50 μm For the present bunch measurement, $\langle r_l \rangle$ = 248 μm from Equation 4.4 and $[\sigma_{p,x}]_l$ = 4.8×10^{-26} kg m/s from Equation 4.5. Assuming conservation of the thermal emittance, the transverse momentum spread at the photocathode is given in terms of the rms bunch radii at

the measured position σ_x and at the photocathode $\sigma_{x,pc}$ by $[\sigma_{p,x}]_{ph} = [\sigma_{p,x}]_l \times \sigma_x/\sigma_{x,pc}$. From Section 4.2 $\sigma_{x,pc}$ is known to be 81 μm. Using Equation 4.3, ΔE_{ph} is found to be equal to 0.55 eV, and the effective work function of the gold layer is thus 4.25 eV.

While bulk gold is known to have a somewhat higher work function of 4.9 – 5.4 eV, thin film layers typically have a work function that is in good agreement with the value obtained here [38,65]. It should be emphasised that the "actual" rms energy spread $\Delta E_k = ([\sigma_{p,z}]_{ph})^2/2m$ and the excess photon energy above the work function ΔE_{ph} generally differ by a large factor since the electrons are emitted in a relatively narrow cone around the surface normal rather than isotropically into half space as shown in Equation 3.1.

5. TEMPORAL CHARACTERISATION WITH A COMPACT STREAK CAMERA

The transverse beam parameters such as angular spread and pulse radius are easily determined using a scanning aperture, but this is not generally the case for longitudinal phase space parameters. In particular, the temporal duration of bunched electron beams requires special measurement techniques. Traditionally, electron pulse durations are measured by passing them through a pair of deflection plates to which a rapidly changing voltage is applied, thereby transforming the longitudinal extent of the pulse into an easily measurable transverse deflection. Such devices, known as streak cameras, are currently not well suited for the temporal characterisation of electron bunches as used in UED for a number of reasons. Section 5.1 gives a brief overview of the current state of the art of UED pulse duration measurements in general and introduces recent developments in streak camera technology in particular. Section 5.2 provides a thorough treatment of streak camera theory with special reference to UED bunch parameters. A novel streak camera design that to a large extent overcomes the challenges faced by current designs is thoroughly introduced in Section 5.3. The experimental results presented in Section 5.4 firmly establish this streak camera concept as a viable contender in the quest for suitable temporal characterisation techniques for UED.

5.1 Electron Pulse Measurement

While the temporal characterisation of laser pulses with femtosecond precision is routine, performing the same feat with electron pulses is considerably more challenging. Improvements on old electron pulse duration measurement techniques as well as proposals and development of new concepts therefore abound. Temporal characterisation of femtosecond optical pulses is done using the technique of cross-correlation; two laser pulses that are well synchronised by deriving them from splitting of a single generating laser pulse are made to interact in a suitable non-linear medium. By recording the interaction observable (e.g. light produced by second harmonic generation) as a function of the relative timing between the pulses, it is in principle possible to resolve features of the pulse with a resolution on the order of the pulse duration. The time difference between the two pulses is typically controlled using a variable time of flight optical delay line, and since an easily controllable distance of 1 μm corresponds to 3 fs time delay, the ability to control the timing is usually not the limiting factor determining the temporal resolution.

There are a number of electron pulse measurement concepts that are based directly or indirectly on the cross-correlation technique. Relativistic electron bunches in large accelerator

facilities can be temporally characterised by electro-optic sampling [72] or generating coherent transition (or diffraction) radiation pulses that can be analysed by standard autocorrelation techniques [73,74,75]. Since such techniques depend on large bunch charge and energy, they are not suitable for sub-relativistic UED. In the sub-relativistic regime, Baum and Zewail have proposed an autocorrelation technique using a pair of co-propagating electron pulses and provided some preliminary results [76]. This method requires detailed modelling of electron bunch propagation, and the experimental setup demands electron pulses that are focussed differently from what would be done in a diffraction experiment, rendering the utility of this technique questionable. A very promising UED pulse characterisation technique is the cross-correlation of electron pulses and laser pulses using ponderomotive force induced scattering, originally proposed by Siwick et al. [77] in response to the shortcomings of streak camera technology at the time. The new technique was demonstrated by Hebeisen et al. using laser pulses with 15 mJ pulse energy, and a temporal resolution of about ±150 fs was achieved [54]. To make the method applicable for more commonly available laser sources with pulse energies in the 100 μJ range, Hebeisen et al. proposed and demonstrated a technique based on ponderomotive scattering of electrons by an optical grating that is synthesised through interference of two counter-propagating fs laser pulses [55]. A temporal resolution of ±160 fs has been achieved. The main contribution to the instrument response time is the transit time of the electron pulse through the laser focus, and sub-100 fs temporal resolution is achievable at higher electron energies and smaller laser spot sizes. The requirement of accurate alignment of two fs laser pulses and one fs electron pulse in space and time, while somewhat challenging, is certainly not prohibitive [55,51].

The oldest and most well established temporal characterisation technique for electron pulses is the streak camera. Since its invention in 1949 [78], the streak camera has seen many applications, such as laser pulse duration measurements [79], electron beam based analog to digital conversion [80] and temporal measurement of electron and x-ray pulses [17,53,45,81,82]. Traditionally, the resolution limit of x-ray streak cameras is considered to be in the ps range due to the photoelectron energy spread and space charge induced broadening as well as timing jitter in the photo switching process [81,82,83]. In UED, one is of course interested precisely in the duration of the electron pulse, and therefore jitter in the photo switching has been a major obstacle, with single shot designs as the most common solution to this problem [17,53,45]. Even in the absence of shot to shot jitter, traditional streak cameras suffer from too small a streak velocity for true fs temporal resolution [17,53,45]. In the last decade, developers of X-ray streak cameras have made much progress in the quest for low-jitter streak cameras suitable for running in accumulation mode [81,84,85,86,87,88]. This

progress has mainly been due to a decrease in the streak camera size (smaller electron transit time) [87], a decrease in the photo switching jitter by using special switch configurations [86], careful optimisation of the laser intensity [88] or trigger laser pulse cleaning [84]. These results are strong support for the feasibility of "jitter free" streak cameras.

5.2 Streak Camera Theory

5.2.1 Basic Principles

Streak camera measurements can be regarded as a type of cross correlation of an electron pulse and a radio frequency (RF) quasi-transverse electromagnetic (TEM) wave guided by a pair of streaking plates. The term streak camera frequently refers to a setup comprising a photogun, streak plate assembly and detector. In the context of UED, the photogun is excluded from this list, since it is precisely the performance of the latter that is of interest here.

The basic principle on which a streak camera operates is illustrated in Figure 5.1. A time dependent voltage $V(t)$ produces a transient electric field $E(t)$ between a pair of streak plates of width l_s and separation d. The following assumptions are made for the electric field: 1) $E(t)$ is abruptly terminated at the streak plate edges and 2) $E(t)$ is independent on the z-coordinate inside the streak region. Condition 2) implies that $E(t)$ must be associated either with a standing electromagnetic (EM) wave or an EM plane wave propagating perpendicularly to the electron beam direction. Travelling wave deflectors where the EM wave has co-propagating components with the electron beam are therefore excluded from the discussion below. As shown in Figure 5.1, two particles labelled *electron 1* and *2* respectively are incident upon the streak plates with longitudinal (z-direction) momentum p_z. Since the electrons begin their transit through the streak region at different times (t_1 and t_2), they experience a different transverse electric field $E(t)$ which imparts transverse momenta p_{y1} and p_{y2} respectively. These transverse momenta are given by

$$p_{y1} = e\int_{t1}^{t1+T} E(\tau)d\tau\,;\; p_{y2} = e\int_{t1+\Delta t}^{t1+\Delta t+T} E(\tau)d\tau \tag{5.1}$$

where e is the elementary charge, T the transit time through the streaking field and $\Delta t = t_2 - t_1$.

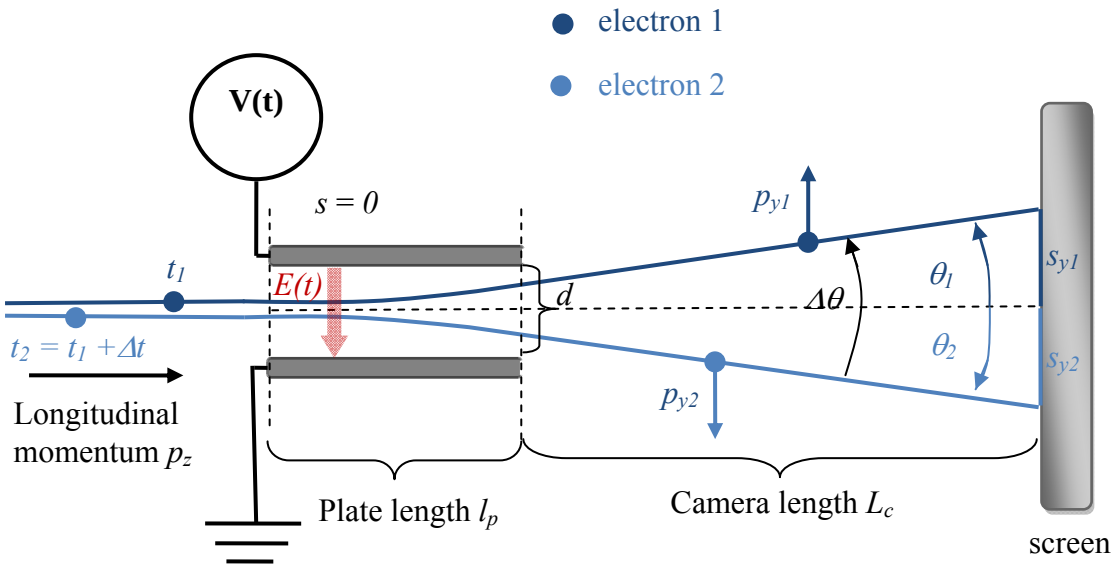

Figure 5.1. Illustrated principle of streak camera operation. Electron 1 and electron 2 are deflected by angles θ_1 and θ_2 respectively, resulting in a total angular spread $\Delta\theta = \theta_1 - \theta_2$ that is proportional to the temporal separation Δt of the two electrons.

It has been customary in the UED literature to make the a priori assumption of a linear electric field ramp in order to explicitly evaluate the integrals in Equation 5.1 (apart from the fact that the field ramp in these cases may indeed have been linear) [45,89]. A more generally applicable and as it turns out simpler approach that does not require such a strong assumption on the form of $E(t)$ is adopted here. One evaluates the momentum difference Δp_y as

$$\Delta p_y = p_{y1} - p_{y2} = e\left[\int_{t1}^{t1+T} E(\tau)d\tau - \int_{t1+\Delta t}^{t1+\Delta t+T} E(\tau)d\tau\right] \tag{5.2}$$

which from elementary calculus is easily shown to be equivalent to

$$\Delta p_y = e\left[\int_{t1}^{t1+\Delta t} E(\tau)d\tau - \int_{t1+T}^{t1+\Delta t+T} E(\tau)d\tau\right] \tag{5.3}$$

From the equation above it follows that the streak momentum difference between two electrons separated by a time difference Δt depends *only* on the behaviour of $E(t)$ within two time intervals of width Δt starting at t_1 and t_1+T respectively. Moreover, if the streak field varies slowly over timescales comparable to Δt [13], $E(t)$ may be regarded as constant in the integrals of Equation 5.3, so that the following simple relation holds:

$$\Delta p_y = e(E(t_1) - E(t_1 + T))\Delta t = e\Delta E\Delta t \tag{5.4}$$

where $\Delta E = E(t_1)$-$E(t_1+T)$. Subject to the assumptions that led to equation 5.4, the streak momentum difference is therefore independent on the temporal shape of $E(t)$, depending only

[13] In 51section 5.3 it will be seen that this is indeed the case even for compact high frequency streak cameras.

on the discrete values $E(t)$ assumes at the time the electron pulse enters and exits the transient field respectively. The corresponding streak angle $\Delta\theta$ which determines the streak length observed on the screen is given by $\Delta\theta = \Delta p_y/p_z$ with $p_z = \gamma m v_z$ and γ, m and v_z are the Lorentz factor, the electron rest mass and the longitudinal electron velocity respectively. Thus one has

$$\Delta\theta = \frac{e\Delta E}{\gamma m v_z}\Delta t \equiv \omega_s \Delta t \tag{5.5}$$

where the angular streak velocity ω_s is a useful figure of merit for estimating the temporal resolution $\Delta\tau_e$ associated with the data extraction. For the case where the electron spot size on the screen is smaller than the pixel size, the temporal resolution is given in terms of $\Delta\theta_{min}$, the smallest angle that can be resolved by the detector, which can be calculated as the ratio of the distance between detector pixels d_p and the camera length l_c. For such a case, the streak velocity $v_s = l_c\omega_s$ is a useful quantity in estimating the temporal resolution. Usually, however, it is the electron spot size on the detector that limits the obtainable resolution rather than the pixel size. It turns out that the smallest resolvable streak width is in this case roughly equal to the rms width of the electron spot on the detector. The estimated error for the pulse duration extraction $\Delta\tau_e$ is thus given in terms of the local rms angular spread σ_θ by

$$\Delta\tau_e \cong \frac{\gamma m v_z \sigma_\theta}{e\Delta E} = \frac{\sigma_\theta}{\omega_s} \tag{5.6}$$

To maximise the streak angle, and therefore get the best possible temporal resolution, it is clear from Equation 5.6 that ΔE must be as large as possible. In fact, ΔE is the only *instrument-specific* parameter that can be optimised; all other quantities in Equation 5.6 pertain to the electron pulse, which are obviously immutable in a given experiment. Equation 5.6 shows that high quality beams with a large transverse coherence length (which is desirable for diffraction experiments) can be temporally characterised with particularly good resolution.

At this stage it is appropriate to point out an important feature of the streak field: the deflection angle of an electron at the centre of the pulse to be measured should be zero. In terms of Figure 5.1 this means that an electron arriving at time t_1+1/2Δt should have a zero deflection angle. One reason for this is to minimise dispersion due to the finite rms energy spread of the electron pulse. The resultant energy dependent streaking cannot be separated from the time dependant streaking, and would thus limit the temporal resolution. In addition, this measure minimises the dependence of the streak angle on amplitude jitter in the supply voltage, see Section 5.3.3.

The remaining task in this section is to discuss and quantify the factors influencing ΔE, and to determine limitations on ΔE as a function of these factors. Maximising ΔE means maximising the difference between the electric field values as the (short) electron pulse enters

and exits the streak region respectively. For a harmonic transient, the electric field is given by $E(t) = E_0\cos(2\pi t/T_\omega)$ where T_ω is the period of the oscillation. In terms of the transit time T, and incorporating the zero net deflection condition, ΔE is given by

$$\Delta E = E_0\left[\cos\left(\frac{\pi}{2}\left(1-\frac{T}{T_\omega}\right)\right)-\cos\left(\frac{\pi}{2}\left(1+\frac{T}{T_\omega}\right)\right)\right] \tag{5.7}$$

The maximum possible electric field difference is then $\Delta E_{max} = 2E_0$, which occurs for $T_{max} = \frac{1}{2}T_\omega$, i.e. the optimal choice for the transit time is half the oscillation period of the streak field. This optimal scenario for which the streak angle is a maximum for a given electric field amplitude E_0 is depicted in Figure 5.2.

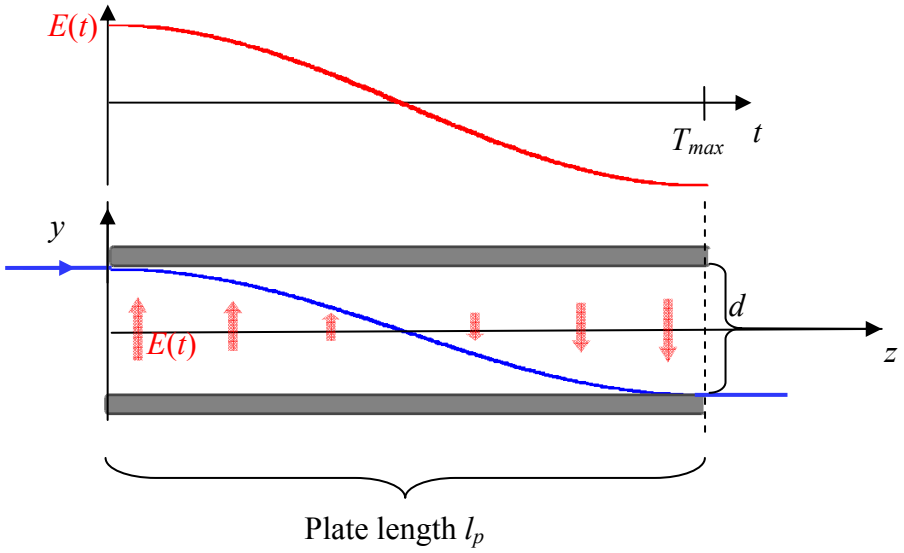

Figure 5.2. Illustration of the deflection of an electron beam inside the streak plates. The transient harmonic electric field $E(t)$ leads to an electron beam deflection which can at most be equal to the plate separation d for the maximal (half cycle) transit time T_{max}.

As seen in the figure, the electron beam undergoes a deflection inside the streak region. To prevent clipping, this deflection must be less than the plate separation d. Assuming nonrelativistic transverse velocities, the equation of motion in the transverse (y) direction is given by

$$y(t) = \frac{eE_0T_\omega^2}{4\pi^2\gamma m}\cos\left(2\pi\frac{t}{T_\omega}\right) \tag{5.8}$$

Setting $\Delta y = y(0) - y(\frac{1}{2}T_\omega)$, $T_\omega = 2l_p/v_z$ and $p_z = \gamma m v_z$, this is leading to

$$\Delta y = \frac{2el_p^2E_0}{\pi^2 p_z v_z} \tag{5.9}$$

An application of these ideas is now demonstrated by an example: suppose a 30 keV electron pulse is to be measured with a streak camera with an available voltage of 1500 V such that a 100 fs temporal difference corresponds to a streak angle of 0.5 mrad. What is a suitable streak plate length that can be used? To answer this question, one first calculates $E_0 = \frac{1}{2}\Delta E$ using equation 7.5 with $v_z = 1.0\times10^8$ m/s and approximating $\gamma = 1$ for 30 keV electrons, which yields $E_0 = 1.4\times10^6$ V/m. Thus, $d = 1.1$ mm. Demanding that $\Delta y = 0.2\times d$ to prevent aberrations one obtains, via equation 5.9, $l_p = 6.3$ mm. The required oscillation frequency is then f = 7.9 GHz. In Section 5.3.15.2, additional compelling motivations will be given for the use of short streak lengths and high frequencies.

5.2.2 Streak Pattern Analysis

It was mentioned in Section 5.2.1 that the temporal resolution associated with the streak pattern analysis does not only depend on the spatial resolution obtainable with a given detector. From a purely data analysis point of view (excluding any other sources of error) there are in fact limitations on the accuracy with which the streak angle can be extracted; these limitations are due to the finite angular spread of the un-streaked pulse which results in a finite spot size on the detector that is independent on the streak angle and necessitates careful de-convolution of the data. In this section a rigorous streak angle extraction method that is both physically and mathematically plausible and requires no a priori assumptions on the temporal electron pulse profile (other than general physically reasonable assumptions) is described. Limitations on the resolution of extracted data are also discussed.

Consider a cylindrical slice taken from an ultrashort electron pulse as shown in Figure 5.3. Such a cylinder is obtainable in practise by truncating the electron pulse with a suitable aperture placed in front of the streak plates. Suppose further that the electron pulse is focussed spatially onto the detector such that the spot size depends only on the local random angular spread, and that the aperture is sufficiently small to render radial space charge broadening insignificant. The un-streaked image is then a circular spot with rms radius $r_{rms} = \sigma_\theta \times l_c$. Reasonably assuming that the rms angular spread σ_θ does not depend on the longitudinal coordinate in the pulse, it becomes clear from the figure that the streaked image can be interpreted as an overlap or convolution of copies of the un-streaked profile which are shifted relative to each other along the streak direction. The shift is related to the arrival time of temporal segments in the cylindrical pulse via the streak velocity. Let the streak direction be along the y-axis as shown in Figure 5.3. To convert the streak image to a 1D function one can bin the counts of detector pixels along the x-axis perpendicular to the streak direction.

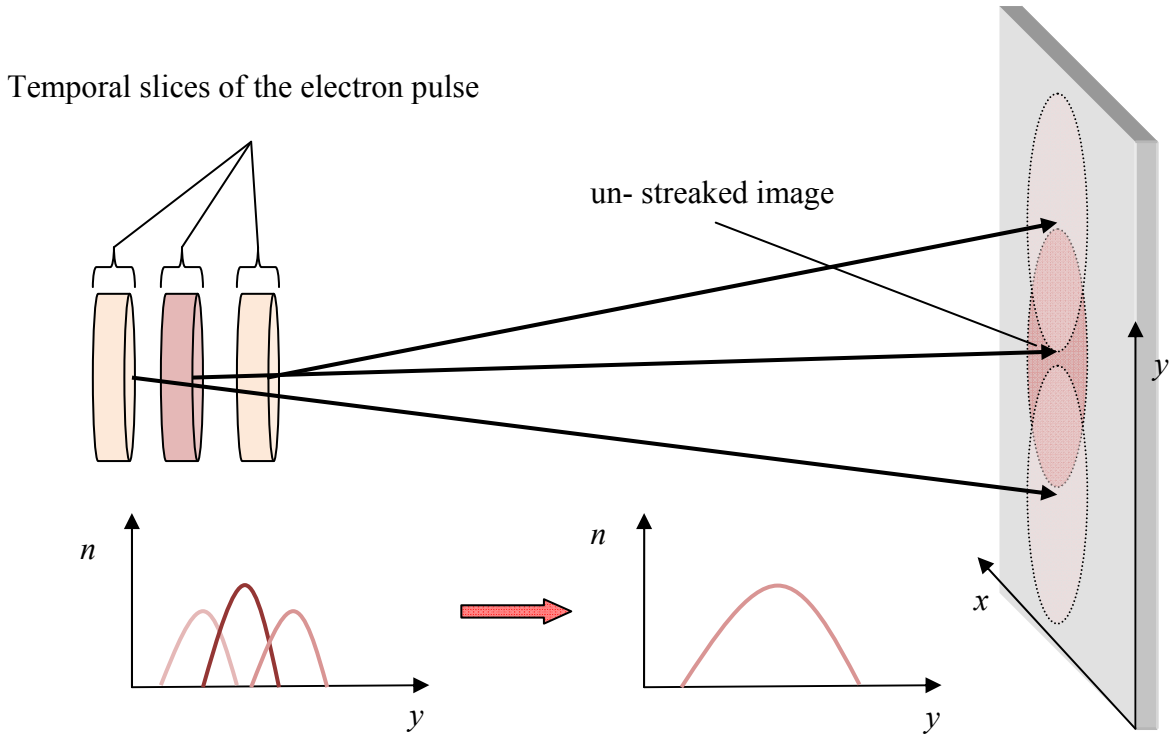

Figure 5.3. Illustration of the formation of a streak image. Different temporal slices of the pulse form a pattern of partially overlapping spots. The pattern can be de-convoluted to yield the temporal electron density profile of the pulse.

The resulting streaked image profile $s(y)$ is then given by the convolution of the un-streaked profile $u(y)$ and the streaked density profile $d(y)$:

$$s(y) = \int_{-\infty}^{\infty} d(y - y')u(y')dy' \tag{5.10}$$

Since $y = t \times v_s$ where v_s is the streak velocity, $d(y)$ is linearly related to the temporal electron density profile of the pulse. To extract $d(y)$ from the experimentally measured $s(y)$ and $u(y)$ profiles, equation 5.10 must be discretised, yielding the following matrix equation

$$\mathbf{s} = A\mathbf{d} \tag{5.11}$$

with **s** and **d** vectors representing $s(y)$ and $d(y)$ respectively. The matrix A is given by

$$A = \begin{bmatrix} u_1 & 0 & \dots & 0 \\ u_2 & u_1 & \dots & 0 \\ \vdots & u_2 & \dots & \vdots \\ u_n & \vdots & \dots & 0 \\ 0 & u_n & \dots & u_1 \\ \vdots & 0 & \dots & u_2 \\ 0 & \vdots & \dots & \vdots \\ 0 & 0 & \dots & u_n \end{bmatrix} \tag{5.12}$$

with u_i the entries of **u**, the vector representing the function $u(y)$. All the columns of A therefore consist of the same vector **u** that is shifted downward by one row per column

increment, and augmented with an appropriate number of zeros. In principle, Equation 5.11 can be solved for **d** by using linear least squares methods. In practise, this approach will not usually yield a physically meaningful solution. The reason for this is that the matrix A is *ill-conditioned*. In A, any two adjacent column vectors are near-parallel, causing the solution **d** in Equation 5.11 to be very sensitive to fluctuations (noise) in the experimentally determined A and **s**. As a result, there is a wide spectrum of vastly different solutions **d** that are consistent with Equation 5.11 in the least squares sense.

To get a stable and physically meaningful solution, additional information needs to be added, and this is done in the form of constraints. An obvious yet powerful constraint is non-negativity of **d**: a negative electron density is unphysical and can be rejected immediately. This is in distinction to the case of waves, for example, where destructive interference does indeed occur. It is further necessary to impose continuity (smoothness) constraints on the solution[14]. Instead of minimising $||A\mathbf{d} - \mathbf{s}||^2$, one solves the following optimisation problem:

$$\min_{\mathbf{d}_\alpha \geq 0} \left\{ \frac{1}{2} \|A\mathbf{d}_\alpha - \mathbf{s}\|^2 + \frac{\alpha}{2} \|\mathbf{d}_\alpha\|^2 \right\}, \qquad \alpha > 0 \tag{5.13}$$

The term involving the regularisation parameter α favours solutions $\mathbf{d}_\alpha$ with a small norm, which generally have greater degree of continuity. This method is known as Tikhonov regularisation [90], and α is chosen such that $||A\mathbf{d}_\alpha - \mathbf{s}|| = \delta$, where δ is the expected rms error in the experimental data **u** and **s**. In order to solve for $\mathbf{d}_\alpha$, Equation 5.13 can be written as a quadratic programming problem in standard form [91]:

$$\min_{\mathbf{d}_\alpha \geq 0} \left\{ \frac{1}{2} \mathbf{d}_\alpha^t (A^t A + \alpha I) \mathbf{d}_\alpha - \mathbf{d}_\alpha^t A^t \mathbf{s} \right\}, \qquad \alpha > 0 \tag{5.14}$$

Here, I is the identity matrix and the superscripted t denotes the transpose of the relevant vector or matrix. Equation 5.14 can be solved by techniques such as the interior point or active set methods. The technique discussed here is implemented in the results section (Section 5.4.) to find pulse durations and temporal pulse profiles.

An important question is with what precision the temporal duration of the pulse can be extracted from the streak image given the measured profiles and the angular streak rate. The simplest and most reliable method of estimating this error is to de-convolute the un-streaked profile with itself, i.e. using a kernel matrix A consisting of column vectors of the un-streaked profile to extract the width of the un-streaked profile itself subject to suitable regularisation conditions. The temporal width of the trace thus generated is a good estimate of the temporal de-convolution error $\Delta\tau_e$. It turns out that this method yields a FWHM error width

[14] Statistical fluctuations that may lead to a discontinuous electron density profile for a single electron pulse are smoothed out if the data represents an average of sufficiently many shots. Demanding continuity for a streak measurement done in accumulation mode is therefore well justified.

corresponding roughly to the rms angular spread of the un-streaked pulse, as already mentioned in Section 5.2.1.

5.3 Design and Construction of a Compact Streak Camera

5.3.1 Design Choices and Goals

In Section 5.2.1 it was briefly mentioned that streak cameras can be classified according to whether the streak plates employ standing waves or travelling waves respectively. The discussion was limited to the former due to the relative simplicity of the required design. A further classification of streak cameras can be made according to the mode of operation: single shot or accumulation mode. In the context of UED, the single shot mode has thus far yielded the highest temporal resolution [45]. While single shot measurements are insensitive to photo-switch timing jitter, they suffer from the major disadvantage that the streak image comprises only a small number of data points[15], leading to statistical problems in the data interpretation. Even if the electron number per shot is large, attenuation may be required to limit radial pulse broadening due to space charge forces which would compromise the resolution at the detector. Moreover, there is no way of measuring the shot to shot arrival time jitter of the electron pulses themselves in case of single-shot measurements, and one cannot characterise an entire pulse by sampling the longitudinal profile at different radial positions.

For purposes of this study, it has therefore been decided to design and construct a streak camera in accumulation mode. The major challenge with accumulation mode streaking is of course minimising the switching jitter, but there are many reports of the achievement of sub-100 fs switching jitter, see Section 5.1.

Another major problem associated with streak cameras in the context of UED is the finite length of the streak region; ultrashort electron pulses, particularly highly charged ones, expand rapidly as a function of propagation distance (see Section 3.1.3), and to avoid temporal smearing associated with pulse expansion inside the streak region, a very small streak length is required, on the order of a few mm for 30 keV electrons with electron numbers in the 10^4 range. In accordance with the discussion in Section 5.2.1, the transit time of the electron pulse through the streak region must be comparable to the half period of the streak field. Short streak lengths therefore imply high frequencies, requiring a very compact design that minimises inductance, capacitance and resistance of the oscillating circuit. As will

[15] Even in the ideal case of single- electron detection, the image will typically be composed of only a few hundred to a few thousand points.

be discussed in Section 5.3.3, high oscillation frequencies have the additional benefit of reducing the switching jitter of the streak camera, see also [87]. The streak field strength, and consequently the applied voltage, should be maximised in order to have a sufficiently large streak angle. The plate separation should be as small as possible to maximise the streak field, and fortunately this is facilitated by a compact design, as discussed in Section 5.2.1. Another concern is radial space charge induced broadening of the streaked beam between the streak plates and detector. This can be remedied by using an aperture in front of the streak camera to limit the number of electrons per shot. In addition, use of an aperture has the benefit of limiting various distortions, as will be discussed in Section 5.3.3.

In summary, the design choices adopted in this study for a streak camera capable of measuring the temporal duration of 30 keV electron bunches with pulse charge in the 10^4 e^-/ shot range with sub-100 fs precision are as follows:

1) accumulation mode instead of single shot to avoid detection and data analysis problems
2) small streak plate length (a few mm) to minimise temporal smear
3) compact overall geometry to maximise streak field frequency and minimise switching jitter
4) large streak plate voltage and small plate separation to maximise temporal resolution
5) use of an aperture to limit beam distortions and radial space charge broadening

It should be noted that requirements 1 through 5 are not contradictory, but actually complement each other: accumulation mode allows the use of apertures (which reduce the electron number per shot) while apertures and a small streak length allows one to reduce the plate separation and increase the applied voltage, thus increasing the streak angle. The small streak length implies a compact design in any case, and this naturally implies the possibility of higher operating frequencies. The latter facilitates switching jitter reduction. Apart from potential technical difficulties, the design of the proposed streak camera is therefore not problematic.

5.3.2 The Design and its Components

First, the general layout and operation of the streak camera setup will be described, where after a more detailed description of the individual components and their characterisation will ensue. Figure 5.4 a) is a schematic representation of the streak camera experiment, including the optical and electrical circuits involved. The part of the setup involving the electron gun is

the same as described previously in connection with the UED pump-probe setup, and is reproduced here for the sake of completeness. The streak camera itself, including streak plates, electron aperture, photo switch and auxiliary circuitry, is placed in the vacuum chamber. As seen in Figure 5.4 b) ,the streak camera consists of a pair of PC board pieces that are patterned with the streak plate geometry: essentially a 3 × 3 mm^2 square with rounded edges attached to a rectangular 2 × 1.5 mm^2 connecting arm, all fashioned from standard PC board copper. The plates are clamped together via a spacer so that there is a 0.5 mm plate separation. Each connecting arm is attached to the terminals of a photo switch that was custom built by depositing two Germanium-Gold ohmic contacts on a wafer of semi-insulating Gallium Arsenide (GaAs). The electron beam is first truncated by a 50 μm aperture before passing between the plates towards the MCP detector. See Figure 5.4 b) and Figure 5.5 for details of the streak camera geometry.

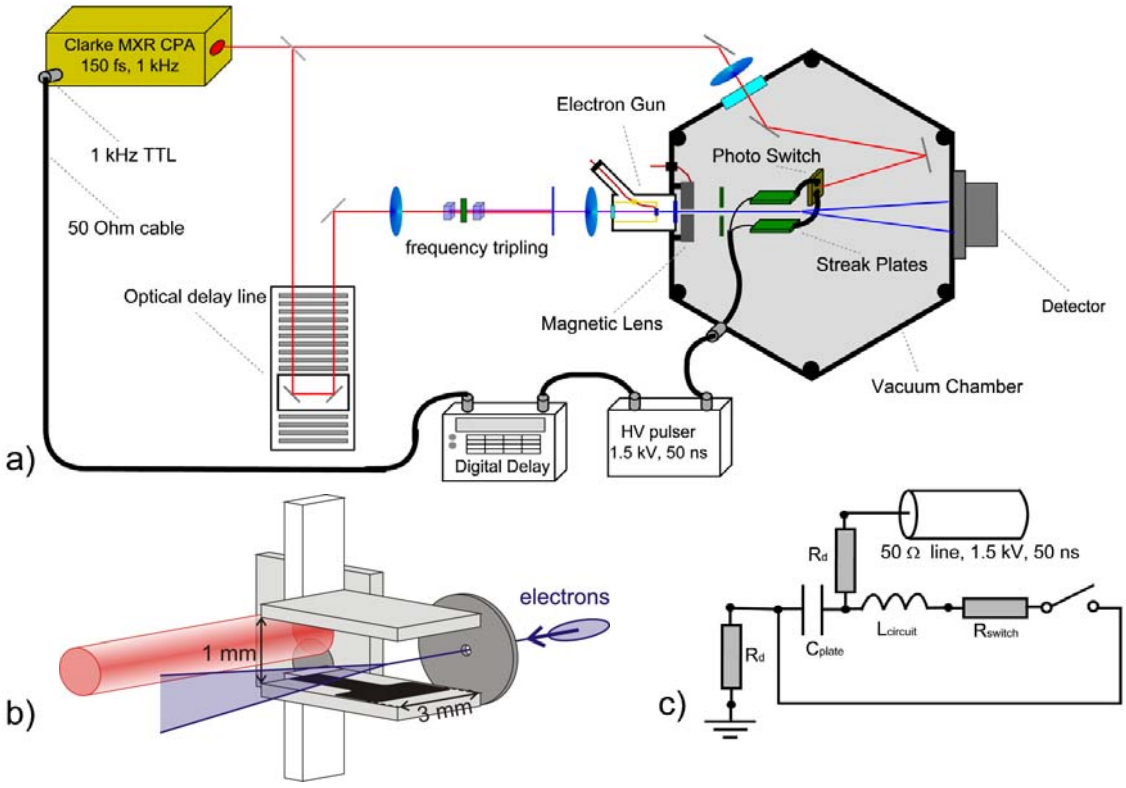

Figure 5.4. Compact streak camera setup and design. a) Schematic of the experimental setup, b) schematic drawing of the streak camera design and c) lumped circuit diagram.

Electrically, the streak camera can be represented as an LCR circuit where the loop inductance L_l and capacitance C_p originate from the discharge loop (including the photo

switch) and the streak plates respectively (see inset in Figure 5.5). The resistance R_s arises mainly from the photo switch. The operation is as follows: with the photo switch in the insulating state, the HV pulser, which was custom built using a Behlke HTS 121 switch, charges the streak plates to a voltage of 1500 V. The high voltage pulse is about 50 ns long, and is synchronised to the 1 kHz fs laser pulse train via a TTL output of the Clarke MXR. The timing, controlled by a Stanford Instruments digital delay generator, is such that the streak plates are fully charged just before the arrival of the pump laser at the photo switch. A pulsed power supply (rather than a DC supply) is necessary since thermal effects in the GaAs switch lead to voltage instability and breakdown already at a few hundred volts. Once the pump pulse impinges on the GaAs switch it becomes conductive, resulting in a well-timed damped oscillation. The timing of the electron pulse (which is of course adjusted using the variable optical delay line) is now such that it traverses the rapidly changing streak field symmetrically about its first zero-crossing; the net deflection of the electron pulse is zero (in accordance with the discussion in Section 5.2.1), but the pulse experiences a streaking effect that is proportional to its temporal duration and can be observed on the detector.

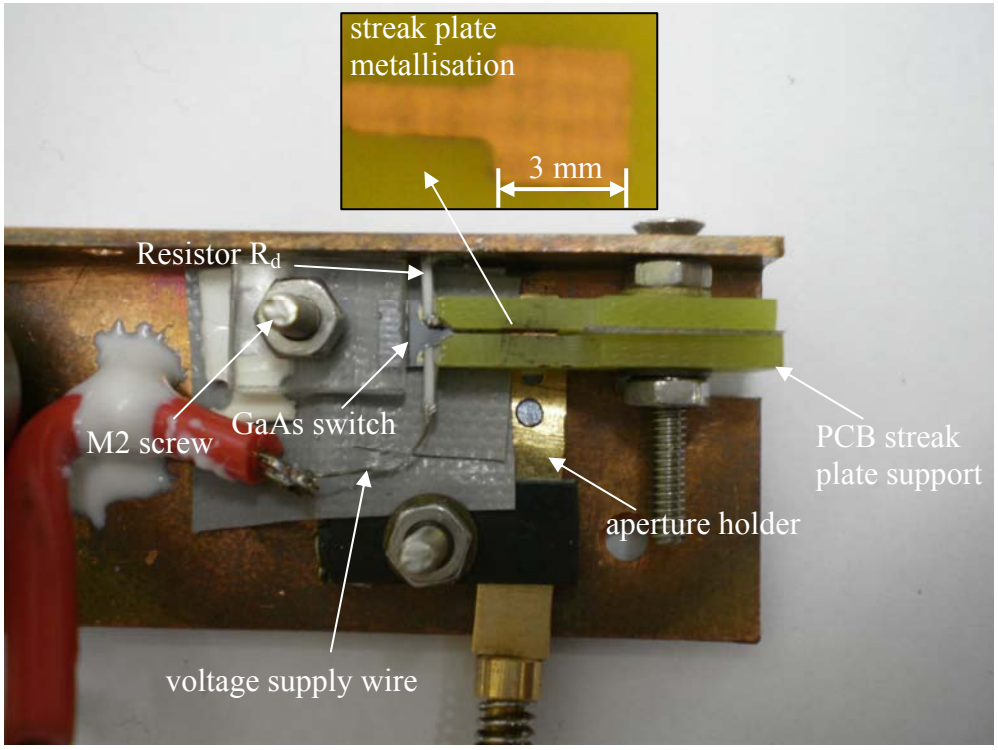

Figure 5.5. Physical implementation of the streak camera.

The two resistors with value R_d in series with the HV pulser and the streak plates serve to de-couple the power supply from the streak plate circuit during the (very short) time of oscillation. Their optimal value depends on a number of factors. Typically, there is output

coupling leakage through the Pockels cell in chirped pulse amplifiers such that, in addition to the main pulse, pre-pulses are also delivered which arrive a few nanoseconds earlier. The intensity ratio between pre-pulses and the main pulse is known as the *pulse contrast*, and is typically on the order of 10^{-2}. This is not small enough to prevent significant discharging of the circuit before the main pulse arrives. However, if the lifetime of the photocarriers τ_s in the switch is short enough (significantly smaller than the time between pre-pulse and main pulse, Δt_p) and R_d is small enough to minimise the charging time constant $2R_dC_p$, the streak circuit will be recharged by the time the main pulse arrives. For this, the condition $2R_dC_p \approx \tau_s \leq 1/3\Delta t_p$ is sufficient. However, R_d should also be large enough so that the time constant $R_dC_p \geq 10t_{1/2}$ with $t_{1/2} = \pi(L_lC_p)^{1/2}$ the half-period of the streak camera oscillation. This is to prevent interference with the high frequency ringing.

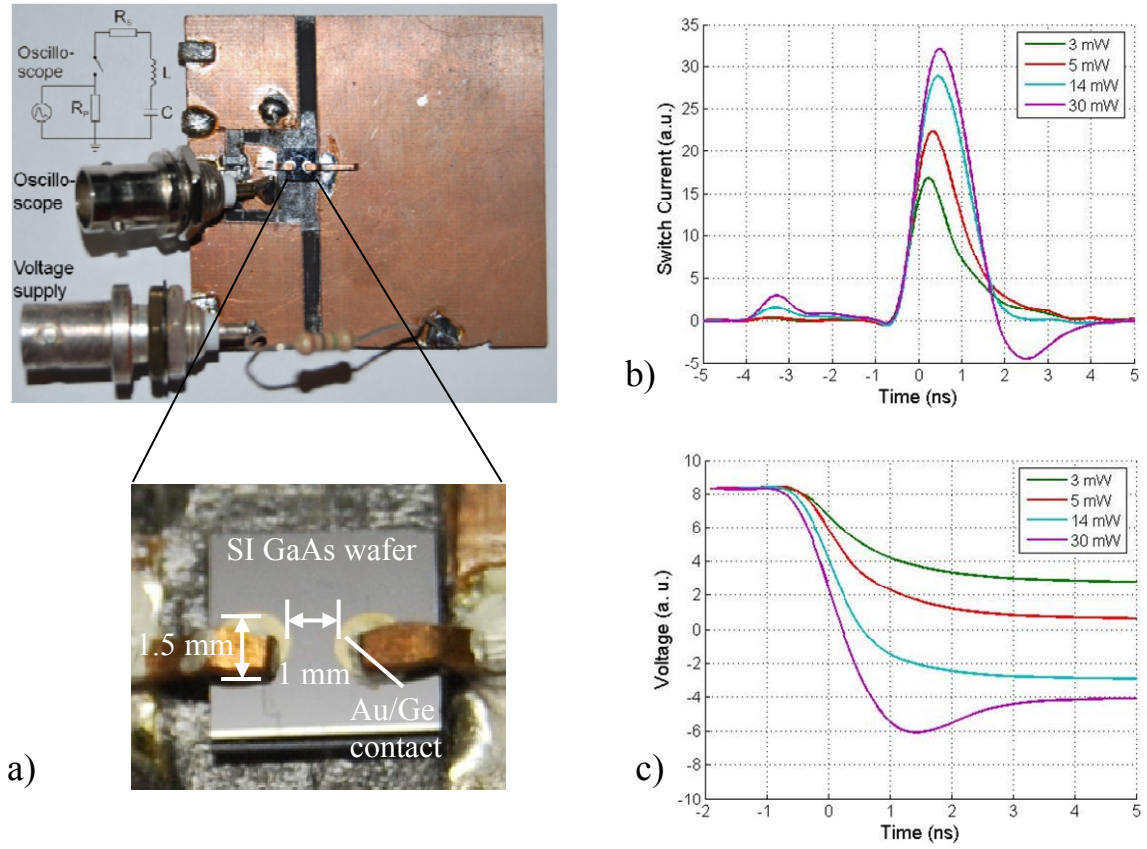

Figure 5.6. Test setup and measurement results for the GaAs photo switch behaviour on the timescale of a few nanoseconds. a) Photograph of the test bed and GaAs photo switch. b) Photocurrent versus time profile of the switch subject to various fs laser illumination intensities. The photocurrent due to laser pre-pulses is clearly visible. c) Temporal profile of the voltage across the photoswitch.

To determine τ_s and Δt_p, a test bed was built, the circuit of which is shown in Figure 5.6 a). A storage capacitor $C \approx 45$pF formed by the pc board metallisation is discharged by the photo switch. The switch current is monitored by measuring the voltage across a 3Ω probe resistor R_p with a 600 MHz oscilloscope. The measurements were done at an initial charging voltage of 80 V and the results for various laser pulse illumination energies in the 3 μJ to 30 μJ range are shown in Figure 5.6 b) and c). In Figure 5.6 b), both the main discharge and a smaller discharge about 4 ns earlier is seen. The latter is due to the pre-pulse, and it only becomes significant at illumination intensities above about 14 mW (corresponding to 14 μJ per pulse), a regime in which the main pulse current begins to saturate. It can also be seen that the current completely vanishes about 5 ns after triggering by the main pulse, suggesting a carrier lifetime significantly less than 5 ns[16]. It should be noted that the complete current decay in Figure 5.6 b) cannot be explained by large switch-independent damping of the circuit since the voltage does not decay to zero, as is evident from the storage capacitor voltage trace (Figure 5.6 c)); the decay must be due to switch-off of the GaAs photo conductor. Thus it should be possible to re-charge the streak plates in the 4 ns time span between pre pulse and main pulse; since the streak plate capacitance is calculated to be about 0.2 pF, a value of about 2 kΩ for R_d, resulting in a time constant of 1 ns, is suitable.

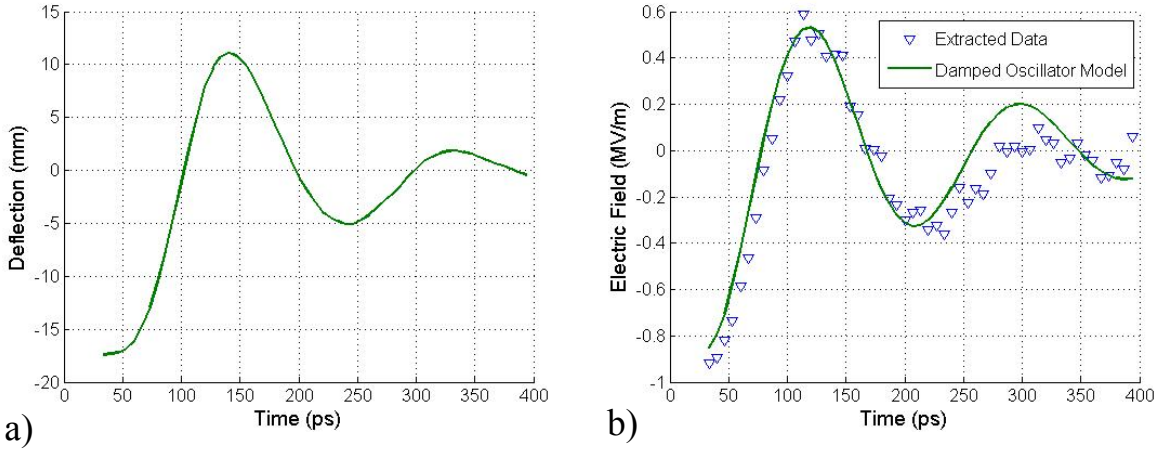

Figure 5.7. Streak field oscillation determined from a pump probe streak experiment. A DC charging voltage of about 400 V was used for these measurements, and the camera length was 35 cm. a) Position of the electron spot on the detector as a function of time delay between 30 μJ switch trigger pulse and electron pulse. b) Electric field of the streak plates versus time calculated from the data in a). The data has been fitted to a simple series LCR oscillator model.

[16] The carrier lifetime is defined as the time taken for the number of carriers to decay to 1/e times the original value.

Measurement of the streak plate oscillation on ps timescales is of course conveniently done using the streak experiment itself. The electron beam deflection as a function of delay time between trigger laser pulse (30 mJ) and electron pulse arrival time is shown in Figure 5.7 a). For this experiment, a static charging voltage of about 400 V was used, and this is about the largest voltage one can use without clipping of the deflected beam on the streak plates or at the detector. The slope of the graph at the first zero crossing determines the streak velocity, which in this case is about 0.5 mm/ps. At the design voltage of 1500 V, a streak velocity of about 2 mm/ps (corresponding to an angular streak velocity of 5 mrad/ps) should thus be achievable, and this was indeed obtained, see Section 5.4.1.

It is instructive to compute the streak field as a function of time in order to estimate circuit parameters such as the effective inductance and switch resistance. This allows one to estimate the expected switching jitter caused by laser intensity fluctuations, as shown in Section 5.3.3. Assume that the streak field is triggered at $t = 0$. The value of the constant streak field for $t \leq 0$, $E(t \leq 0)$, is given in terms of the initial deflection length s_0, camera length l_c, streak plate width l_s and electron bunch velocity v_z by

$$E(t \leq 0) = \frac{\gamma m v_z^2 s_0}{e l_c l_s} \tag{5.15}$$

Differentiating both sides of the first Equation 5.1 with respect to τ and using the fact that $s/l_c = p_y/p_z$, one obtains the following recursion relation on $E(t)$

$$E(t) = E(t - T) - \frac{\gamma m v_z}{e l_c} s'(t) \tag{5.16}$$

where $s'(t) = \mathrm{d}s(t)/\mathrm{d}t$. Equation 5.16 can then be solved using the data shown in Figure 5.7 a) and the initial condition given by equation 5.15 in terms of the measured initial deflection s_0. The result of this computation is shown in Figure 5.7 b), and the data was fitted to a simple series LCR oscillator model given by

$$E(t) = E_0 \exp\left(\frac{-R_s}{2L_l} t\right) \cos(\omega' t) \; ; \; \omega' = \sqrt{\left(\frac{1}{L_l C_p}\right)^2 - \left(\frac{R_s}{2L_l}\right)^2} \tag{5.17}$$

The plate capacitance C_p was not used as a fitting parameter but calculated from the geometry as $C_p = 0.2$ pF (this includes an estimate for the stray capacitance of the photo switch itself). The fit shown in Figure 5.7 b) then yielded $L_l = 5$ nH and $R_s = 50\ \Omega$. The extracted oscillation frequency is 5.2 GHz. Before presenting and discussing the electron pulse measurements, it is useful to discuss possible sources of error associated with the streak camera under consideration, thereby getting an idea of the temporal resolution that can be expected.

5.3.3 Sources of Error

There are several factors that can cause streaking of the electron pulse other than its temporal duration. These can be grouped into effects due to 1) the streak plate geometry/ alignment, 2) properties of the streaking electron pulse including its momentum spread and space charge forces, and 3) jitter in the streak field, which includes factors due to fluctuations in the charging voltage and the photo switching process.

The entry angle of the electron pulse at the streak plates is optimally 90º. Deviations $\Delta\theta$ from this ideal case result in streak smearing due to the finite transverse size of the electron pulse, as explained in Figure 5.8 a). The resulting error in the temporal resolution is

$$\Delta\tau_\theta = \frac{d_a \sin\,\Delta\theta}{v_z} \tag{5.18}$$

where d_a is the aperture diameter, which is 50 µm in the present case. Assuming a value of 6º for $\Delta\theta$, $\Delta\tau_\theta$ is evaluated as 50 fs (v_z = 10^8 m/s). Now consider the possibility of shear type misalignment of the streak plates, as shown in Figure 5.8 b). The electrons at the top of the beam will experience a temporally advanced streak field relative to the ones at the bottom, resulting in a temporal smear $\Delta\tau_\varphi$ given by

$$\Delta\tau_\varphi = \frac{d_a \sin\Delta\varphi}{v_z} \tag{5.19}$$

Allowing for an angle of 12º in this case due to greater alignment difficulty, one obtains $\Delta\tau_\varphi$ = 100 fs. Of course there is still ample room for improvement here, either by using a smaller aperture or better streak plate assembly tolerance.

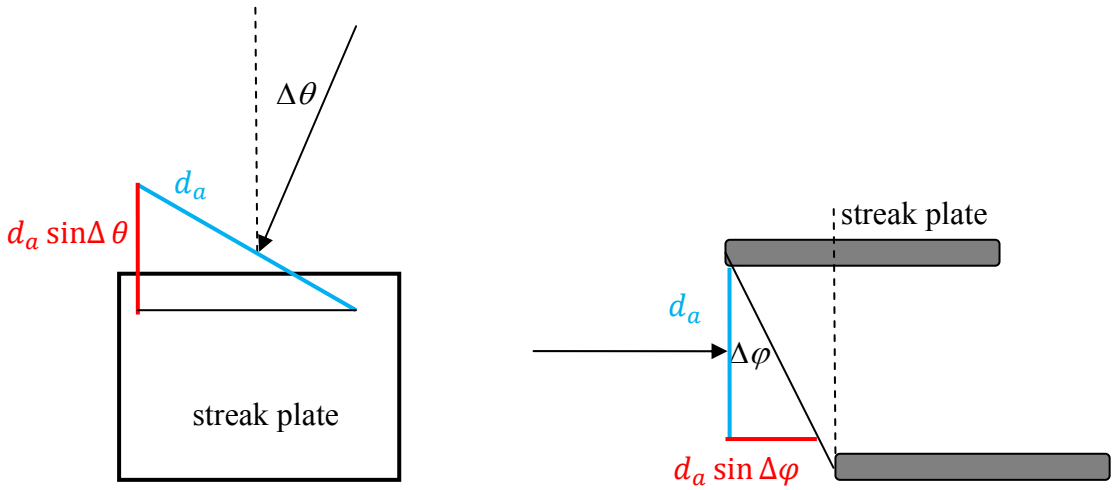

Figure 5.8. Illustration of the effect of a) beam misalignment and b) streak plate misalignment on the temporal resolution of the streak camera.

Another source of error that is dependent on the beam diameter is the fact that the streak field timing varies in the transverse direction of the streak plates. This is due to the fact that the electromagnetic field travels at a finite velocity from the photo switch across the streak plates. In the present case, this velocity is c, since the streak plates form a microstrip line with vacuum permittivity. A simple way of estimating the temporal smearing in this case is to consider the transverse streak voltage differential due to the distributed inductive reactance of the streak plates. As shown in Figure 5.9 a), the streak camera can be regarded as a transmission line with inductance per unit length L_0 and capacitance per unit length C_0. This transmission line is connected to a voltage source of angular frequency ω.

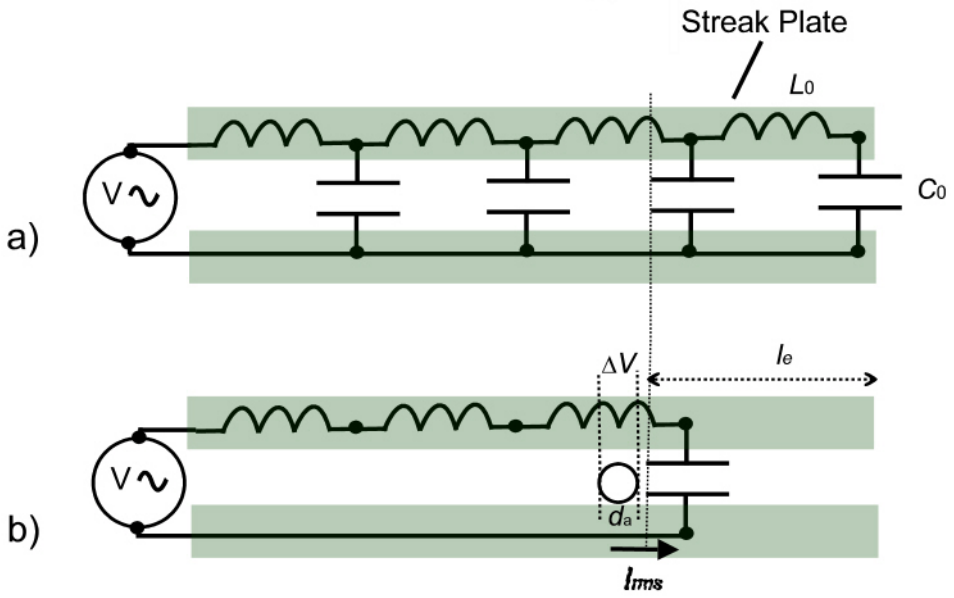

Figure 5.9. Illustration of the streak smearing due to the transmission line nature of the streak plates. a) Lumped circuit approximation of the streak plate transmission line. b) Illustration of the voltage gradient that exists across the electron beam diameter resulting from the alternating current flowing through the distributed inductive load of the transmission line.

The distributed inductive reactance and capacitive reactance per unit length are given by $X_{L0} = \omega L_0$ and $X_{C0} = 1/\omega C_0$ respectively. From $c^2 = 1/L_0C_0$ it follows that

$$\frac{X_{C0}}{X_{L0}} = \frac{c^2}{\omega^2} \tag{5.20}$$

Now, for the present case where $\omega = 3.3\times10^{10}$/s, the inductive reactance per unit length clearly dominates by many orders of magnitude. The local inductive reactance is therefore

much larger than the local capacitive reactance; since the two are in series, the effect of the capacitive reactance becomes negligible locally, resulting in the effective lumped circuit diagram Figure 5.9 b). Suppose that the electron beam traverses the streak plates a distance l_e from the edge. Since the transmission line is terminated on the right hand side, current flow is via the capacitance of the section of length l_e given by $C_e = C_0 \times l_e$. For the present case, l_e = 1 mm and C_e = 0.053 pF. The peak current into C_e is calculated via the edge capacitive reactance $X_{C,e}$ and the peak supply voltage V = 1500 V, yielding I_p = 2.7 A. The voltage drop across the beam diameter d_a = 50 μm is then given by $\Delta V = Ip \times L_0 \times d_a$ = 2.7 V. The streak angle due to this voltage difference is then easily calculated as 0.28 mrad, corresponding to a transmission line induced temporal smear $\Delta\tau_\omega$ = 55 fs.

Focussing due to fringe fields at the streak plate edge is a further source of angular spread in the streak direction. This effect increases with beam diameter as well as the displacement from the streak plate centre. Apart from inaccuracies in the positioning of the aperture, there is a limit to how close the beam can be to the centre: as discussed in Section 5.2.1 and quantified by Equation 5.9, the displacement from the centre will be at least half the drift length Δy, the latter being equal to 50 μm for the present operating parameters. To estimate the focussing angular spread, the 50 μm wide electron beam was modelled as two rays parallel to the streak plates and displaced from the streak plate centre by 75 μm and 125 μm respectively. The fringe fields were simulated for the present geometry using the Poisson Superfish code and the transverse electric field thus obtained was integrated along the two trajectories. Based on this calculation, an upper limit on the angular spread can be set at 0.2 mrad, corresponding to a temporal error due to fringe focussing of $\Delta\tau_f$ = 40 fs.

As far as jitter in the streak field itself is concerned, the possible influence of amplitude fluctuations in the initial charging voltage of the streak plates is addressed first. Assume that the streak field is of the form $E(t) = E_0 f(t)$[17] with $E_0 = E(0)$ and $f(t)$ any function such that

$$p_y = e \int_{T_m - T/2}^{T_m + T/2} E_0 f(t) dt = 0 \qquad (5.21)$$

(see Equation 5.1) for suitable timing T_m, i.e. there is zero net deflection of the electron bunch centre through the field (as usual, T is the transit time). Clearly, any fluctuation in E_0 does not alter the net deflection which is proportional to p_y: it remains zero. Slight deviations from p_y = 0 would of course lead to finite fluctuations; in fact the angular jitter would be proportional to the (near zero) deviation angle multiplied by the relative amplitude jitter, the latter being typically about 1%. Realistically it is easily possible to keep the deviation angle below 5

[17] This is a plausible assumption on the form of $E(t)$ since equation 7.12 fits the electric field data reasonably well, as seen in Figure 5.7 b).

mrad, which leads to negligible streak jitter. The same goes for the streak angle which is of course proportional to E_0. Thus it follows that amplitude fluctuations in the supply voltage are not really a problem.

A more serious concern is associated with intensity fluctuations in the trigger laser. The photo generation process in semiconductor switches itself is quasi-instantaneous, as it is for the case of the photoelectric effect in metals. In principle, there should thus be no switching jitter, just as there is no jitter in the generation of electron pulses in ultrafast photoguns. In the case of a perfectly stable laser with no shot to shot intensity variation, this indeed holds true. In practise, CPA lasers suffer from amplitude fluctuations on the order of 1%. Now, the number of photo carriers generated in the photo switch is proportional to the laser pulse energy W_l, assuming that one is not operating in the saturation regime. For the case where the switch operation of interest occurs in a time frame much shorter than the carrier lifetime, the photoinduced carrier concentration n_{ph} is constant (on that timescale) and proportional to W_l. This is the case here, since the streaking occurs within about 100 ps after triggering while the carrier lifetime is about 1 ns. The photo conductivity σ_{ph}, in turn, is given in terms of the photo carrier density n_{ph} and mobility μ_{ph} by $\sigma_{ph} = en_{ph}\mu_{ph}$ while the switch resistance R_s is inversely proportional to σ_{ph}. Assuming constant μ_{ph}, one has

$$R_s \propto 1/W_l \tag{5.22}$$

Small fluctuations in laser energy ΔW_l therefore lead to small switch resistance fluctuations ΔR_s according to the relation

$$\frac{\Delta R_s}{R_s} = \kappa \frac{\Delta W_l}{W_l} \; ; \; 0 \leq \kappa \leq 1 \tag{5.23}$$

where the factor κ accounts for possible resistance saturation at high intensities. At low laser pulse energies, Equation 5.23 is valid and $\kappa = 1$, which is the worst case scenario in terms of the magnitude of resistance fluctuations. In the saturation regime, κ becomes less as the resistance versus laser pulse energy curve begins to flatten out, and eventually vanishes at complete saturation where R_s is independent of pulse energy.

An equation for the timing jitter of the streak camera due to relative laser pulse energy fluctuations can now be derived. Since the electron pulse traverses the streak field roughly symmetrically in time around the first zero crossing, jitter in the position of this zero crossing is approximately equal to the streak camera timing jitter. The zero crossing position t_0 is calculated by setting $E(t_0) = 0$ in equation 5.21, yielding the solution

$$t_0 = \frac{\pi}{2\omega'} \tag{5.24}$$

since $\cos(\pi/2) = 0$. Recalling from equation 5.17 that ω' is a function of R_s and differentiating equation 5.24 with respect to R_s, one obtains for the rms streak camera timing jitter $\Delta\tau_{j,rms}$

$$\Delta\tau_{j,rms} = \frac{\pi R_s^2 \Delta R_s}{4L_l^2 \omega'^3 R_s} \tag{5.25}$$

The equation was multiplied by R_s in the numerator and denominator so that the relative resistance change $\Delta R_s/R_s$ appears explicitly. The quality factor Q of the LCR circuit is given by

$$Q = \left|\frac{X}{R_s}\right| \tag{5.26}$$

where X is the reactance due to L and C elements. Q can also be written in terms of the attenuation constant $\alpha = L/2R_s$ and the un-damped frequency $\omega_0 = (L_l C_p)^{-1/2}$, which is nearly equal to ω' unless the damping is very large

$$Q = \frac{\omega_0}{2\alpha} \approx \frac{\omega'}{2\alpha} \tag{5.27}$$

Equation 5.25 can then be written in terms of Q as

$$\Delta\tau_{j,rms} = \frac{\pi \Delta R_s}{4Q^2 \omega' R_s} \tag{5.28}$$

In the present case, the data fit shown in Figure 5.7 yields $Q = 3$ and $\omega' = 3.3\times10^{10}$/s. Assuming $\kappa = 1$ and $\Delta W_l/W_l = 10^{-2}$ in equation 5.23 , one obtains $\Delta R_s/R_s = 10^{-2}$. The rms timing jitter due to laser intensity fluctuations is thus predicted to be $\Delta\tau_{j,rms} = 26$ fs. The FWHM timing jitter, assuming a Gaussian distribution, is then given by $\Delta\tau_j = 61$ fs.

From equation 5.28 it is clear that the timing jitter decreases with increasing streak field frequency. Streak cameras with larger plate lengths (typically on the order of a few cm) would therefore likely have a much larger $\Delta\tau_j$ than the present design[18]. While the smaller ω' could possibly be compensated by a larger Q, there is still the problem of the ramp period that is on the order of 1 ns, comparable to the time difference between pre-pulse and main pulse. This would make it difficult to suppress the destabilising effect of pre-pulses as is done in the present design. Short of cleaning the laser pulses, the only remedy would be to lower the laser intensity which automatically results in larger R_s; this is in direct conflict with the aforementioned requirement of larger Q.

The issue of temporal smear due to the finite energy spread of the electron bunch and the finite streak plate length is now discussed. The temporal expansion of UED pulses occurs because of the longitudinal velocity spread (in the bunch rest frame) Δv_z. The resultant smear

[18] In practice this seems to be the case since all streak cameras thus far employed in UED are operating in single shot mode.

$\Delta\tau_s$ in the temporal duration during the transit time T of the pulse through the streak field is given by Equation 3.5 terms of the rms energy spread ΔE_k. For example, 30 keV UED pulses containing 5000 electrons typically have an rms energy spread of about 30 eV (see Figure 3.3), and Equation 3.5 yields a FWHM temporal smear of $\Delta\tau_s$ = 30 fs for the present streak camera parameters, which is not significant compared with the other errors.

The arguments and analyses given in this section are compelling motivations in favour of compact high frequency streak cameras such as the design presented here. As will be seen in Section 5.4, the experimental results look equally promising.

5.4 Results and Comparison to Particle Simulations

5.4.1 Dependence of Pulse Duration on Electron Number per Pulse

In Section 3.1.3, the issue of space charge broadening was discussed, and it was shown via simulations that the temporal duration of electron pulses depends to a large degree on the electron number per pulse. This dependence was investigated experimentally using the streak camera. The experimental method was as follows: with electron gun parameters the same as given previously in Section 3.3, the pulse charge was set to three different values using the attenuation filters and measured as described in Section 4.5.1. For each pulse charge setting, the aperture of the streak camera was scanned across the electron beam horizontally and vertically while observing the electron spot on the detector. By recording the spot intensity at various transverse positions, the beam centre position was estimated and the aperture was placed at this position. The trigger laser was then positioned by inspection so that it was centred roughly on the midpoint of the photo switch electrodes. Next, the streak velocity was measured by recording a displacement versus delay time trace similar to the one shown in Figure 5.7 a) except that the temporal range extended only a few ps around the zero deflection position. The gradient of this displacement versus delay time graph is equal to the streak velocity, which was found to be equal to 2.1 mm/ps, corresponding to an angular streak velocity of 5.3 mrad/ps with the camera length of 400 mm. The electron spot closest to the zero deflection position was selected as the streak image. Both streaked and unstreaked images for two different electron numbers per pulse are shown in Figure 5.10 a)

The streaked image on the right hand side is noticeably longer in the vertical (streak) direction for the case of larger electron number. The size of the un-streaked is also larger for larger electron numbers as is also apparent from Figure 5.10 b) due to a slight space charge broadening. The temporal electron current profile is of course not directly given by the binned

streak profiles of Figure 5.10 b), but can be extracted in accordance with the de-convolution method of Section 5.2.2. The regularised solution was used to generate smoothed streaked profiles (solid red lines in Figure 5.10 b)) that can be compared with the measured profiles. The regularisation parameter α was chosen such that the relative rms deviation of this re-constructed solution from the measured trace is 0.3%.

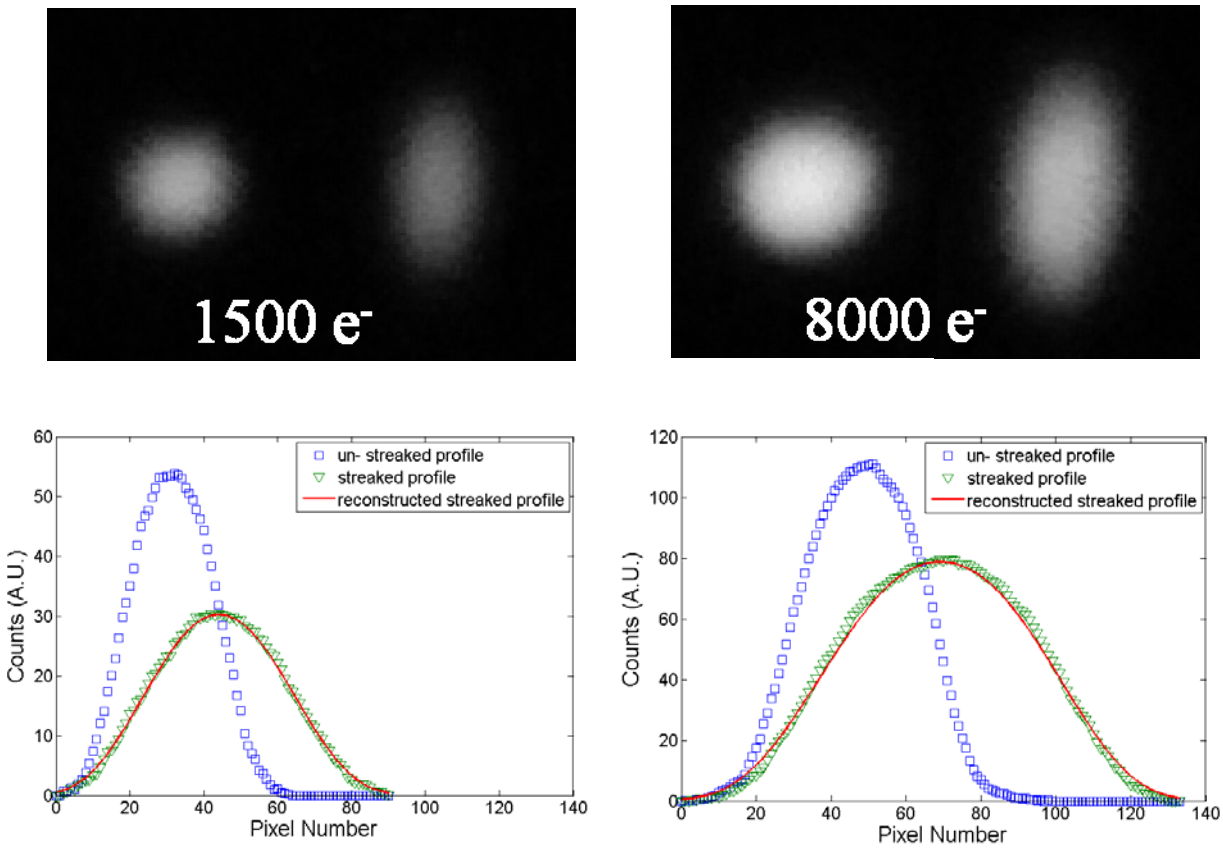

Figure 5.10. Streak images (top) recorded for electron pulses containing 1500 and 8000 electrons respectively. The horizontally binned intensity profiles of streaked and un-streaked images are displayed at the bottom. The solid red lines are the reconstructed streaked profiles subject to a Tikhonov regularisation.

The resultant temporal electron current profiles for the 1500 and 8000 electrons per pulse cases are shown in Figure 5.11 together with ASTRA simulations for comparison. The simulations were set up so as to emulate the actual experimental conditions as closely as possible: the simulated bunch was truncated at a radius of 100 μm to represent the fact that the streak camera measures a section of the pulse near the centre with a diameter of 50 μm. The reason for choosing a larger radius for the simulations is the difficulty of getting good statistical accuracy and the fact that the exact position at which the pulse was sampled is not

known with much greater precision in any case. The other simulation parameters such as the laser spot size on the cathode, UV laser pulse duration and cathode emission energy spread are the same as described in Sections 3.3 and 4.2. It is evident that the measured profiles are broader than the simulations, which is to be expected considering all the error mechanisms. The pulse shapes are also noticeably more flat-top than the simulated profiles, a feature that is particularly evident for the 1500 electrons case where the simulated profile appears Gaussian-like. This could be attributed to the fact that some of the error mechanisms, particularly those due to plate misalignment and the plate transmission line nature produce more flat top like "half circle" profiles rather than Gaussian ones. For the 8000 electrons case, the simulated profile is indeed more flat-top, and this is also reflected by the measured result. Surprisingly enough, more subtle features of the simulated profiles also show up in the measurements: the twin-peak features present in the simulations are evident in the measured profiles as a characteristic saddle shape. While other simulations do not predict a double humped profile [40], it should be noted that these simulations extend over the entire radial extent of the bunch, while the present simulations represent a narrow radial slice near the bunch centre. Indeed, simulations done in the present study corresponding to the entire electron bunch also do not yield any double-humped features. The measurement results obtained here demonstrate the capability of the streak camera to resolve not only statistical quantities such as pulse duration but actually the longitudinal electron density profile as well.

The temporal duration of three measurements corresponding to electron numbers of 1500, 6000 and 8000 electrons per pulse are shown in Figure 5.12. The measurements compare well with the simulated results (solid green line) and confirm the predicted trend of increasing pulse duration with electron number. Just as important as the measured results are the error bars, which were calculated by taking into account all the error mechanisms discussed in Section 5.3.3. Most of these error mechanisms lead to an increase in the transverse normalised emittance of the beam and can therefore only lead to broadening of the streak image, never a reduction of its width. As a result, the error bars extend mainly below the measured values. Errors belonging to this class are those due to streak plate and beam misalignment, the transmission line nature of the streak plates, laser intensity induced shot to shot timing jitter and the finite spot size induced extraction error. The latter was estimated using the method described in the last paragraph of Section 5.2.2, and values of 85 fs (FWHM) for the 1500 electrons case and 100 fs for the 6000 and 8000 electrons cases were obtained. Due to the radially un-correlated nature of the angular spread of these errors, they are added up according to $\Delta\tau^2_{\text{total}} = \Delta\tau^2_1 + \Delta\tau^2_2 + \ldots$. The fringe field focussing error results from a radially correlated angular spread, and is to be added directly to the other errors

symmetrically in the positive and negative direction. The same goes for the assumed 5% error in the streak velocity determination. The error bars in Figure 5.12 were calculated in this way from the estimations of the error mechanisms (see also Section 5.3.3).

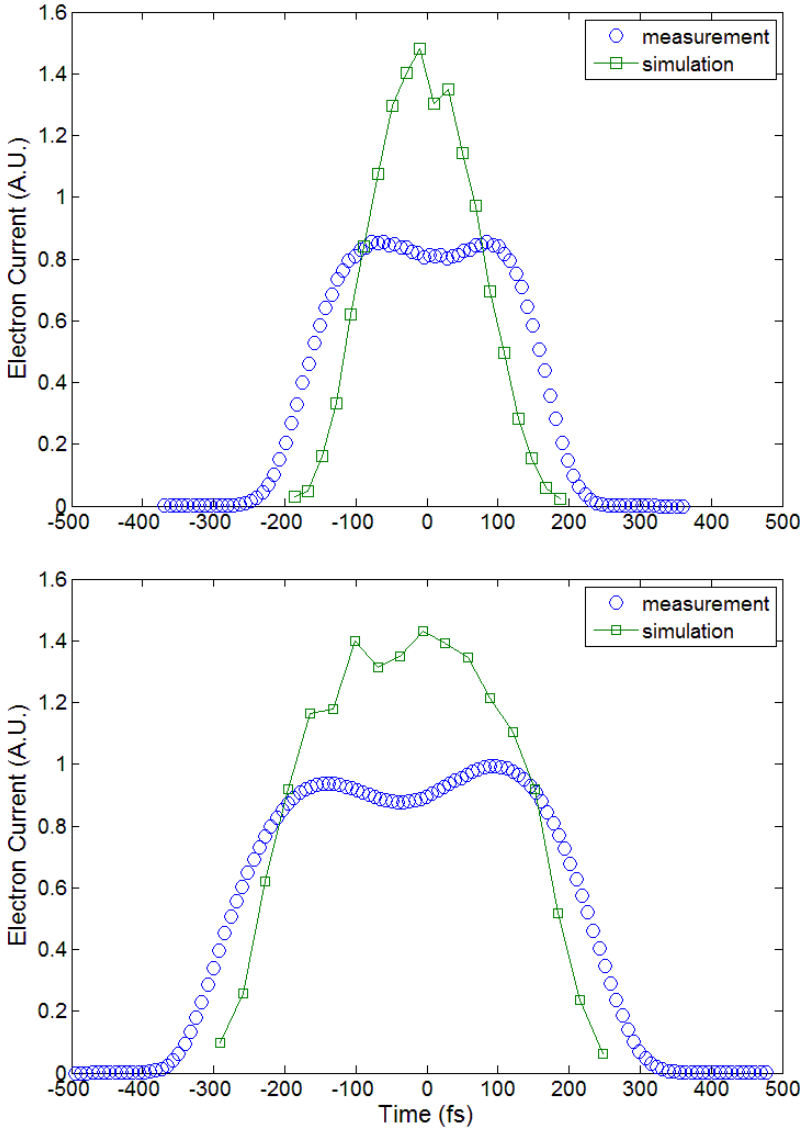

Figure 5.11. Graphs showing the measured and simulated longitudinal electron current profiles of pulses containing 1500 electrons (top) and 8000 electrons (bottom). The intensities of the simulated and measured profiles are normalised so as to correspond to the same total electron number.

The error margins obtained for the present streak camera are significantly better than what has been obtained by any other streak camera in UED thus far [53], and rival the current state of the art results obtained by the ponderomotive laser-electron pulse cross correlation technique

in terms of temporal resolution [54,55]. The main reason for the better performance is a larger angular streak velocity due to the high electric field generated by the streak plates of this design. The more sophisticated data extraction technique described in Section 5.2.2 also plays an important role in obtaining the best possible temporal resolution. It could be argued that the good temporal resolution obtained here is in part due to the relatively low electron energy of 30 kV, unlike the measurements done by Wang et al. who obtained a temporal resolution of ± 350 fs, but at 60 kV [53]. An analysis of the electron energy dependence of the temporal resolution shows, however, that the temporal resolution should be almost the same at 60 kV. The only error that increases at higher energy is the extraction error $\Delta\tau_e$. In the non-relativistic approximation, the streak velocity scales as E_k^{-1}, but the spot size on the screen scales as $E_k^{-1/2}$, which implies that $\Delta\tau_e$ is proportional to $E_k^{1/2}$. The errors due to beam and streak plate misalignment actually decrease with electron energy and scale as $E_k^{-1/2}$, while all other errors are unaffected. The total error span of the 1500 electrons pulse duration measurement is calculated as 120 fs at 30 kV, and would become a only marginally higher 126 fs at 60 kV.

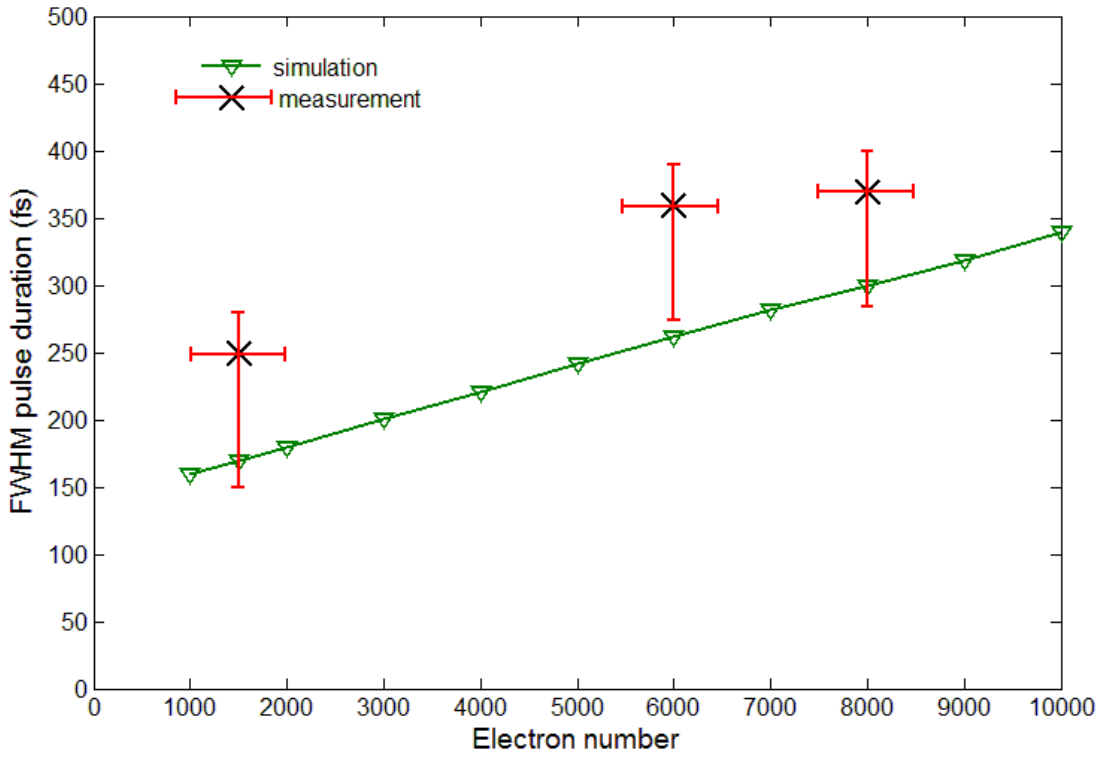

Figure 5.12. Graph showing a comparison between measured and simulated FWHM pulse durations of electron pulses from the current setup at a distance of 2 cm in front of the solenoid lens exit.

5.5 Improvements and Future Developments

The results presented in Section 5.4 represent the current state of the art in terms of the error width of temporal durations measured and detail of the longitudinal electron density that could be extracted. While the results demonstrated may be accurate enough for pulse lengths in excess of 200 fs, further improvements are needed to characterise pulses with about 100 fs or less duration. Fortunately, the streak camera design presented in this work is amenable to significant further improvements without major design modifications being necessary. Reduction of the aperture size is the easiest route to improve the temporal resolution. A detection threshold of about 120 fs instead of the current 200 fs would be possible simply by reducing the aperture size to 20 microns diameter, thereby reducing all transverse beam size dependent errors. Significant further improvement would only be possible by increasing the angular streak velocity, a measure that would reduce the data extraction error which is independent of the aperture size. This can be done by increasing the streak plate voltage, decreasing the plate separation or increasing the discharge frequency. At present, there is still significant pre-pulse induced discharging of the streak plates, resulting in a lower working voltage than allowed by the electrical breakdown strength of the GaAs photo switch. Reduction of the carrier lifetime of the photo switch e.g. by introduction of charge carrier trapping centres via electron irradiation could eliminate this discharging, effectively raising the operating voltage and thus the angular streak velocity. Shorter carrier lifetimes would also allow higher trigger laser intensities to be used, which would reduce the switch timing jitter below the currently estimated 60 fs. The author believes that the streak camera concept presented here has the potential capability to reach sub-100 fs accuracy for the temporal characterisation of electron pulses in the sub-100 keV energy range.

The measurements preformed are currently limited to a very narrow region near the bunch centre. To characterise the entire bunch, the streak camera needs to be scanned in the radial direction, measuring the longitudinal electron density at various positions. This has not yet been done successfully since such a translation of the streak camera causes a change in the position of the trigger pulse on the photo switch, resulting in timing variations due to differences in time of flight and trigger laser intensity. While the former can be corrected for quite easily from the geometry of the setup, the surest way to eliminate the effect of intensity variation is beam tracking to prevent such variations. Once this is implemented, it will be possible to obtain a more complete picture of the bunch shape. For example, one could verify the predicted uniformly filled ellipsoidal nature of highly charged electron pulses generated by fs electron pulses, which has already been achieved for relativistic electron bunches using

an rf deflection cavity [92]. Such a feat is obviously impossible with single shot high jitter streak cameras, and the required re-alignments would be rather difficult with the optical grating enhanced ponderomotive cross correlation technique [55,51].

For full 6-dimensional phase space characterisation of the pulses, it is still necessary to include measurement of the longitudinal momentum. By placing a dispersive element (e.g. a spectrometer with crossed *E* and *B* fields) behind the streak camera such that the dispersion direction is perpendicular to the streak direction, it will be possible to obtain the longitudinal position-momentum correlation (chirp) of the pulses. Such information will be very useful if one wishes to develop UED sources that make use of compression techniques, as discussed in Chapter 6.

6. PULSE COMPRESSION: NOVEL CONCEPTS[19]

While ultrafast electron diffraction already has a significant advantage over the competing technique of ultrafast X-ray diffraction in terms of scattering efficiency and brightness of table top sources, UED is generally not a single shot technique at the present time [10]. Near single-shot structural determinations do exist for small molecules and large electron beam cross sectional area [18], but the single-shot determination of larger structures would require a larger electron bunch brightness. In view of processes that are not reversible, such as most phase transitions, chemical reactions and transformations of biological molecules, it has been identified as an important quest to significantly increase the brightness of UED sources [10]. The UED diffractometer described in Chapter 4, which was based on the pioneering work of B.J. Siwick et al. [12,17,40], has been designed to overcome the brightness limitations of femtosecond electron pulses imposed by space charge forces up to electron numbers of about 10^4. For near single shot structural determinations, this number would optimally have to be increased by between one and two orders of magnitude while pulse durations should be decreased to the sub-100 fs range. This chapter gives a brief review of the progress that has been made in the development of high brightness UED sources, with particular emphasis on pulse compression concepts in the sub-relativistic regime. The core of this chapter is formed by two novel pulse compression concepts which have been developed by the author: achromatic reflectron compression (Section 6.2) and pulsed cavity compression (Section 6.3). The author believes that both of these concepts will be easier to implement than conventional compression techniques, and both are verified through detailed numerical simulations.

6.1 Motivation for the Development of Pulse Compression Sources

One of the great challenges facing the UED experimenter is to obtain sufficiently bright beams that allow femtosecond temporal resolution without compromising spatial resolution. Since the spatial extent of femtosecond electron pulses is necessarily small in the propagation direction, even relatively small electron numbers can lead to significant charge densities, which in turn leads to rapid pulse broadening and concomitant development of significant longitudinal energy spread (see Section 3.1.3 and 3.3). A beam consisting of pulses containing 10^4 electrons, for example, will have an average current of only 1.6 picoamperes assuming a pulse repetition rate of 1000 Hz, which is many orders of magnitude less than typical average beam currents in conventional electron diffractometers. Single-electron detection and long integration times can, to a large extent, make up for this deficit. It would

[19] Sections 6.1 and 6.2 are based on the published article Kassier et al. [32]

however still be highly desirable to maximize the number of electrons per pulse since not only does this increase the average beam current, but also less sample area would then be required in pump-probe experiments involving irreversible processes.

Since electron guns operating in the sub-300 fs range without using pulse compression techniques seem to be limited to a brightness of less than 10 000 electrons per pulse, new electron sources must be found that surmount this barrier. There are a number of ways to achieve this. By accelerating the electron bunches to relativistic energies (a few MeV) the space charge induced de-bunching is strongly suppressed (see Equation 3.8). In addition, the RF photoguns employed for the acceleration of MeV electron beams allow compression of the electron pulses to shorter durations than the generating laser pulse [46]. As a result, relativistic electron bunches suitable for diffraction experiments with a temporal duration in the 100 fs range and a bunch charge of about 3 pC range can be created [46,47]. Even larger bunch charges are possible if the electron pulse is allowed to be several ps long and the temporal resolution is achieved by dispersing the diffracted signal with a deflection mode cavity, as shown by Musumeci et al. [93]. In this way it is possible to gather, in a single shot with a bunch charge of 20 pC, structural information about a specimen with sub-100 fs temporal resolution over a time span of a few ps. This approach may also be feasible for sub-relativistic UED. While MeV UED certainly shows the most promise in the quest for true single shot structural determinations of matter, the required technology is bulky and expensive, thus making wide proliferation of such devices unlikely. Table top UED systems therefore employ sub-relativistic electron energies. An interesting concept proposed by Baum and Zewail is to use expanded (several ps duration) chirped electron pulses for UED diffraction experiments [94]. By exploiting the fact that there is a highly predictable time-energy correlation in such pulses, a temporal resolution of about 40 fs is in principle achievable by filtering out a narrow energy band from the diffracted signal. While the total bunch charge can be large ($10^4 – 10^5$ e^- per pulse) the concept as proposed by Baum et al. only allows a small portion (corresponding to the selected energy band) of the pulse to reach the detector, and thus nothing is gained in terms of effective electron number per pulse. In principle it should however be possible to allow scattered electrons from the entire pulse to reach the detector measuring for example the diffracted signal along one direction of the detector while the energy dispersion (related to arrival time by the chirp) is in the perpendicular direction. This possibility, which is somewhat similar to the streak camera concept of Musumeci et al. [93], was not discussed by Baum and Zewail.

Finally, one has the possibility of pulse compression that can enhance the effective electron number per pulse while retaining high temporal resolution. The transverse beam

quality as measured by the transverse normalised emittance $\varepsilon_{n,x}$ has been shown to be insensitive to the effect of electron densities up to the 10^5 electrons per pulse range for non-relativistic bunches [41], making the creation of femtosecond bunches in this charge range via compression techniques an attractive possibility. While the longitudinal emittance $\varepsilon_{n,z}$ is much less forgiving of large pulse charges, femtosecond pulses can nonetheless be attained at the cost of a relatively large longitudinal rms energy spread (see Section 3.3). As a result, compressed electron bunches typically have a much larger longitudinal emittance and therefore a much smaller longitudinal coherence length $L_{c,z}$, but it is still possible to have $L_{c,z} \sim L_{c,x}$. UED bunch compression is therefore a worthwhile undertaking. The highest conceivable electron densities at the sample can be obtained if the electron pulse reaches its peak density exactly within the pulse-sample interaction region, with the unavoidable broadening of temporal and energy spread occurring outside this region. The sample should, in other words, be at a longitudinal (temporal) focus of the electron pulse.

At such high electron densities the internal space charge forces are considerable, and high quality beams are only possible if these space charge forces are nearly linear. This is the case for uniformly charged ellipsoidal electron bunches, which have been shown to obtain in a rather straightforward manner from femtosecond pulses generated at a photocathode [41]. Radio frequency compression of DC accelerated photoelectrons is a routine method for achieving bright femtosecond pulses, and recently a very promising electron diffraction gun concept has been published based on this [44]. The relatively complicated geometry of the required RF cavity, as well as the fact that complicated schemes for synchronization of the RF cavity and the femtosecond laser are required would, however, hamper the easy realization of such a design [95]. In the remainder of this chapter, alternatives to RF compression that would be simpler to implement are described.

6.2 Achromatic Reflectron Compressor

6.2.1 Overview of the Setup

The difficulties outlined in Section 6.1 concerning RF compression could be avoided if the longitudinal focusing were instead achieved by much simpler static electron optics. In ion optics, the time of flight of different ion species is routinely controlled using an electrostatic mirror, also known as a reflectron [96]. It has been shown that the reflectron can be used to compensate for the temporal spread of photo-emitted electron pulses induced by their finite energy distribution, thereby allowing recovery of the femtosecond pulse duration present at the photocathode [97]. In this section, it will be shown through particle simulations that the

reflectron concept is applicable even in the space charge dominated regime and that a design involving a reflectron is suitable for achieving high charge density femtosecond electron pulses with excellent spatial and temporal resolution capability.

For compression of high charge density bunches containing ~10^5 electrons to the femtosecond time domain whilst retaining favorable beam parameters and using only electrostatic and magnetostatic components, consider the setup shown in Figure 6.1. It consists of the usual direct current (DC) photogun, two solenoidal electron lenses S_1 and S_2, two bending magnets B_1 and B_2 and a reflectron, which is simply a uniform electrostatic field acting as a dispersive electron mirror. The electron gun is similar to the one described in Sections 3.3 and 4.3.1, except that the solenoid lens S1 has a larger inner bore diameter of 15 mm instead of 7 mm to reduce transverse normalised emittance growth. The acceleration distance from anode to cathode is also larger for the case of 100 keV acceleration potential.

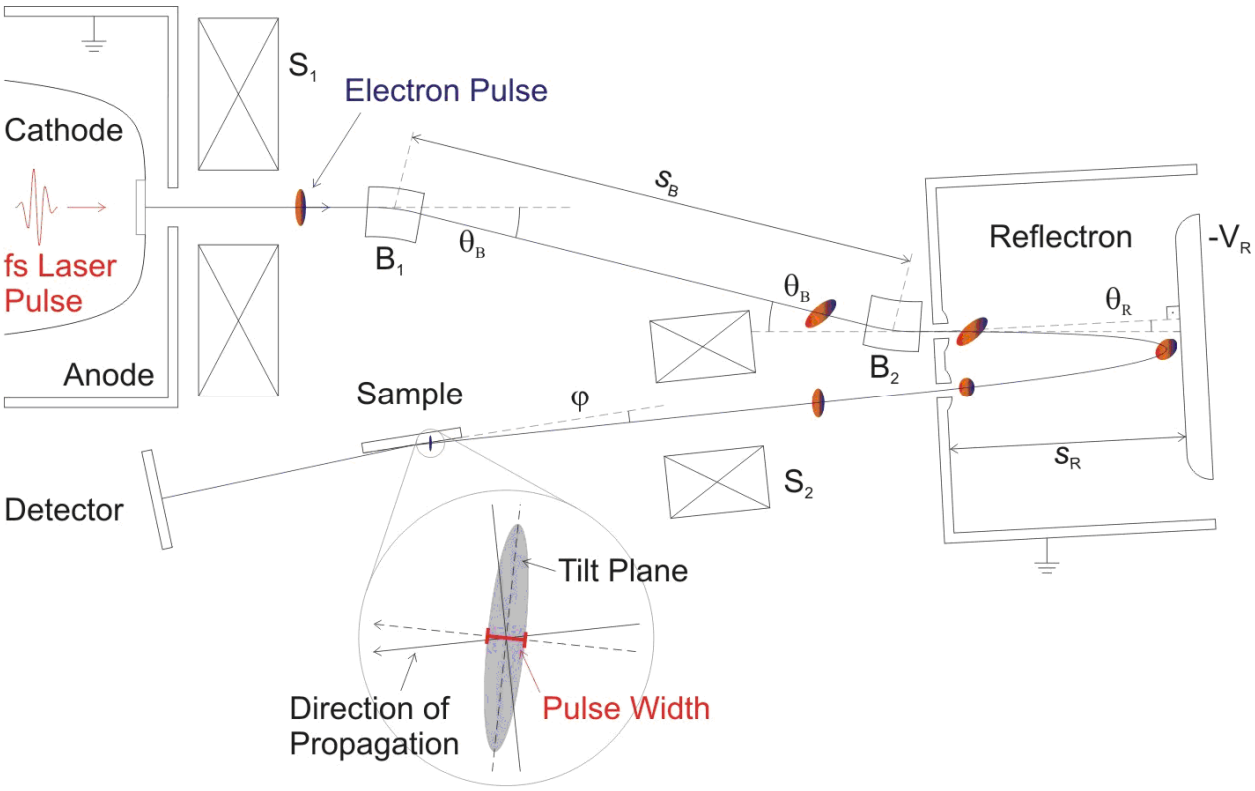

Figure 6.1. Schematic of the proposed femtosecond electron gun employing a dispersion-compensated reflectron bunch compressor. The bunch is pre-dispersed by a pair of bending magnets B_1 and B_2 with bending angle θ_B and a separation distance s_B. A reflectron of length s_R and inclination angle θ_R to the horizontal reflects and compresses the pulse onto the sample with incident angle φ. Typical electron pulse shapes at various points in the setup are also shown. At the sample, the pulse front is tilted relative to the propagation direction by a few degrees as seen by the blowup in the figure. The shortest pulse width occurs in a direction normal to the tilt plane.

Lens S_1 reverses the considerable transverse expansion of the pulse due to space charge expansion and the de-focusing effect of the electric field at the anode opening. The pair of bending magnets then disperses the bunch so that faster electrons are deflected less in the horizontal *y*-direction. The angular dispersion at the end of B_2 is zero, but there will be an offset dispersion as the bunch enters the reflectron. Inside the reflectron, faster electrons, which are initially ahead of the bunch center, travel further longitudinally along the reflectron axis. This results in a reversal of the velocity-position correlation at the reflectron exit such that the faster electrons are trailing the slower ones, leading to ballistic self-compression of the pulse. Due to the finite entry angle, the faster electrons also travel further in the horizontal direction. Since the slower electrons have a head start on the faster ones due to the bending magnet dispersion, the net dispersion at the end of the reflectron will be approximately zero for proper choice of θ_B, θ_R, s_B and s_R. For a more detailed discussion of expansion dynamics of highly charged photo emitted DC-accelerated electron pulses the reader is referred to [44]. Reflectron compression is discussed in Section 6.2.2, and an approximate relation will be derived for minimizing the total dispersion. A second solenoid lens S_2 is required to focus the electron beam so that the extensions of the trajectories at the sample (or rather slightly beyond the sample as discussed in Section 6.2.4) converge at a focal point on the detector. Typical pulse shapes (not to scale) are also indicated in Figure 6.1. The finite reflectron entry angle gives rise to a pulse front tilt at the temporal focus which has to be taken into account in the design of the experiment if the maximum possible temporal resolution is to be achieved. This phenomenon has been observed previously [97], and will be discussed in greater detail in Section 6.2.3. Reflectron compression is now discussed in more detail.

6.2.2 Reflectron Compression

While the transverse expansion can be reversed by regular electron lenses, longitudinal compression is conventionally achieved by one of two methods: Radio frequency (RF) cavity compression or magnetostatic compression. The latter is most effective at fully relativistic energies where it is the technique of choice [98], while the former is more effective at sub-relativistic or mildly relativistic energies, including the 100 kV range for electron diffraction as shown by van Oudheusden et al. [44]. Due to the technical difficulties associated with RF compression, it is desirable to make use of static compression techniques. One possibility in the sub-relativistic energy range, known to researchers in the field of time of flight ion mass spectroscopy, is the use of a reflectron. Although the reflectron has previously been considered for compression of femtosecond electron bunches [97], detailed numerical

simulations considering all relevant beam properties for electron diffraction are not available, nor has the applicability of reflectron compression for highly charged pulses been established. To see how reflectron pulse compression is achieved, consider a chirped bunch incident parallel to the electric field of a reflectron as shown in Figure 6.2 a). The bunch is represented by its two outmost particles b and b' with momenta p and p-Δp in the +z-direction respectively. This means that the particles at the front have more momentum than the trailing ones, as is the case in DC-accelerated photo-generated electron pulses. Due to its negative chirp, such a pulse will continue to broaden in the absence of external fields.

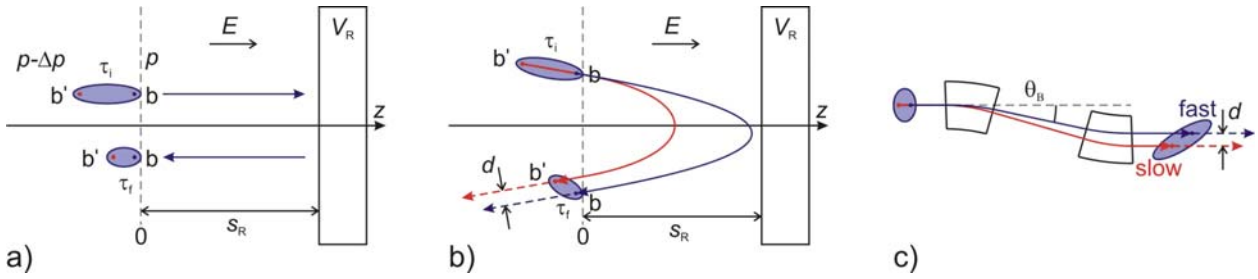

Figure 6.2. a) Illustration of the chirp-inverting effect of a reflectron with potential V_R, length s_R and electric field E. The incident pulse with fast (blue) electrons of momentum p at point b in front and slower (red) electrons of momentum p-Δp at point b' at the back is reversed in both direction and chirp. The initial and final pulse durations are denoted by τ_i and τ_f respectively. b) Dispersion of the pulse entering the reflectron at an angle. Faster electrons travel further parallel and perpendicular to the z-direction. c) Dispersion due to a pair of bending magnets. Slower electrons undergo a larger deflection.

Let the reflectron entrance be located at $z = 0$, and denote the initial temporal spread of the pulse by $t_i = t_b - t_{b'}$ where t_b and $t_{b'}$ are the arrival times of particles b and b' at $z = 0$ respectively. Neglecting space charge effects, a particle with momentum p subject to a uniform electric field E obeys the following equation of motion

$$\int_{p}^{-p} dp = -\int_{t0}^{t1} eEdt = -\int_{t0}^{t1} \frac{eV_R}{s_R} dt \tag{6.1}$$

where e is the elementary charge and V_R and s_R the reflectron voltage and total reflectron length respectively. Evaluation of the integral in Equation 6.1 allows one to solve for the time the particle spends inside the reflectron:

$$t_R = \frac{2s_R}{eV_R} p \tag{6.2}$$

The resulting time difference introduced between particle b and b' is

$$\Delta t = \frac{2s_R}{eV_R}\Delta p \tag{6.3}$$

which implies that

$$\tau_f = \tau_i + \frac{2s_R}{eV_R}\Delta p \tag{6.4}$$

Since τ_i is negative (negative chirp), one obtains a positively chirped pulse in the post-reflectron drift region if $2s_R\Delta p/eV_R > \tau_i$. It is thus possible to create a self-compressing pulse using a reflectron. If the incident pulse has a linear position-momentum correlation, its time-momentum correlation will also be linear if $\Delta p << p$. Inspection of Equation 6.4 reveals that the reflectron preserves the linearity of the chirp, and thus one would expect a large degree of longitudinal emittance conservation.

To be of use in practice, the entry angle into the reflectron cannot be parallel to the reflectron field since this would preclude the possibility of placing a sample in the beam path. In addition, there must be sufficient clearance between the electron gun and the electron detector. The bunch must therefore enter the reflectron at a sufficiently large angle θ_R. Instead of straight-line trajectories, the orbits inside the reflectron will now be parabolas in the case of non-relativistic electrons, as shown in Figure 6.2 b).

An approximate formula that is useful in estimating the reflectron dispersion and finding a condition that minimizes this dispersion in the presence of a pair of bending magnets will now be derived. It must be stressed however that the detailed particle simulations in Section 6.2.3 do not depend on the simplifying assumptions now used, although they verify that the approximations used are reasonable. Assuming $p = mv$ and neglecting focusing and space charge effects, the range in the transverse direction is given by $y = vt_R \sin\theta_R \cos\theta_R$. This reduces to

$$y = \frac{2s_R\theta_R mv^2}{eV_R} \tag{6.5}$$

using Equation 6.2. and assuming small θ_R. To calculate the dispersion distance d, one assumes a bunch centre velocity v and a constant velocity spread Δv with $\Delta v << v$ so that $(v + \Delta v)^2 - v^2 \sim= 2v\Delta v$. The range difference $\Delta y = d$ between particles of velocity $v + \Delta v$ and v respectively after the pulse has passed through the reflectron is then equal to

$$d = \frac{4s_R\theta_R mv\Delta v}{eV_R} = \frac{4s_R\theta_R\Delta E_k}{E_k} \tag{6.6}$$

where the last equality follows from $\frac{\Delta p}{p} = \frac{\Delta E_k}{2E_k}$ combined with $E_k = ½\ mv^2$ and $E_k = eV_R$ for sufficiently small θ_R. While d is negligible in the case of electron pulses whose energy spread

is dominated by the photo-emission process (ΔE_k ~ 0.4 eV), the simulations show that a highly charged 30 keV bunch containing 10^5 electrons typically has an rms energy spread of about 200 eV, for which d = 0.1 mm assuming a reflectron entry angle of 4 degrees and reflectron length of 60 mm. This is comparable to typical rms bunch radii, and considerable transverse emittance growth will result if the dispersion is not corrected. The latter is achieved by pre-dispersing the bunch using a pair of bending magnets as shown in Figure 6.1 and explained in Figure 6.2 c). Using the fact that the radius of curvature of the trajectory in a bending magnet is proportional to the particle velocity v it can be shown that, for sufficiently small bending angles θ_B

$$d_B = \frac{-s_B \theta_B \Delta v}{v} = \frac{-s_B \theta_B \Delta E_k}{2E_k} \tag{6.7}$$

where s_B is the bunch path length between the bending magnets and the negative sign indicates that particles of larger velocity are deflected less in the y-direction than their slower counterparts. The pair of bending magnets therefore tends to cancel the reflectron dispersion, and the total dispersion is matched to zero at the reflectron exit if

$$\theta_B s_B = 8\theta_R s_R \tag{6.8}$$

Since this condition is independent of both the bunch centre energy and the energy spread, a given setup should work well over a wide range of bunch charges and acceleration voltages without significant adjustments being necessary. This is verified through numerical simulations in Section 6.2.3. Even though this approximate relation neglects relativistic effects and assumes that Δv is constant (which it is generally not), it is a useful design aid. Fine-tuning of the parameters will of course have to be done with the help of detailed simulations such as the ones discussed in Section 6.2.3, which do not depend on any of the simplifying assumptions used to derive Equation 6.8.

The bending magnets employed in the setup need a brief discussion. As deflection magnets, both Helmholtz-type coils and sector magnets with iron pole pieces are suitable. The latter are however more straightforward to model in particle simulations as they can be well approximated as a region of uniform magnetic field that is abruptly terminated by a straight edge boundary. Apart from deflecting a beam, bending magnets generally act as thick astigmatic lenses. In the direction of the deflection (y-direction) this arises from a geometric effect while in the vertical x-direction edge fields have a focusing effect for beams that enter at a nonzero angle with respect to the edge normal. The focal lengths for horizontal focusing of a sector magnet with edges normal to the beam trajectory and vertical focusing by a single edge are given by [68]

$$f_y = \frac{r}{\tan\alpha} \tag{6.9}$$

$$f_x = \frac{r}{\tan\beta} \tag{6.10}$$

where r is the bending radius , α the deflection angle ($\alpha = \theta_B$ in our case) and β the edge inclination angle. Equation 6.10 will change for nonzero β, and it is in fact possible to achieve stigmatic focusing with proper choice of β for both edges of a sector magnet.

6.2.3 Simulation Detail and Results

For the electron gun a relatively simple geometry was chosen consisting of a back-illuminated rogowski-type photocathode and a planar anode with circular exit opening of radius 1 mm. The distances from cathode to anode are 3 mm and 10 mm at accelerating potentials of 30 kV and 100 kV respectively. This type of electron gun is experimentally well established [12,45]. The electric field has been calculated using the Poisson-Superfish set of codes [61], and using the simulation it was verified that the electric field does not exceed 10 MV/m at any point in the geometry, which is important to prevent possible vacuum breakdown at metal surfaces.

An inner bore diameter of 15 mm and 10 mm respectively was chosen for the solenoid lenses S_1 and S_2, and both lenses have a magnetic gap of 10 mm. The magnetic field profiles of the respective geometries were simulated with Poisson-Superfish; the reflectron geometry can be seen in Figure 6.3. Because of lack of radial symmetry of the actual reflectron due to the fact that two entry openings are used as shown in Figure 6.1, the Poisson-Superfish simulation in Figure 6.3 is only an approximation which was used for simulation purposes. Since the potential does not vary appreciably in the radial direction on the length scale of the separation between the two entry openings of the reflectron, and since their separation is large compared to their diameter, this simplification should not severely compromise the accuracy of the results.

The simulations of the setup discussed in the previous section have been performed using the ASTRA [59] and CSRTrack [57] codes (see Sections 3.2.1 and 3.2.2 for an overview of space charge tracking codes and a brief description of the ASTRA code). The photoemission process and tracking through straight sections of the beamline as well as all sections involving electrostatic fields have been simulated using ASTRA, while the bending magnet sections have been simulated using CSRTrack. Since the latter is inaccurate for long straight beamline sections [99], the straight section length handled by that code has been kept to a minimum. The number of macroparticles in the simulations has been set equal to the actual electron

numbers for bunches containing up to 50 000 electrons, while in the case of bunches containing more electrons, a maximum of 64 000 macroparticles was used. For the photoemission process, the cylindrical symmetric algorithm in ASTRA has been used, and image charge effects have been included. The number of both the longitudinal and radial sections was set to 12 slices. Radial uniform and longitudinal Gaussian emission profiles have been assumed throughout, and the initial energy spread of the bunch at the photocathode was modelled as a "Fermi-Dirac" distribution with assumed values for Fermi energy, effective work function and photon energy of 5.5 eV, 4.5 eV and 4.9 eV respectively, so that the total energy spread is 0.4 eV. The emission time used was 30 fs FWHM and the temporal integration step size for the emission process was set to 1 fs. The cylindrical symmetric algorithm was only used for the first 1 mm of propagation distance, where after the full 3-dimensional algorithm available in ASTRA ("3D FFT") was chosen with the bunch divided into 32 segments in each direction. The on-axis profiles of the simulated electrostatic and magnetic fields were generated and used in the ASTRA simulations. The bending magnet sections were simulated using the CSRTrack code. Bending magnets are approximated by hard-edged regions of uniform magnetic field and tracking is done by replacing the bunch with Gaussian sub-bunches which experience a force due to a meshed field that is computed using a pseudo-Green's function. Tracking was performed using the "csr_g_to_p" method [99] with ellipsoidal sub-bunches of size 10 μm in each direction.

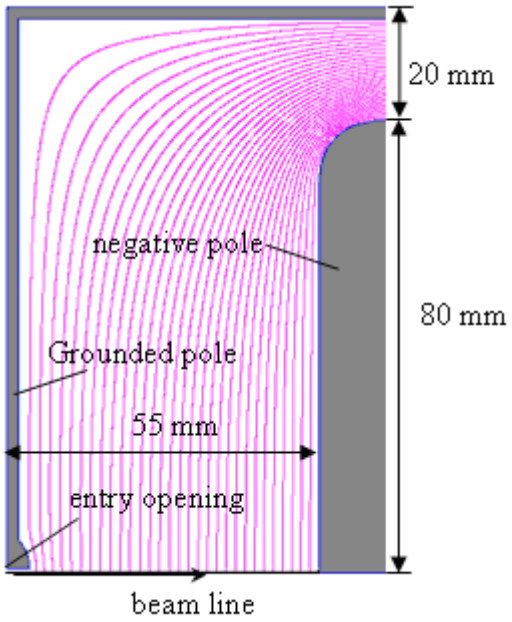

Figure 6.3. Geometry and potential lines of the 54 mm reflectron. The electron bunch enters and exits the reflectron at the entry opening on the ground pole side (see also Figure 6.1) and turns around at the negative pole. The geometry differs slightly from the reflectron depicted in Figure 6.1 in that only one entry opening has been simulated.

The simulations can be divided into two parts: a 64 mm reflectron design operating at 30 kV and a 55 mm design operating at 100 kV. The reason for this choice of voltages is that most existing or proposed ultrafast electron guns work in this energy range. Various bunch charges in the range 2 000 to 200 000 electrons were used in the simulations which demonstrate the versatility of the setup. Figure 6.4 shows the radius of the electron pulse σ_x and its duration σ_t as they evolve along the propagation distance from the photocathode through the reflectron to the target. Their evolution is shown for the 30 kV (solid lines) and 100 kV (dotted lines) designs. The evolution starts with a severe radial expansion at the anode opening caused by a combination of space charge effects and the electric field curvature. This is reversed by solenoid S1, as can be seen by the radius versus z distance curves. An additional kink a short distance after S1 testifies to the focusing effect of bending magnet B1, while further focusing is evident at B2 which is located just before the reflectron entry. The latter has a slight de-focusing effect which, assisted by space charge forces inside the reflectron, causes the bunch to reach a minimum radius whereupon the radius increases again to be focused onto a waist at the sample by solenoid S2. In the longitudinal direction, the familiar space charge induced temporal broadening occurs in the drift space between the electron gun and the reflectron. This broadening is more severe for lower energy (30 kV) pulses than in the case of their 100 kV counterparts due in part to the fact that the latter spend less time in the drift space. After passing into the reflectron, longitudinal compression of the pulses already begins to set in since the electrons at the front of the pulse start decelerating before the ones at the back. This relatively slow compression continues until the pulse passes through the reflectron exit, where the trailing electrons (which were originally in front) are further accelerated relative to the front ones, leading to rapid compression and longitudinal focusing.

The parameter values for the 30 kV and 100 kV electron gun designs that have been found using the particle simulations are summarized in Table 6.1. Other than the values quoted in the table it is worth mentioning that the arc length of the beam inside the bending magnets is 10 mm and 6 mm for B1 and B2 respectively. The angles between the beam and the edge normal of the bending magnets was in the range 2.8 and 4 degrees, the main optimisation criterion being that the focus at the sample be stigmatic. No change of these angles was necessary when varying the pulse charge, but slight modifications were made when changing the energy from 30 kV to 100 kV. As can be seen in Table 6.1, only slight changes in the setup are required to vary the electron energy from 30 kV to 100 kV. The optimised bunch parameters at the sample are summarized in Table 6.2. For a relatively small 2000 electron bunch at 30 kV, the rms temporal duration σ_t = 64 fs is shortest. In comparison,

a simulation of a 3 cm direct ultrafast electron gun yields an rms pulse width of 100 fs with 2000 electrons per pulse, 100 μm rms pulse radius and transverse emittance of 8 πnm. Thus the reflectron setup can produce shorter pulses than a direct short gun with pulse radius, electron number and transverse emittance being the same.

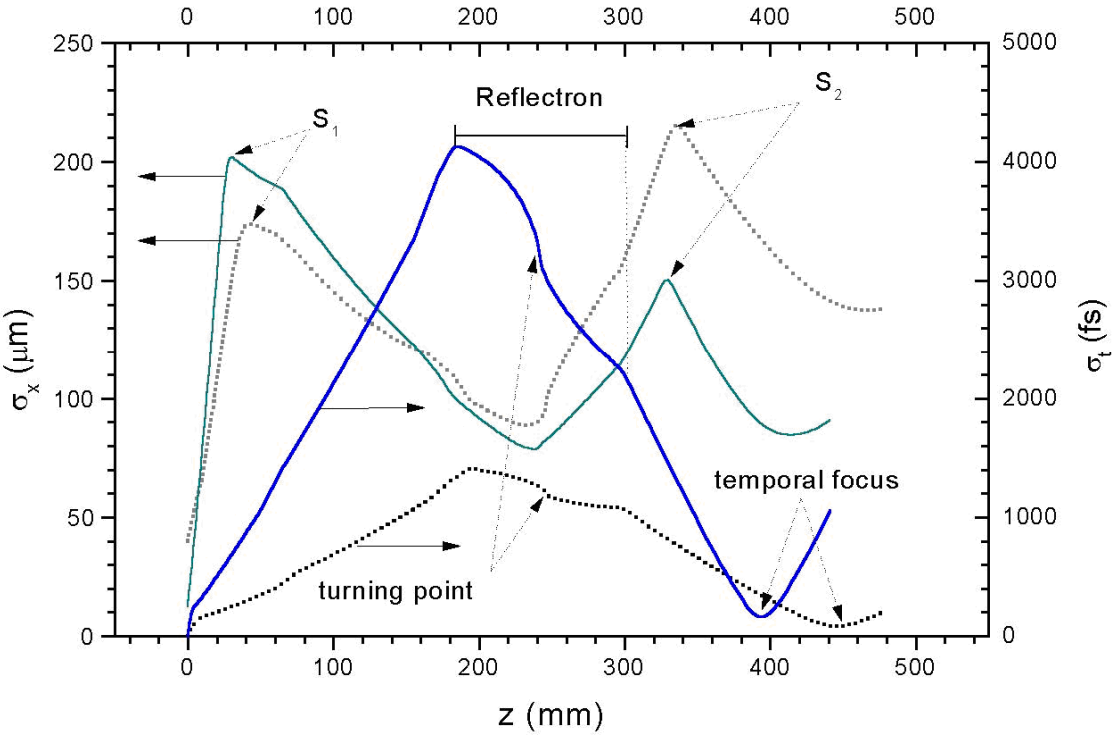

Figure 6.4. Rms Pulse radius σ_x and rms temporal duration σ_t versus propagation distance z for the 30 kV (solid lines) and 100 kV (dotted lines) designs. Pulse duration values σ_t are calculated assuming a constant bunch centre velocity corresponding to 30 kV and 100 kV for the respective pulses. The position of the solenoid lenses, the reflectron and the temporal foci are shown.

Table 6.1 Design parameters for the reflectron gun. s_g ,s_B and s_R are the distances of the acceleration gap, the distance between the centres of the bending magnets and the reflectron length respectively. θ_B *and* θ_R denote the bending magnet deflection angle and the reflectron incidence angle respectively while s_{S1} , s_{S2} and s_{sample} are the electron flight distances from the cathode at solenoids S_1 , S_2 and the sample respectively. All distances are given in mm.

V_{acc}	s_g	s_B	s_R	θ_B	θ_R	s_{s1}	s_{s2}	s_{sample}
30 kV	3	104	64	14	2.8	25	340	400
100 kV	10	102	55	16	2.5	37	300	450

The power of the reflectron setup becomes more apparent at higher electron densities. As seen in Table 6.2, 50 000 electrons can be compressed into a pulse of width σ_t = 136 fs.

According to simulations, a direct short gun can accommodate only about 5000 electrons in a pulse of similar temporal duration, pulse radius and transverse emittance, and thus the reflectron represents an improvement of one order of magnitude in 30 kV ultrafast electron pulse brightness over more conventional designs.

Temporal and spatial pulse profiles of the 30 kV pulse containing 50 000 electrons at temporal focus can be seen in Figure 6.5 a), c) and d). The pulse front is tilted relative to the xy plane which is normal to the propagation direction as shown in Figure 6.1, resulting in a projected pulse duration of 260 fs, as can be seen in Figure 6.5 a) and d). This tilt angle is about 3 degrees for this particular setup and is caused by the fact that the pulse compresses along a direction that is not parallel to the original expansion direction. The tilt angle need however not compromise the temporal resolution, provided that either the sample or the pump pulse in a pump-probe experiment are also tilted accordingly [97]. Therefore the optimal fitting plane to the pulse was calculated, and the σ_t values in Table 7.2 as well as the current density profiles shown in Figure 6.5 a) and b) have been calculated normal to this fitting plane rather than the xy plane perpendicular to the propagation direction (see Figure 6.1). It should be noted that the FWHM pulse width of 260 fs contains 79% of the electrons, which is slightly more than the 76% that would be contained in the FWHM of a perfect Gaussian pulse.

Table 6.2. Optimal values of important bunch parameters at the sample. In the transverse direction, both the values in the x and y-direction are reported due to the slight astigmatism of the beam focus. The rms temporal duration σ_t is calculated with respect to the tilted plane that best fits the bunch at the temporal focus (see Figure 6.1).

V_{acc} (kV)	n	σ_x / σ_y (μm)	σ_t (fs)	$\Delta E_{K,rms}$ (eV)	$\varepsilon_{nx} / \varepsilon_{n,y}$ (πnm)	$\sigma_{\theta,x} / \sigma_{\theta,y}$(mrad)	$L_{c,x} / L_{c,y}$ (nm)
30	2 000	93 / 99	64	33	8 / 8	0.55 / 0.54	4.7 / 5.0
30	50 000	110 / 109	135	115	10 / 11	0.60 / 0.63	4.4 / 4.4
100	100 000	113 / 110	76	220	20 / 21	0.34 / 0.35	2.2 / 2.0
100	200 000	140 / 139	81	310	26 / 28	0.36 / 0.37	2.1 / 1.9

The transverse (front view) pulse shape depicted in Figure 6.5 c) is seen to be almost circular. The transverse parameters in the *x* and *y* directions are slightly different due to the fact that the setup is not radial symmetric. However, important parameters such as the rms angular spread σ_θ and the transverse normalized emittance ε_n differ by less than 5% in the *x* and *y* directions, as seen in Table 6.2. For the 30 kV pulses, an initial rms pulse radius of 12.5 μm at the cathode was used, yielding an initial $\varepsilon_{n,x}$ of 8 πnm. Clearly, as seen in Table 6.2, $\varepsilon_{n,x}$ and

$\varepsilon_{n,y}$ do not increase considerably from the initial value even for the 50 000 electron pulses, which attests to the good optical quality of the reflectron gun. At the sample, the transverse emittance of the 50 000 electron pulse allows a transverse coherence length of 4.4 nm according to Equation 2.21. The angular spread σ_θ has been optimised for a camera length of about 20 cm. The required beam divergence is then approximately 0.5 mrad for typical bunch radii at the sample. This is more than sufficient for inorganic crystals which typically have unit cell dimensions in the sub-nm range. Many organic and biological molecules are also smaller than 2nm, and thus the electron pulses described here are suitable for studying a wide range of molecular structures. At 100 kV the statistics also look promising. Taking account of the respective pulse radii and electron numbers, one calculates for the 100 kV, 200 000 electron pulse an aerial electron density of 2.5 times that reached in the 30 kV, 50 000 electron pulse. In addition, the pulse duration is significantly shorter, the details of which are depicted in Figure 6.4 and Figure 6.5. Although the FWHM duration of 130 fs (as measured normal to the tilt plane) pertaining to the 100 kV pulse is half that of the 30 kV pulse, it should be noted that it contains only 66% of the total electron number, less than is the case for a perfect Gaussian pulse. The transverse coherence length is also somewhat less than for the 30 keV case due to the larger photo generation spot and the shorter de Broglie wavelength at 100 keV.

These results clearly indicate that our femtosecond reflectron electron gun concept represents a significant improvement in electron density over current state of the art short electron guns operating in the 100 fs regime. While the pulse duration predicted recently by van Oudheusden for the case of radio frequency (RF) compression [44] are shorter than the results reported here, it is once again emphasized that the present concept uses only static electron optics which are free of possible RF jitter and would be easier to construct and handle.

A few words need to be said concerning the longitudinal rms energy spread ΔE_k. From Table 6.2 it is evident that even for a pulse containing only 2000 electrons, ΔE_K is about 30 eV at the sample. This is large compared to the “thermal” energy spread in the 100 meV range that is characteristic of photocathodes or hot filaments. In (static) reflection high energy electron diffraction (RHEED) the very small longitudinal energy spread gives rise to a large longitudinal coherence length up to about 1 μm, making RHEED useful for determining microstructure [33]. Due to their large energy spread, highly charged femtosecond electron bunches, including the ones produced by the reflectron design, have a much smaller longitudinal coherence length that is comparable to or even less than the transverse coherence

length. Fortunately, molecular structure determinations depend mainly on the transverse coherence length [34,30], which makes bright femtosecond electron bunches useful despite their large energy spread.

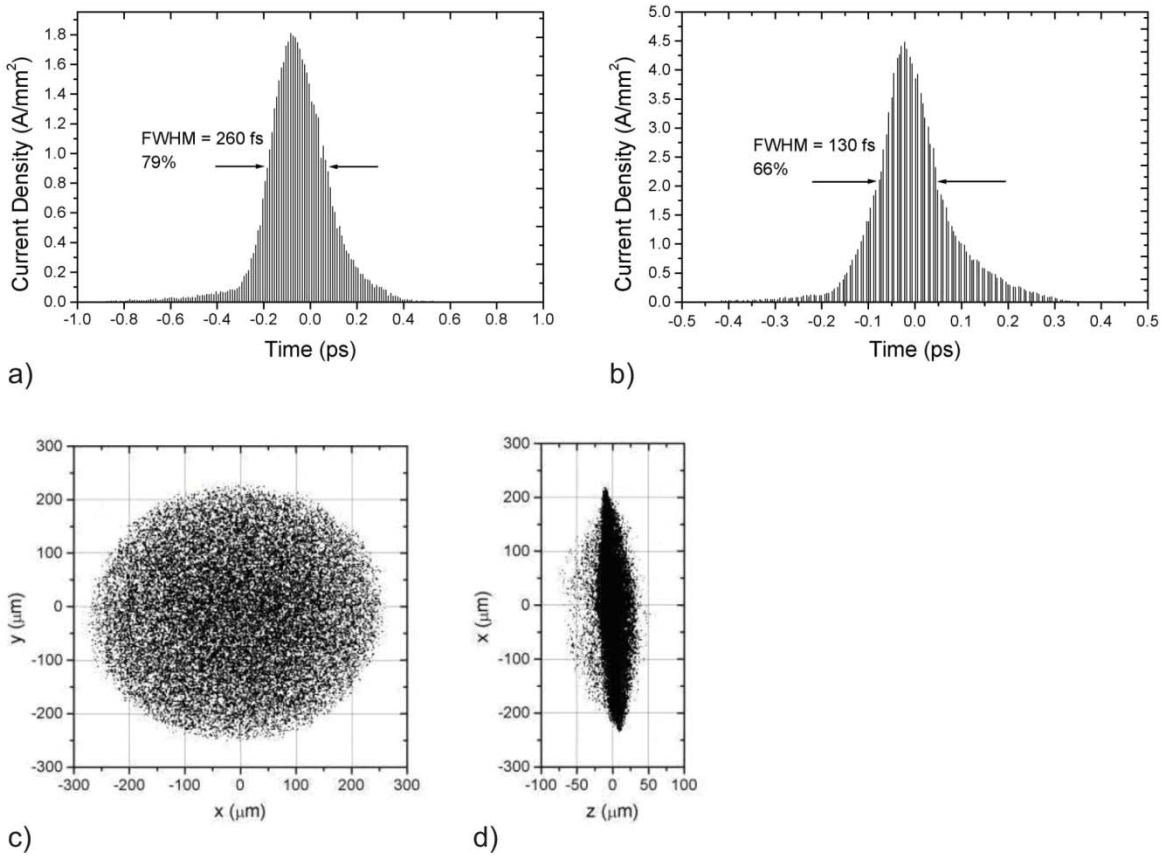

Figure 6.5. Current density versus time profiles of a) the 30 keV pulse containing 50 000 electrons and b) the 100 keV pulse containing 200 000 electrons at the temporal focus. The full width at half maximum (FWHM) pulse duration as well as the percentage of electrons contained therein are also shown. The current density profiles have been calculated relative to an optimal fitting plane that is slightly tilted with respect to the *xy* plane. The front and side profiles of the 30 keV pulse is seen in c) and d) respectively.

Sensitivity of the bunch properties to changes in the gun design parameters is an important issue that needs to be addressed. As already mentioned in previous sections, gun performance depends only insensitively on the bunch charge and acceleration voltage. Increasing the bunch charge by more than an order of magnitude in the 30 kV design does not necessitate any change in the optimal design parameters while changing the acceleration voltage by a factor of 3 leads to relatively modest changes. In the 100 kV design, a 5% deviation of θ_B or θ_R from the optimal design values results in less than 5% change of $\varepsilon_{n,x}$, $\varepsilon_{n,y}$, σ_x, σ_y and ΔE at the temporal focus while the longitudinal position of the focus changes by

less than 5 mm and the pulse front tilt angle varies by less than 1 degree. The temporal duration σ_t and angular spread $\sigma_{\theta,x}$ and $\sigma_{\theta,y}$ are more sensitive and change by less than 25%. Variation of the reflectron length s_R by 5% results in a deviation of less than 5% for $\varepsilon_{n,x}$, $\varepsilon_{n,y}$, and ΔE while σ_x and σ_y change by less than 11%. $\sigma_{\theta,x}$ and $\sigma_{\theta,y}$ vary by less than 15% and the position of the temporal focus, the pulse front tilt angle and σ_t vary by up to 20 mm, 2 degrees and 25% respectively. The author believes that these results demonstrate reasonable robustness of the design.

Only one high voltage power supply is required which can be connected to both the electron gun and the reflectron. For normal incidence of the electron beam into the reflectron, a possible concern would be that the beam could collide with the negative reflectron plate. Since the angle of incidence deviates from the normal by about 3 degrees, this danger is averted and a beam clearance of a few millimetres is guaranteed. Separate power supplies for gun and reflectron could however make adjustments easier. Another concern is the stability of the high voltage supply. Jitter in the supply voltage gives rise to an arrival time jitter of the electron pulse at the sample due to flight time differences at different electron energies. In the current setup, a DC voltage stability of one in 10^6 is sufficient to guarantee an arrival time jitter of less than 10 fs, which is considerably less than the pulse duration. High voltage supplies with suitable stability ratings are commercially available.

6.2.4 Post-Sample Signal Distortions

Perhaps a more serious concern, which affects the transverse spatial resolution of the femtosecond diffractometer, is the possibility of distortions of the diffracted signal resulting from space charge forces due to the un-scattered portion of the pulse a short distance after interaction with the sample. In transmission electron diffraction, only a small fraction of the electrons is scattered, leaving the greater part of the pulse to continue virtually uninterrupted. Thus far this has not been considered since femtosecond pulses containing less than ~10 000 electrons do not appear to cause any such distortions. However, in raising the electron numbers to the 10^5 range by employing compression techniques, this effect must be considered. Typical diffraction angles are in the 10 mrad range, and for a pulse with radius 0.1 mm this means that the diffracted electrons only escape the influence of the main beam a distance on the order of 1 cm after the sample. As can be seen from the pulse radius plots in Figure 6.4, one can expect significant de-focusing of the signal to occur on this length scale. In addition, as the signal separates from the main pulse, the de-focusing effect will become increasingly asymmetric, resulting furthermore in a deflection in the direction of separation. To estimate the post-sample signal distortion, the propagation of the diffracted signal from

sample to detector under influence of the highly charged bunch was simulated using the ASTRA code as follows: a random uniformly distributed subset comprising 3000 electrons was selected from the simulated electron distributions at the sample for both the 50 000 electron, 30 kV and 200 000 electron, 100 kV cases. An angular deflection of 30 mrad and 15 mrad in the *y*-direction respectively was imparted on these sub-bunches to simulate the diffracted signal. The sub-bunches were then tracked considering the influence of space charge due to the main (un-scattered) bunch, neglecting space charge effects due to sub-bunch electrons.

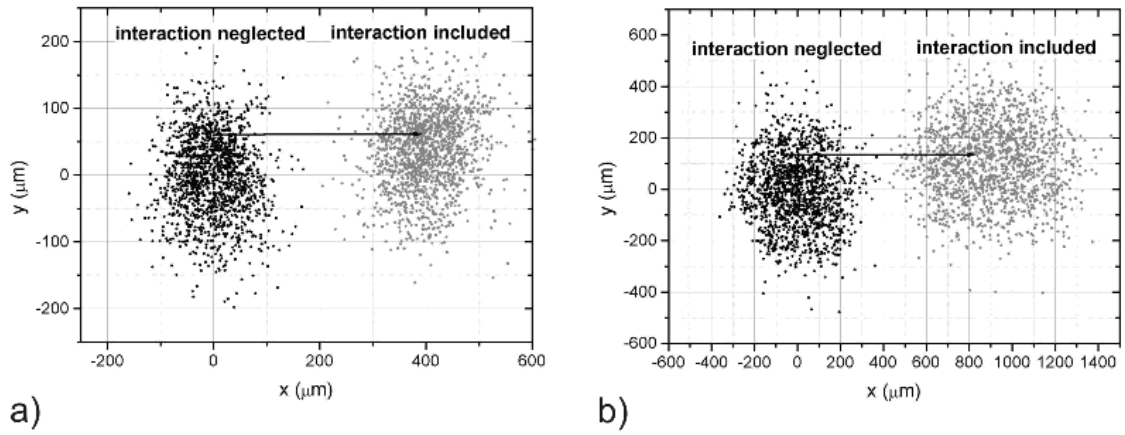

Figure 6.6. Simulated diffraction spot shapes with and without interaction of the diffracted signal with the un-scattered pulse for a) 50 000, 30 kV electrons at a camera length of 20 cm and diffraction angle of 30 mrad, and b) 200 000, 100 kV electrons with a camera length of 40 cm and diffraction angle of 15 mrad. The pulses with interaction included have been shifted to the right for visual purposes since they overlap with the pulses where interaction is neglected. The vertical (*y*) shift is an actual displacement due to signal-pulse interaction.

The results of these simulations can be seen in Figure 6.6. In case of the 30 kV bunch as shown in Figure 6.6 a), the dominant effect is a small deflection of the diffracted signal along the *y*-direction, with little signal broadening due to the additional de-focusing effect. The deflected distance of about 60 μm corresponds to an angle of about 0.3 mrad, which is small but noticeable. In case of the 100 kV pulse (Figure 6.6 b)), the deflection distance of 130 μm at a camera length of 40 cm amounts to about 0.3 mrad angular deflection. In addition, the de-focusing effect seems more pronounced, leading to noticeable spot broadening and consequent loss of spatial resolution. It is evident that pulse-signal interactions need to be taken into account if the best possible spatial resolution is to be achieved. The signal shifts, which are relatively small for the pulses considered here, can probably be corrected quite

easily in the data analysis of diffraction signals. The signal broadening due to the de-focusing effect can be countered by increasing the angular convergence of the bunch at the sample. The added angular spread would of course decrease the coherence length, and therefore it seems that large bunch charges place additional limits on the attainable spatial resolution of ultrafast electron diffractometers. More detailed studies are required to determine exactly what these limits are.

6.3 Pulsed Cavity Compressor

The reflectron compressor discussed in the previous section is a low cost alternative to conventional RF cavity compressor concepts, and would probably be easier to implement, particularly for groups lacking experience and facilities in particle accelerator technology. It does however have some disadvantages. The reflectron as implemented here cannot alter the rms energy spread inherent in the pulse; it merely reverses the chirp in an analogous way to laser pulse compressors based on dispersive elements such as gratings, prisms or chirped mirrors. This means that the freedom one has in choosing pulse parameters such as duration and electron density of the pulse at the sample is more limited than in the case of an RF cavity. In addition, the direction of the beam is reversed, requiring a complete re-design of the electron diffractometer without compression. To avoid these disadvantages but still retain ease of construction and low cost, the novel concept of pulsed cavity compression is introduced here, and the potentially excellent performance of such a design is shown by simulations.

The streak camera concept described in Chapter 5 has an interesting spin-off application: if the device were oriented such that the streak field points parallel to the pulse propagation instead of perpendicular, a longitudinal chirp would be introduced. In fact, the device would operate exactly like a conventional RF compressor cavity, but without all the technical difficulties associated with the latter. This cavity would also be synchronised with the electron pulse with a jitter of 60 fs or less as described in Section 5.3.3, a requirement for compressed femtosecond electron pulse sources in UED. To estimate the momentum spread that can be introduced by such a cavity, the procedure followed is analogous to that adopted for the streak camera in Section 5.2.1. Once again, the electron pulse is represented by two particles which arrive at the cavity at different times, as illustrated in Figure 6.7. Assuming an abruptly terminated time dependent electric field $E(t)$, this time pointing in the $+z$-direction, a pulse of length Δt will be imparted with a longitudinal momentum spread Δp_z given by

$$\Delta p_z = e\left[\int_{t1}^{t1+\Delta t} E(\tau)d\tau - \int_{t1+T}^{t1+\Delta t+T} E(\tau)d\tau\right] \tag{6.11}$$

In analogy to equation 5.3. For $\Delta t << T$, this becomes

$$\Delta p_z = \Delta p_1 - \Delta p_2 = -e\Delta E\Delta t \tag{6.12}$$

where $\Delta E = E(t_1)\text{-}E(t_1+T)$ and Δp_1 and Δp_2 are the momentum difference imparted on electron 1 and electron 2 by the cavity respectively. A pulse that is initially positively chirped can thus become negatively chirped after traversing the cavity, leading to self-compression after a certain longitudinal focal length. Moreover, the imparted chirp will be linear for sufficiently small Δt.

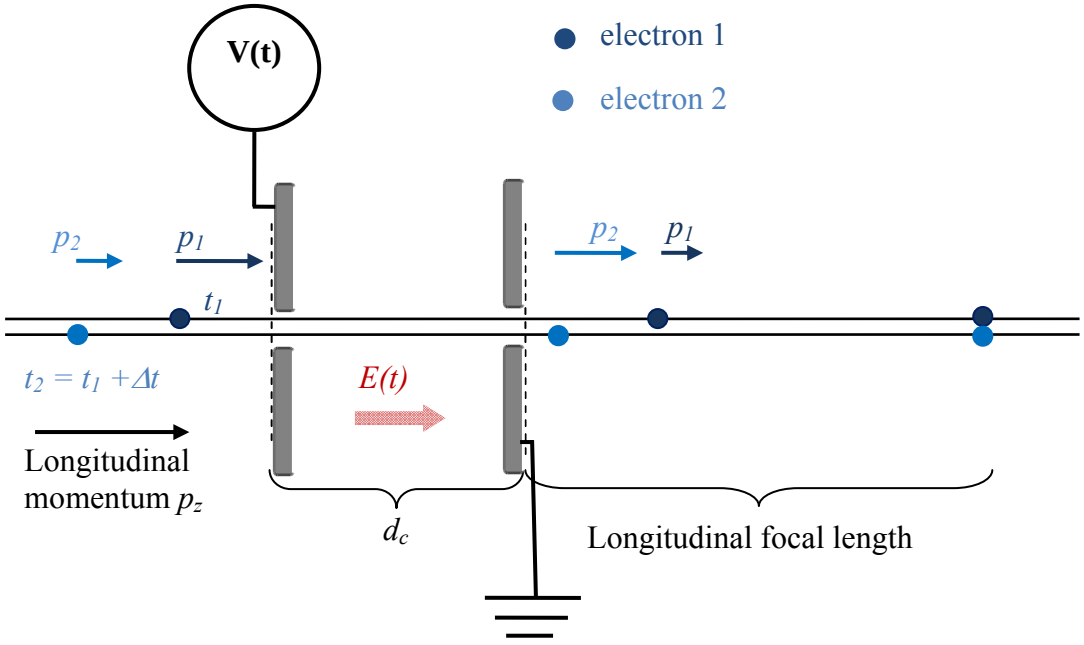

Figure 6.7. Illustration of the principle of pulsed cavity bunch compression. The transient electric field $E(t)$ speeds up trailing slower electrons relative to the fast electrons at the front of the pulse. For a sufficiently large momentum "kick" imparted by the cavity the pulse will self-compress in the post-cavity drift space.

It is useful to write Equation 6.12 in terms of the rms energy spread ΔE_k. Differentiation of the momentum $p_z = \gamma m v_z$ with respect to v_z yields

$$dv_z = \frac{dp_z}{m\gamma\left[\frac{v_z^2}{c^2}\gamma^2 + 1\right]} \tag{6.13}$$

Substitution of Equations 3.4, 6.13 and 6.12 into each other yields the desired relation between the rms energy spread ΔE_k, the electric field differential of the cavity ΔE and the rms pulse duration σ_t:

$$\Delta E_k = \frac{\gamma v_z \Delta E \sigma_t}{[\beta^2\gamma^2 + 1]} \tag{6.14}$$

For successful compression, the energy spread imparted on the pulse must overcome the initial positively chirped energy spread of the electron pulse as well as the Coulomb potential of the pulse in its full state of compression. In addition, there should be a residual un-correlated energy spread required for the desired pulse duration that is consistent with the finite longitudinal emittance, as discussed in Section 3.3. The cavity must therefore deliver an energy spread equal to the sum of these three components. Consider an electron pulse at 30 keV containing 10^5 electrons. If the electron pulse is emitted from a spot on the cathode with an rms radius of 25 μm assuming an electron gun as described in the previous sections, the rms energy spread of the pulse will be about 170 eV at a longitudinal position of 6 cm. The corresponding longitudinal emittance is about 0.8 π eV mm. For a desired pulse duration of 100 fs FWHM at full compression, this $\varepsilon_{n,z}$ value predicts that an un-correlated excess rms energy spread of about 200 eV must be present at the temporal focus. The required rms energy spread in the bunch rest frame to overcome the coulomb potential is given via Equation 3.7 as 0.55 eV for an rms bunch radius of 125 μm at the temporal focus. It is however not only the longitudinal rms velocity Δv_z that contributes to overcoming this potential U, but also the transverse rms velocity Δv_t according to

$$U = \frac{1}{2} m(\Delta v_z^2 + \Delta v_t^2) \tag{6.15}$$

Assuming a transverse rms beam convergence of 4 mrad corresponding to $\Delta v_t = 4\times10^5$ m/s due to the magnetic lens one obtains $\Delta v_z = 1.7\times10^5$ m/s. According to Equation 3.4 this corresponds to an rms energy spread of 120 eV. The total energy spread that needs to be delivered by the cavity is therefore estimated to be 170 eV + 200 eV + 120 eV = 490 eV. To design a suitable cavity, one must decide on a suitable cavity length d. This should be chosen such that the transit time of the pulse through the cavity is significantly greater than the rms pulse duration σ_t at injection to avoid breakdown of the assumptions leading to the linear temporal focussing predicted by Equation 6.12. Assuming 2 ps for σ_t, a transit time of 15 ps corresponding to d = 1.5 mm is suitable. According to equation 8.5, $\Delta E = 2.6\times10^6$ V/m. For a cavity frequency of 10 GHz, a peak charging voltage of 3.1 kV is sufficient to generate this ΔE, assuming a sinusoidal waveform. Figure 6.8 shows a possible design of the proposed cavity in terms of the geometry and simulated electrostatic potential. The frequency of the cavity in Figure 6.8 was estimated to be 10 GHz by approximating the effective inductance of each (symmetric) half as 3 nH and the capacitance as 0.08 pF. The GaAs switch of the streak camera has an electrode spacing of 1 mm, and can withstand voltages in excess of 1.5 kV. It is realistic to assume that a switch with 1.5 mm spacing could withstand in excess of 3 kV given a more optimal electrode geometry that

minimises edge fields. The static electric field corresponding to this geometry was approximated by solving the potential problem of the radial symmetric geometry in Figure 6.8 using the Poisson/ Superfish code [61]. The RF field was generated by alternating the on-axis field profile in time with a frequency of 10 GHz and damping corresponding to a Q factor of 3[20]. Since a damped waveform cannot be directly fed into the ASTRA code [59], this field was decomposed into a series of 10 harmonic waveforms using a discrete Fourier transform. These were fed into ASTRA by defining 10 identical superimposed RF cavities, each corresponding to a Fourier component of the field. While it is a good approximation to consider the RF field to be a standing wave in the region between the high potential plate and the beam entrance side of the ground plate, this is not the case on the exit side of the pulse, where one expects a travelling wave. Since the electric field magnitude is much less on this side, and since any compression effects are partially cancelled due to the relatively long transit time, the travelling field effect was neglected in the simulations.

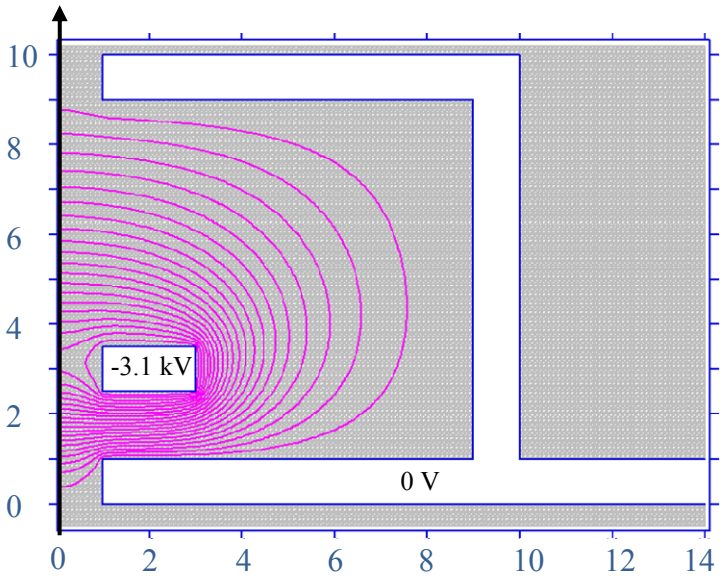

Figure 6.8. Geometry of the proposed pulsed cavity with electrostatic potential contours obtained from a Poisson simulation. The beamline is indicated by the arrow.

The complete setup is shown in Figure 6.9 and consists of the usual photo gun followed by the same magnetic lens used for the reflectron setup simulation in Section 6.2.1. The emission region on the photo cathode was assumed to be radial uniform with an rms radius of 25 mm and a Fermi-Dirac type emission with a photon energy exceeding the cathode work function by 0.4 eV.

[20] This Q value is equal to the value obtained for the streak camera, and probably a good estimate.

With the photo cathode position taken as $z = 0$, the position of the solenoid lens was taken such that the peak axial magnetic field is at $z = 4.2$ cm. The entrance of the pulsed cavity is positioned at 7.0 cm, and the peak electric field was chosen as 3.2 kV. The cavity phase was set to -90°[21] so that there is zero net energy gain of the bunch centre as it passes through the transient field. This choice of phase minimises timing jitter of the pulse due to fluctuations in the supply voltage of the cavity, and also minimises nonlinearities in the temporal focussing.

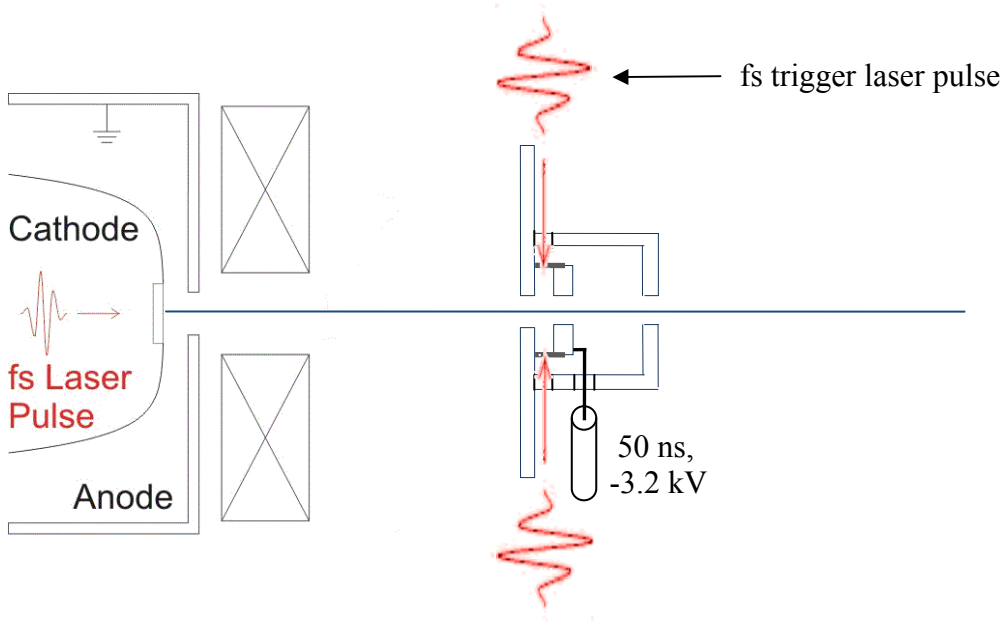

Figure 6.9. Pulsed cavity compressor setup. The pulsed cavity is charged to a high voltage on the centre electrode via a 50 ns HV pulse. The two photo switches connecting the charged electrode to ground are triggered simultaneously by two synchronised fs laser pulses, resulting in a symmetric discharge of the electrode. The injection timing is such that the electron bunch centre experiences no energy change and experiences near-linear temporal focussing.

The FWHM bunch duration and rms radius are plotted versus propagation distance in Figure 6.10. The pulse broadens rapidly in both transverse and longitudinal directions, reaching an rms radius of about 300 μm and a FWHM duration in excess of 4 ps. The pulse is focussed in the radial direction by the solenoid lens and in the longitudinal direction by the pulsed cavity. The angular convergence at the temporal focus is chosen such that the extension of the trajectories are focussed at the detector with a camera length of 400 mm. From the inset in Figure 6.10 it is seen that the pulse duration reaches a minimum of about 90 fs, but changes rapidly with

[21] The cavity phase is defined such that 0° corresponds to the phase of maximum energy gain of the bunch centre.

propagation distance so that the pulse duration remains below 100 fs for a distance of only about 1 mm.

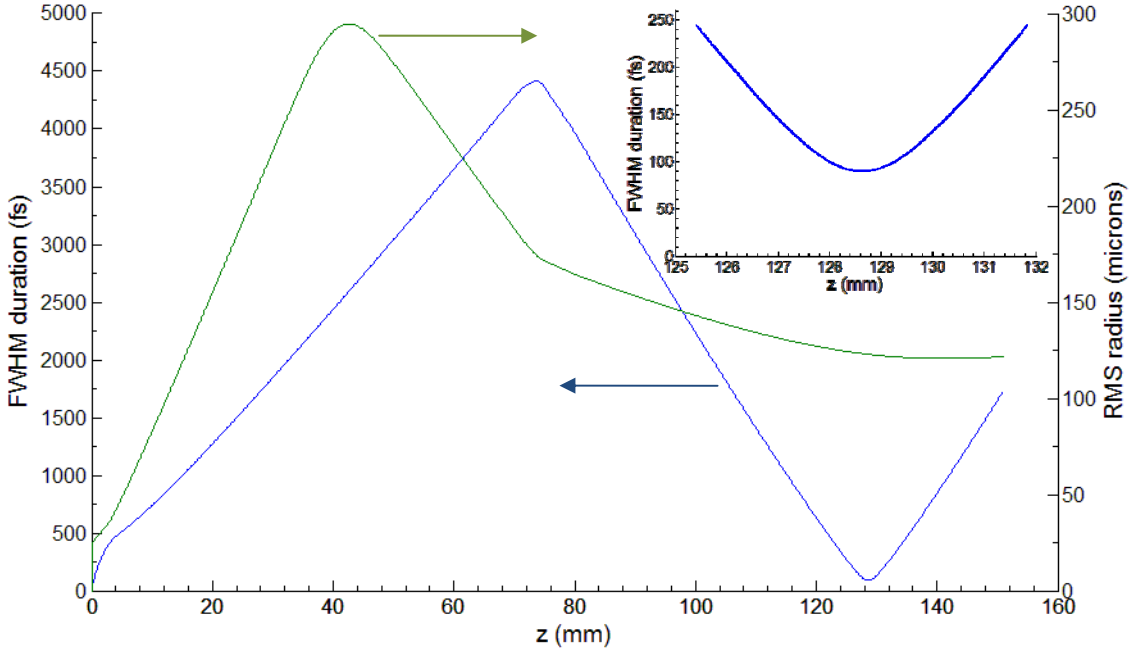

Figure 6.10. Simulated bunch radius and temporal duration versus propagation distance of pulses containing 10^5 electrons compressed by the pulsed cavity. The inset affords a more detailed view of the behaviour of the pulse duration near the temporal focus.

The remaining parameters of the bunch at temporal focus are as follows: rms radius σ_x = 125 μm, transverse normalised emittance $\varepsilon_{n,x}$ = 20 π nm, transverse coherence length $L_{c,x}$ = 1.9 nm, rms energy spread ΔE_k = 190 eV, longitudinal normalised emittance $\varepsilon_{n,z}$ = 0.73 π eV mm, longitudinal coherence length $L_{c,z}$ = 0.4 nm. As can be seen from Figure 6.11, $\varepsilon_{n,x}$ does not experience a significant net increase from the initial emission value. This is however not true for $\varepsilon_{n,z}$. This rapid increase of $\varepsilon_{n,z}$ has already been described in Chapter 3 where it was found to increase roughly in proportion to the electron number in the pulses. It appears that highly charged pulses inevitably suffer from a large energy bandwidth, and it remains to be investigated in detail what the effect of this will be in actual UED experiments. The pulsed cavity does however not appear to contribute significantly to the longitudinal emittance, indicating that the temporal focussing is close to linear.

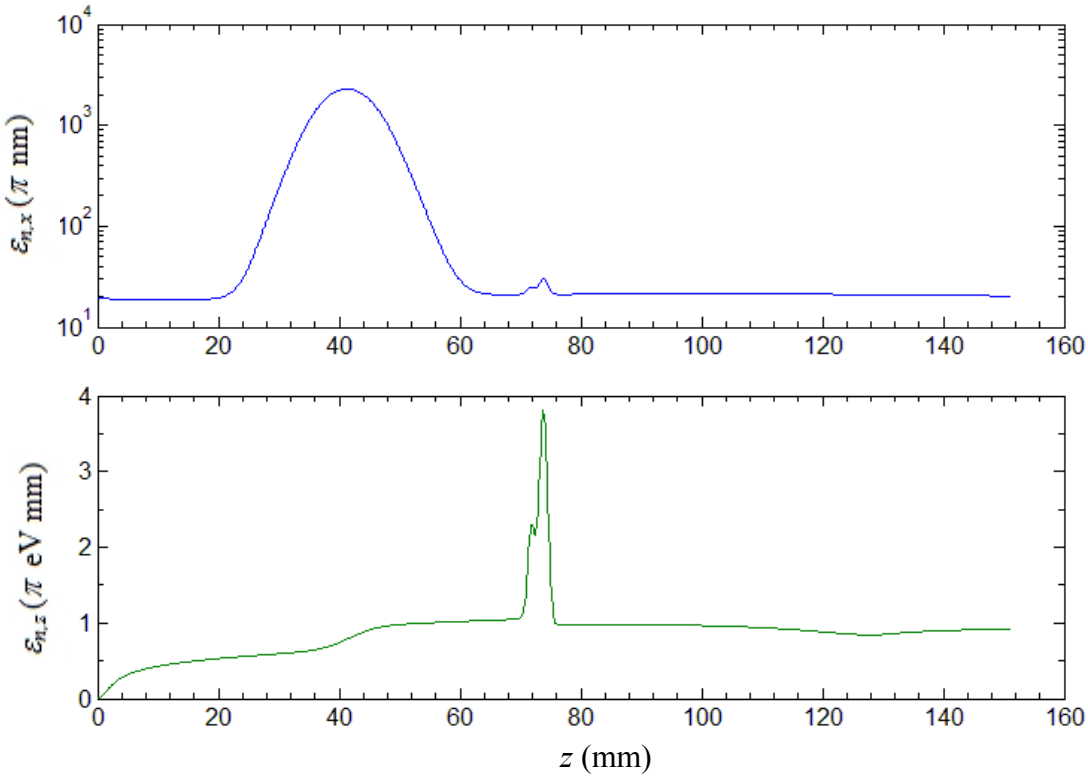

Figure 6.11. Transverse (top) and longitudinal (bottom) normalised emittance versus propagation distance. There is no net transverse normalised emittance growth from the electron source to the sample, but the longitudinal normalised emittance increases significantly. The pulsed cavity itself does however not lead to further longitudinal emittance growth.

7. SUMMARY, CONCLUSIONS AND OUTLOOK

In the current dissertation, the following content has been covered:

1) A framework for understanding the dynamics of electron bunches in UED taking account of the dependence of both spatial and temporal resolution on bunch parameters has been covered in Chapter 3, based on elementary beam physics concepts that have been introduced in Chapter 2.
2) A compact UED gun has been designed and verified with the help of detailed electron bunch simulations that include all relevant effects such as the initial photoelectron energy spread of electrons, space charge forces and detailed beamline element geometries. The design methodology and results, reported on in Chapter 3, have shown that it is in principle possible to construct an UED setup capable of producing bright high energy electron beams (30- 60 keV) containing 5000 electrons per pulse with a rms radius below 0.1 mm, a transverse coherence length above 2 nm and sub-300 fs temporal duration. This setup has been designed with the aim of probing structural dynamics of specimens with a reasonable number of shots, thereby also allowing the investigation of samples with a large unit cell size that cannot be pumped and probed repeatedly.
3) The UED setup determined by the detailed design has been constructed as described in Chapter 4. Although the setup is not operating at the exact design parameters yet, particularly in terms of the initial rms electron source size at the photocathode, the setup has been characterised with respect to beam size, angular spread and temporal duration. Good agreement was found for simulated and measured transverse beam parameters, allowing one to proceed with confidence in the final optimisation stages, which are expected to consist mainly in achieving a smaller initial electron spot size.
4) A compact streak camera that is particularly well suited for temporal characterisation of bright UED pulses has been developed as part of the current project, and is described in detail in Chapter 5. The streak camera is shown to have a temporal resolution of better than 200 fs, and therefore represents a substantial improvement over any other streak camera so far implemented for sub-relativistic electron beams. The temporal resolution rivals that obtained by the current state of the art ponderomotive electron pulse-laser pulse cross correlation techniques. At the same time, the measurement of electron pulses produced by the current UED gun has convincingly demonstrated that sub-300 fs temporal resolution is easily achievable.
5) In the quest for ever brighter UED sources, van Oudheusden et al. have proposed a UED pulse compression source for sub-relativistic UED beams based on conventional RF cavity

technology. Experimental confirmation of the concept is still pending almost three years after the original proposal. In Chapter 6, two alternative electron bunch compression concepts developed by the author are described: achromatic reflectron compression and pulsed cavity compression. The feasibility of both concepts is made plausible by convincing arguments and detailed particle simulation results. A strong case is made for the statement that these concepts will be easier to implement than other more conventional designs.

While the UED setup described in this dissertation is essentially operational, some improvements are still necessary to make it better suited for experiments. As was already mentioned, the electron beam size at the sample is currently too large, resulting in non-linear focussing by the magnetic lens as discussed in Section 4.5.3. The best way of reducing the beam size at the sample is to reduce the size of the source at the photocathode. This can be done by more tight focussing of the UV beam (see Section 4.2) onto the photocathode by telescopic enlargement of the UV beam prior to the focussing lens. Another issue is currently the achievable vacuum, which is at best in the 10^{-6} mbar range. This needs to be improved to at least the 10^{-7} mbar range, particularly if reflection electron diffraction studies are to be attempted. The author is confident that this will be attained once all leaks in the vacuum chamber have been identified and fixed. Lastly, the current electron detection method needs some improvement. The camera currently used to record the image displayed by the MCP (see Section 4.4) is not of a scientific grade and suffers from excessive pixel noise. While this has so far not been a problem, particularly in connection with the streak camera measurements, it will surely become an issue if one wishes to record diffraction patterns in the presence of inevitably low electron flux.

The ultrafast electron diffractometer designed, constructed and characterised as part of this study is, subject to some minor improvements, ready to be used in experiments that study ultrafast structural evolution of matter. It is therefore important to discuss possible research projects that can be undertaken in future. Initially, it is wise to consider relatively simple systems, and one interesting possibility is the study of ultrafast laser induced phonon dynamics and/ or melting of thin free standing titanium foils. While much work has been done on ultrafast melting of metals, particularly gold and aluminium which have a cubic crystal structure, Ti may provide interesting new results due to the fact that it has a hexagonal crystal structure.

Another potentially fruitful project is the investigation of ultrafast dynamics at metal-semiconductor interfaces. In semiconductor processing technology, a major issue has been the formation of eutectic alloys after the deposition of metals on semiconductors (e.g. gold on

silicon). The eutectic formation is known to occur above a very precisely defined temperature, suggesting that a phase transformation is taking place with potentially interesting dynamics, perhaps on ultrafast timescales. UED in reflection geometry would be an ideal tool to investigate such processes, and systems of silicon and germanium with various metals will be considered for these experiments.

UED sources with a good coherence length in the nm range as the one constructed during this study are in principle capable of probing materials with larger, more complicated unit cells such as organic crystals. It is known that certain organic crystals undergo a rapid photo-induced metal-insulator phase transition. As shown by Chollet et al. [100] by ultrafast reflectivity measurements, this transition can occur on sub-picosecond timescales. Interestingly, the phase transition is accompanied by a structural re-arrangement in the crystal; while the dynamics of the electronic transition is known from the ultrafast reflectivity measurements, nothing is known about the concomitant structural evolution dynamics. UED has the potential to provide answers to this question.

The investigation of structural dynamics on femtosecond timescales is at the dawn of a new era that has been ushered in by the realisation of novel high brightness table top sources (most notably compact UED sources) alongside much larger facilities such as the X-ray free electron lasers. The difference in their size and availability is tremendous, but nevertheless these facilities will contribute in complementary ways to our understanding of the dynamics associated with the very building blocks of matter.

REFERENCES

1. Watson, J. D., Crick, F. H. C.: A structure for Deoxyribonucleic acid. Nature 171, 737 (1953)
2. Watson, J. D.: The double helix: A personal account of the discovery of the structure of DNA. Penguin Books, London (1999)
3. Bryson, B.: A short history of nearly everything. Black Swan (2004)
4. Roentgen, W. C.: Ueber eine neue Art von Strahlung., Aus den Sitzungsberichten der Wuerzburger Physik.- Medic. Gesellschaft, Wuerzburg (1895)
5. Rousse, A., Rischel, C., Gauthier, J. C.: Colloquium: Femtosecond x-ray crystallography. Rev. Mod. Phys. 73, 6861 (2001)
6. Pfeifer, T., Spielmann, C., Gerber, G.: Femtosecond x-ray science. Rep. Prog. Phys. 69, 443 (2006)
7. Tomov, I. V., Oulianov, D. A., Chen, P., Rentzepis, P. M.: Ultrafast time-resolved transient structures of solids and liquids studied by means of. J. Phys. Chem. 103, 7081 (1999)
8. Brown, F. L. H., Wilson, K. R., Cao, J.: Ultrafast extended x-ray absorption fine structure (EXAFS) — theoretical considerations. J. Chem. Phys. 111, 6238 (1999)
9. Chergui, M., Zewail, A. H.: Electron and X-ray methods of ultrafast structural dynamics: advances and applications. ChemPhysChem 10, 28 (2009)
10. Dwyer, J. R., Hebeisen, C. T., Ernstorfer, R., Harb, M., Deyirmenjian, V. B., Jordan, R. E., Miller, R. J. D.: Femtosecond electron diffraction: 'making the molecular movie'. Phil. Trans. Roy. Soc. A 364, 741 (2006)
11. Miller, R. J. D., Ernstorfer, R., Harb, M., Gao, M., Hebeisen, C. T., Jean-Ruel, H., Lu, C., Moriena, G., Sciaini, G.: 'Making the molecular movie': First frames. Acta Cryst. A66, 137 (2010)
12. Siwick, B. J., Miller, R. J. D.: Femtosecond electron diffraction studies of strongly driven structural phase transitions. Chem. Phys. 299, 285 (2004)
13. King, W. E., Campbell, G. H., Frank, A., Reed, B., Schmerge, J. F., Siwick, B., Stuart, B. C., Weber, P. M.: Ultrafast electron microscopy in materials science, biology, and chemistry. J. Appl. Phys. 97, 11101 (2005)
14. Zewail, A. H.: 4D ultrafast electron diffraction, crystallography, and microscopy. Annual Review of Physical Chemistry 57, 65 (2006)
15. Ihee, H., Cao, J., Zewail, A. H.: Ultrafast electron diffraction: structures in dissociation dynamics of Fe(CO)(5). Chem. Phys. Lett. 281, 10 (1997)
16. Ihee, H., Lobastov, V. A., Gomez, U. M., Goodson, B. M., Srinivasan, R., Ruan, C. Y., Zewail, A. H.: Direct imaging of transient molecular structures with ultrafast diffraction. Science 291, 458 (2001)
17. Siwick, B. J., Miller, R. J. D.: An atomic-level view of melting using femtosecond electron diffraction. Science 302, 1382 (2003)
18. Sciaini, G., Harb, M., Kruglik, S. G., Payer, T., Hebeisen, C. T., Meyer zu Heringdorf, F. J., Yamaguchi, M., Horn-von Hoegen, M. l., Ernstorfer, R., Miller, R. J. D.: Electronic acceleration of atomic motions and disordering in bismuth. Nature Letters 458, 56 (2009)
19. Ernstorfer, R., Harb, M., Hebeisen, C. T., Sciaini, G., Dartigalongue, T., Miller, R. J. D.: The Formation of warm densematter: experimental evidence for electronic bond hardening in gold. Science 323, 1033 (2009)
20. Harb, M., Ernstorfer, R., Dartigalongue, T., Hebeisen, C. T., Jordan, R., Miller, R. J. D.: Carrier relaxation and lattice heating dynamics in silicon revealed by femtosecond electron

diffraction. J. Phys. Chem. B 110, 25308 (2006)

21. Harb, M., Peng, W., Sciaini, G., Hebeisen, C. T., Ernstorfer, R., Eriksson, M. A., Lagally, M. G., Kruglik, S. G., Miller, R. J. D.: Excitation of longitudinal and transverse coherent acoustic phonons in nanometer free-standing films of (001) Si. Phys. Rev. B 79, 94301 (2009)
22. Ruan, C., Lobastov, V. A., Vigliotti, F., Chen, S., Zewail, A. H.: Ultrafast electron crystallography of interfacial water. Science 304, 80 (2004)
23. Yang, D.-S., Zewail, A. H.: Ordered water structure at hydrophobic graphite interfaces observed by 4D, ultrafast electron crystallography. PNAS 106, 4122 (2009)
24. Janzen, A., Krenzer, B., Zhou, P., von der Linde, D., Horn von Hoegen, M.: Ultrafast electron diffraction at surfaces after laser excitation. Surface Science 600, 4094 (2006)
25. Hanisch, A., Krenzer, B., Pelka, T., Mollenbeck, S., Horn-von Hoegen, M.: Thermal response of epitaxial thin Bi films on Si(001) upon femtosecond laser excitation studied by ultrafast electron diffraction. Phys. Rev. B 77, 125410 (2008)
26. Baum, P., Yang, D., Zewail, A. H.: 4D visualization of transitional structures in phase transformations by electron diffraction. PNAS 103, 16105 (2007)
27. Carbone, F., Baum, P., Rudolf, P., Zewail, A. H.: Structural preablation dynamics of graphite observed by ultrafast electron crystallography. Appl. Phys. Lett. 100, 35501 (2008)
28. Carbone, F., Kwon, O.-H., Zewail, A. H.: Dynamics of chemical bonding mapped by energy-resolved 4D electron microscopy. Science 325, 181 (2009)
29. Gedik, N., Yang, D., Logvenov, G., Bozovic, I., Zewail, A. H.: Nonequilibrium phase transitions in cuprates observed by ultrafast electron crystallography. Science 316, 425 (2007)
30. Michalik, A. M., Sipe, J. E.: Evolution of non-Gaussian electron bunches in ultrafast electron diffraction experiments: Comparison to analytic model. J. Appl. Phys. 105, 84913 (2009)
31. van der Geer, S. B., de Loos, M. J., van Oudheusden, T., op ’t Root, W. P. E. M.: Longitudinal phase-space manipulation of ellipsoidal electron bunches in realistic fields. Physical Review Special Topics - Accelerators and Beams 9, 44203 (2006)
32. Kassier, G. H., Haupt, K., Erasmus, N., Rohwer, E. G., and Schwoerer, H.: Achromatic reflectron compressor design for bright pulses in femtosecond electron diffraction. J. Appl. Phys. 105, 113111 (2009)
33. Ichimiya, A., Cohen, P. I.: Reflection high energy electron diffraction. Cambridge University Press, Cambridge (2004)
34. Michalik, A. M., Sherman, E. Y., Sipe, J. E.: Theory of ultrafast electron diffraction: The role of the electron bunch properties. J. Appl. Phys. 104, 54905 (2008)
35. Flottmann, K.: Note on the thermal emittance of electrons emitted by Cesium Telluride photo cathodes. TESLA-FEL report, DESY, Hamburg (1997)
36. Clendenin, J. E., Kotseroglou, T., Mulhollan, G. A., Palmer, D. T., Schmerge, J. F.: Reduction of thermal emittance of rf guns. SLAC-PUB 99, 8284 (1999)
37. Dowell, D. H., Schmerge, J. F.: Quantum efficiency and thermal emittance of metal photocathodes. Phys. Rev. ST Accel. Beams 12, 74201 (2009)
38. Janzen, A., Krenzer, B., Heinz, O., Zhou, P., Thien, D., Hanisch, A., Heringdorf, F., von derLinde, D., Horn von Hoegen, M.: A pulsed electron gun for ultrafast electron diffraction at surfaces. Rev. Sci. Instrum. 78, 13906 (2007)
39. Michalik, A. M., Sipe, J. E.: Analytic model of electron pulse propagation in ultrafast electron diffraction experiments. J. Appl. Phys. 99, 54908 (2006)

40. Siwick, B. J., Dwyer, J. R., Jordan, R. E., Miller, R. J. D.: Ultrafast electron optics: Propagation dynamics of femtosecond electron packets. J. Appl. Phys. 92, 1643 (2002)
41. Luiten, O. J., van der Geer, S. B., de Loos, M. J., Kiewiet, F. B., van der Wiel, M. J.: How to realize uniform three-dimensional ellipsoidal electron bunches. Phys. Rev. Lett. 93, 94802 (2004)
42. Batygin, Y.: Test problems for validation of space charge codes. Proceedings of the 1999 Particle Accelerator Conference (1999)
43. Luiten, O. J., van der Geer, B., de Loos, M., Kiewiet, F. B., van der Wiel, M. J.: Ideal waterbag electron bunches from an RF photogun. In : Proceedings of EPAC, p.725 (2004)
44. van Oudheusden, T., de Jong, E. F., van der Geer, S., Op 't Root, W. P. E. M., Luiten, O. J.: Electron source concept for single-shot sub-100 fs electron diffraction in the 100 keV range. J. Appl. Phys. 103, 93501 (2007)
45. Cao, J., Hao, Z., Park, H., Tao, C., Kau, D., Blaszczyk, L.: Femtosecond electron diffraction for direct measurement of ultrafast atomic motions. Appl. Phys. Lett. 83, 1044 (2003)
46. Hastings, J. B., Rudakov, F. M., Dowell, D. H., Schmerge, J. F., Cardoza, J. D., Castro, J. M., Gierman, S. M., Loos, H., Weber, P. M.: Ultrafast time-resolved electron diffraction with megavolt electron beams. Applied Physics Letters 89, 184109 (2006)
47. Musumeci, P., Faillace, L., Fukasawa, A., Moody, J. T., O'Shea, B., Rosenzweig, J. B., Scoby, C. M.: Novel radio-frequency gun structures for ultrafast relativistic electron diffraction. Microsc. Microanal. 15, 290 (2009)
48. Williamson, S., Mourou, G., Li, J. C. M.: Time-resolved laser-induced phase-transformation in aluminum. Phys. Rev. Lett. 52, 2364 (1984)
49. Elsayed-Ali, H. E., Herman, J. W.: Picosecond time-resolved surface-lattice temperature probe. Appl. Phys. Lett. 57, 1508 (1990)
50. Qian, B. L., Elsayed-Ali, H. E.: Electron pulse broadening due to space charge effects in a photoelectron gun for electron diffraction and streak camera systems. J. Appl. Phys. 91, 462 (2002)
51. Hebeisen, C. T.: Generation, characterization and applications of femtosecond electron pulses. PhD Thesis, University of Toronto, Toronto (2009)
52. Gahlmann, A., Park, S. T., Zewail, A. H.: Ultrashort electron pulses for diffraction, crystallography and microscopy: theoretical and experimental resolutions. Phys. Chem. Chem. Phys. 10, 2894 (2008)
53. Wang, X., Nie, S., Park, H., Li, J., Clinite, R., Li, R., Wang, X., Cao, J.: Measurement of femtosecond electron pulse length and the temporal broadening due to space charge. Rev. Sci. Instrum. 80, 13902 (2009)
54. Hebeisen, C. T., Ernstorfer, R., Harb, M., Dartigalongue, T., Jordan, R. E., Miller, R. J. D.: Femtosecond electron pulse characterization using laser ponderomotive scattering. Opt. Lett. 31, 3517 (2006)
55. Hebeisen, C. T., Sciaini, G., Harb, M., Ernstorfer, R., Dartigalongue, T., Kruglik, S. G., Miller, R. J. D.: Grating enhanced ponderomotive scattering for visualization and full characterization of femtosecond electron pulses. Opt. Express 16, 3335 (2008)
56. van der Geer, S. B., de Loos, M. J., Vredenbregt, E. J. D., and Luiten, O. J.: Ultracold electron source for single-shot, ultrafast electron diffraction. Microsc. Microanal. 15, 282 (2009)
57. www.desy.de/xfel-beam/csrtrack/.
58. van der Geer, B., de Loos, M.: The General Particle Tracer code design, implementation and application. PhD thesis, Technische Universiteit Eindhoven (2001)

59. www.desy.de/~mpyflo/.
60. Floettmann, K., Lidia, S. M., Piot, P.: Recent improvements to the Astra particle tracking code., DESY, Hamburg (2006)
61. Available at: laacgl.lanl.gov/laacg/services/download_sf.phtml.
62. Rogowski, W.: Die elektrische Festigkeit am Rande des Plaltenkondensators. Ein Beitrag zur Theorie der Funkensirecken und Durchfuhrungen. Archiv fur Elektrotechnik 7, 1 (1923)
63. Humphries, S. R.: Principles of Charged Particle Acceleration. John Wiley and Sons, Albuquerque (1999) 227
64. Dwyer, J. R. ., Hebeisen, C. T., Harb, M., Ernstorfer, R., Dartigalongue, T., Miller, R. J. D.: Experimental basics for femtosecond electron diffraction studies. J. Mod. Opt. 54, 923 (2007)
65. Rangarajan, L. M., Bhide, G. K.: Photoemission energy-distribution studies of gold thin-films under uv excitation by a photoelectron spectroscopic method. Vacuum 30, 515 (1980)
66. Zou, Y., Li, H., Reiser, M., O'Shea, P. G.: Theoretical study of transverse emittance growth in a gridded electron gun. Nuclear Instruments and Methods in Physics Research A 519, 432 (2004)
67. Allen, C., Pattengale, N.: Theory and technique of beam envelope simulation. Los Alamos National Laboratories, Los Alamos (00)
68. Humphries, S. R.: Principles of Charged Particle Acceleration. John Wiley and Sons, Albuquerque (1999)
69. Wiza, J. L.: Microchannel plate detectors. Nuclear Instruments and Methods 162, 587 (1979)
70. Lide, D. R., editor: Handbook of Chemistry and Physics. CRC Press (2008)
71. Beeston, B. E.: Electron diffraction and optical diffraction techniques. Elsevier Science Ltd (1994)
72. Wilke, I., MacLeod, A., Gillespie, W. A., Berden, G., Knippels, G. M. H., van der Meer, A. F. G.: Single-shot electron-beam bunch length measurement. Phys. Rev. Lett. 88, 124801 (2002)
73. Bolotov, V. N., Kononenko, S. I., Muratov, V. I., Fedorchenko, V. D.: Transition radiation of nonrelativistic electron bunches passing through diaphragms. Technical Physics 49, 466 (2004)
74. Op ’t Root, W. P. E. M., Smorenburg, P. W., van Oudheusden, T., van der Wiel, M. J., Luiten, O. J.: Theory of coherent transition radiation generated by ellipsoidal electron bunches. PhysicalReview Special Topics - Accelerators and Beams 10, 12802 (2007)
75. Thongbai, C., Kusoljariyakul, K., Rimjaem, S., Rhodes, M. W., Saisut, J.: Femtosecond electron bunches, source and characterization. Nuclear Instruments and Methods in Physics Research A 587, 130 (2008)
76. Baum, P., Zewail, A. H.: Breaking resolution limits in ultrafast electron diffraction and microscopy. PNAS 103, 16105 (2006)
77. Siwick, B. J., Green, A. A., Hebeisen, C. T., Miller, R. J. D.: Characterization of ultrashort electron pulses by electron-laser pulse cross correlation. Opt. Lett. 30, 1057 (2005)
78. Courtney-Pratt, J. S.: A new method for the photographic study of fast transient phenomena. Research 2, 287
79. Schelev, M. Y., Richards, M. C., Alcook, A. J.: Image-converter streak camera with picosecond resolution. Appl. Phys. lett. 18, 354 (1971)
80. Aldana, R., Pease, F.: Miniature traveling wave deflection for electron beam analog to digital conversion. Microelectronic Engineering 84, 806 (2007)

81. Jaanimagi, J. A.: Breaking the 100-fs barrier with a streak camera. In : Proc. SPIE, Rochester (2003)
82. Maksimchuk, A., Kim, M., Workman, J., Korn, G., Squier, J., Du, D., Umstadter, D., Mourou, G.: Signal averaging x-ray streak camera with picosecond jitter. Rev. Sci. Insrum. 67, 697 (1996)
83. Niu, H., Sibbett, W.: Theoretical-analysis of space-charge effects in photochron streak cameras. Rev. Sci. Instrum. 52, 1830 (1981)
84. Scheidt, K., Naylor, G.: 500 fs streak camera for uv-hard x rays in 1khz accumulating mode with optical jitter- free synchronisation. In : Proceedings DIPAC, vol. CT03, p.54 (1999)
85. Gallant, P., Forget, P., Dorchies, F., Jiang, Z., Kieffer, J. C., Jaanimagi, P. A., Rebuffie, J. C., Goulmy, C., Pelletier, J. F., Sutton, M.: Characterization of a subpicosecond x-ray streak camera for ultrashort laser-produced plasmas experiments. Rev. Sci. Instrum. 71, 3627 (2000)
86. Belzile, C., Kieffer, J. C., Cote, C. Y., Oksenhendler, T., Kaplan, D.: Jitter-free subpicosecond streak cameras. Rev. Sci. Instrum. 73, 6748 (2002)
87. Liu, J., Wang, J., Shan, B., Wang, C., Chang, Z.: An accumulative x-ray streak camera with sub-600-fs temporal resolution and 50-fs timing jitter. Appl. Phys. Lett. 82, 3553 (2003)
88. Bonte, C., Harmand, M., Dorchies, F., Magnan, S., Pitre, V., Kieffer, J. C., Audebert, P., Geindre, J. P.: High dynamic range streak camera for subpicosecond time-resolved x-ray spectroscopy. Rev. Sci. Instrum. 78, 43503 (2007)
89. Park, H.: The development of femtosecond electron diffraction for direct measurements of ultrafast atomic motions. PhD Thesis, The Florida State University College Of Arts And Sciences (2006)
90. Arsenin, V. Y., Tikhonov, A. N.: Solutions of Ill-Posed Problems. John Wiley & Sons (1977)
91. Landi, G., Zama, F.: The active-set method for nonnegative regularization of linear ill-posed problems. Applied Mathematics and Computation 175, 715 (2006)
92. Musumeci, P., Moody, J. T., England, R. J., Rosenzweig, J. B., Tran, T.: Experimental generation and characterization of uniformly filled ellipsoidal electron-beam distributions. Phys. Rev. Lett. 100, 244801 (2008)
93. Musumeci, P.,. Moody, J., Scoby, C., Gutierrez, M., Tran, T.: rf streak camera based ultrafast relativistic electron diffraction. Rev. Sci. Instrum. 80, 13302 (2009)
94. Baum, P., Zewail, A. H.: Femtosecond diffraction with chirped electron pulses. Chem. Phys. Lett. 462, 14 (2008)
95. Kiewiet, F. B., Kemper, A. H., Luiten, O. J., Brussaard, G. J. H., van der Wiel, M. J.: Femtosecond synchronization of a 3 GHz RF oscillator to a mode-locked Ti:sapphire laser. Nuclear Instruments and Methods in Physics Research A 485, 619 (2002)
96. Flory, C. A., Taber, R. C., Yefchak, G. E.: Analytic expression for the ideal one-dimensional mirror potential yielding perfect energy focusing in TOF mass spectrometry. International Journal of Mass Spectrometry and Ion Processes 152, 177 (1996)
97. Weber, P. M., Carpenter, S. D., Lucza, T.: A reflectron design for femtosecond electron guns. In : Proc. Spie, vol. 2521, p.23 (2005)
98. Kang, H.-S., Kim, G.: Femtosecond electron beam bunch compression by using an alpha magnet and a chicane magnet at the PAL test linac. Journal of the Korean Physical Society 44, 1223 (2004)
99. CSRTRACK version 1.2 user manual.
100. Chollet, M., Guerin, L., Uchida, N., Fukaya, S., Shimoda, H., Ishikawa, T., Matsuda, K. .,

Ota, A., Yamochi, H., Saito, G., Tazaki, R., Adachi, S., Koshihara, S.: Gigantic Photoresponse in ¼-Filled-Band Organic Salt (EDO-TTF)2PF6. Science 307, 86 (2005)